Investigating Electron Transfer Kinetics in Redox Flow Batteries

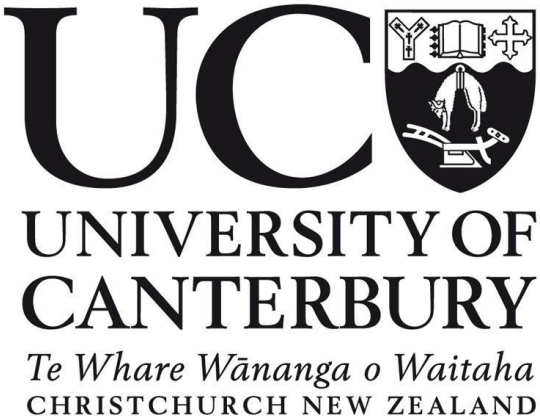

Leatham Landon-Lane

Department of Chemical and Process Engineering

A thesis submitted in partial fulfilment of the requirements
for the degree of Doctor of Philosophy

University of Canterbury, Christchurch, New Zealand

August 2020

Acknowledgements

This work was undertaken in the Chemical and Process Engineering Department (CAPE) of the University of Canterbury between March 2017 and August 2020. Funding for this work was gratefully received from the University of Canterbury Doctoral Scholarship and the MacDiarmid Institute.

I am extremely thankful for the support and guidance of my supervisory team. My primary supervisor Associate Professor Dr Aaron Marshall. At every step he was approachable and innovative, enabling me to make progress and learn throughout my PhD experience. My co-supervisor, Professor Alison Downard, has a great understanding of electrochemistry and as a result led me to improve the clarity and quality of my work on numerous occasions. Without their support this thesis would not be what it is and I would certainly know a lot less about electrochemistry.

The entire CAPE departmental staff have been a pleasure to work with, providing clear expectations and rigorous safety measures, with keen oversight from Rayleen Fredericks, Garrick Thorn and Michael Sandridge. Whenever I needed a new part or piece of equipment, the workshop technicians, Stephen Beuzenberg, Graham Furniss, Graham Mitchell and Leigh Richardson were efficient and easy to work with. I would like to give special thanks to Glenn Wilson for organising the repair of my potentiostat during a global pandemic. Ranee Hearst, Joanne Pollard and Rachel Rogers all helped me to solve various self-inflicted administration issues. Without the help of Ben Reynolds and Daniel Clarke it would not have been possible for me to write the code in Matlab to carry out the numerical simulations. I would also like to thank Wasim Khan for carrying out the BET measurements.

Outside of CAPE, Anna Farquhar Paula Brooksby from the chemistry department were a great help for carrying out my early experiments. During my research I was lucky enough to use Raman spectra equipment at Massey University in Palmerston North, with help from Mark Waterland. Raman measurements were also taken at the University of Auckland with help from Rakesh Arul and the University of Otago by Chima Robert and Keith Gordon.

In a non-academic sense, the supportive and entertaining environment provided by my fellow CAPE postgraduates was second to none. To my family and friends, the emotional support has been invaluable, as has been the sporadic access to the bank of Mum and Dad. And lastly but most definitely not least, I am grateful for the support from my partner Evie Templeton, although we would not necessarily advise other couples to study PhD's at the same time.

Abstract

Vanadium Redox Flow Batteries can enable an increase in the fraction of renewable energy sources, such as solar and wind generation in electricity grids around the world. This in turn will help to reduce CO_2 emissions and begin to combat global warming. Vanadium Redox Flow Batteries are a great choice for energy storage as they are non-flammable, with long lifecycles of 20 years or more. However, currently the capital cost is too high limiting their deployment. The cost of the vanadium electrolyte is dependent on the demand for vanadium on the open market, which is dominated by demand for hardened steel. In contrast, improving the performance of carbon felt electrodes will lead to an increase in power density of the cells, reducing the cell cost.

Many treatments have been applied to carbon felts, with the aim of improving the inherent kinetics, surface area, wettability or conductivity. Typically, improvements in at least one area reported, however the source of improvements is not always assigned and often when it is the improvement is only qualitative. This is due to the complex and dis-ordered nature of the carbon felt electrodes which are typically used. In this work we have used single carbon fiber electrodes extracted from carbon felt samples, providing a defined cylindrical geometry and enabling quantative analysis of cyclic voltammetry and electrochemical impedance spectroscopy.

Single fiber electrode results were then extended to measurements at carbon felt. Numerical simulation of the carbon felt electrode were carried out by approximating the carbon felt as an array of cylindrical electrodes, with a specific void distribution. The analysis of the experimental results highlighted the importance of the void size distribution and supported the finding from single fiber measurements, that there was a rate constant distribution within the felt for the $Fe(CN)_6^{3-}$ / $Fe(CN)_6^{4-}$ redox couple.

Cyclic voltammetry of four different carbon fiber electrodes before and after thermal treatment at 450 ºC for 1 hour, showed that the rate constant for the $Fe(CN)_6^{3-}$ / $Fe(CN)_6^{4-}$ increased with thermal treatment. The capacitance of the carbon fiber electrodes also increased significantly, indicating that in part the increased kinetic performance was due to an increase in the wetted area of the electrodes, likely caused by the formation of pores at the carbon fiber surface. However, the magnitude of the apparent rate constant increase was significantly different to the increased capacitance at three of the four fiber types tested, indicating that functional groups at the surface strongly influence the kinetic performance.

Thermal treatment of three different felts showed a clear increase in the electrical double layer capacitance and physical area measured by BET. Therefore, the surface area and hence roughness of the fibers also increased. Cyclic voltammetry of the VO^{2+} / VO_2^+ redox couple showed improved kinetics and thus the increase in capacitance was linked to an increase in apparent kinetics for the VO^{2+} / VO_2^+ redox couple. As with the $Fe(CN)_6^{3-}$ / $Fe(CN)_6^{4-}$, the magnitude of the surface area increase was not consistent with the increase in the apparent rate constants. Therefore, the presence of different functional groups at the surface alters the kinetics of the reaction.

The apparent rate constants calculated from cyclic voltammetry of carbon felt electrodes were validated with half-cell polarization curve and charge / discharge measurements. With very close agreement observed between the rate constants calculated from cyclic voltammetry and polarization curve measurements. Finally, the charge / discharge measurements demonstrated that carbon felts with higher apparent rate constants for the VO^{2+} / VO_2^+ redox couple had higher energy efficiency.

Deputy Vice-Chancellor's Office

Postgraduate Office

UNIVERSITY OF CANTERBURY
Te Whare Wānanga o Waitaha
CHRISTCHURCH NEW ZEALAND

Co-Authorship Form

This form is to accompany the submission of any thesis that contains research reported in co-authored work that has been published, accepted for publication, or submitted for publication. A copy of this form should be included for each co-authored work that is included in the thesis. Completed forms should be included at the front (after the thesis abstract) of each copy of the thesis submitted for examination and library deposit.

Please indicate the chapter/section/pages of this thesis that are extracted from co-authored work and provide details of the publication or submission from the extract comes:

Chapter 4 is a reproduction of the publication:

Landon-Lane, L., A.T. Marshall, and D.A. Harrington, *EIS at carbon fiber cylindrical microelectrodes.* Electrochemistry Communications, 2019. **109**: p. 106566.

Please detail the nature and extent (%) of contribution by the candidate:

100% of the experimental work was done by the candidate. 10% of analysing the results and writing the paper was performed by the candidate. Harrington wrote majority of the paper.

Certification by Co-authors:

If there is more than one co-author then a single co-author can sign on behalf of all

The undersigned certifies that:

- The above statement correctly reflects the nature and extent of the PhD candidate's contribution to this co-authored work

Name: Aaron Marshall Signature: AMarshall Date: 6/8/2020

Deputy Vice-Chancellor's Office

Postgraduate Office

UNIVERSITY OF CANTERBURY
Te Whare Wānanga o Waitaha
CHRISTCHURCH NEW ZEALAND

Co-Authorship Form

This form is to accompany the submission of any thesis that contains research reported in co-authored work that has been published, accepted for publication, or submitted for publication. A copy of this form should be included for each co-authored work that is included in the thesis. Completed forms should be included at the front (after the thesis abstract) of each copy of the thesis submitted for examination and library deposit.

Please indicate the chapter/section/pages of this thesis that are extracted from co-authored work and provide details of the publication or submission from the extract comes:

Chapter 5 is a reproduction of the publication:

Landon-Lane, L., A.J. Downard, and A.T. Marshall, *Single fibre electrode measurements – A versatile strategy for assessing the non-uniform kinetics at carbon felt electrodes.* Electrochimica Acta, 2020. **354**: p. 136709.

Please detail the nature and extent (%) of contribution by the candidate:

100% of the experimental work was done by the candidate. 90% of analysing the results and writing the paper was performed by the candidate.

Certification by Co-authors:

If there is more than one co-author then a single co-author can sign on behalf of all

The undersigned certifys that:

- The above statement correctly reflects the nature and extent of the PhD candidate's contribution to this co-authored work
- In cases where the candidate was the lead author of the co-authored work he or she wrote the text

Name: Aaron Marshall Signature:  Date: 6/8/2020

Contents

1. Introduction

1.1. Energy Storage and Renewables

Renewable-energy sources have become significantly cheaper due to initiatives designed to tackle global warming and thus technologies such as solar and wind are being rapidly deployed, with 178 GW of renewable energy capacity installed in 2017, accounting for over two-thirds of global net electricity capacity growth [1]. The majority of this capacity growth was in the form of solar and wind technologies, which only provide power intermittently [2]. It has been reported that at high levels of penetration over 20%, these new technologies may destabilise electrical grids unless they are accompanied by energy storage [3]. In order to support the deployment of renewable electricity generation, highly efficient and cheaper methods of storing excess energy and providing power when needed is of critical importance.

1.2. Current State of Storage Technology

Many physical and chemical methods for storing electricity exist, however cost has typically been a barrier to large scale adoption, limiting the utility of these systems to specific scenarios [4]. Properties that are desirable for an economically feasible large-scale energy storage system include durability, low capital cost, low maintenance cost, safe design and high round trip efficiency. No one technology is likely to be superior in all aspects, but depending on the necessary application an optimal combination can be found [3].

1.3. Mechanical Energy Storage Technologies

Mechanical energy storage technologies store energy in the form of potential energy or kinetic energy. Pumped hydroelectricity storage (PHES) uses gravitational potential energy, compressed air energy storage (CAES) stores energy using elastic potential and flywheel energy storage (FES) uses kinetic energy.

1.3.1. Pumped Hydro Electricity Storage

PHES is the most mature form of electricity storage, with individual system sizes rated at larger than 100 MW power output and over 95 GW of total power capacity installed globally, as of 2010 [5]. PHES stores electricity in the form of hydraulic potential energy. Pumping water from a lower lake into a lake at higher altitude in PHES is analogous to recharging a battery. Pumping typically occurs during off-peak periods, when electricity demand and pricing is low. Generation is analogous to discharging a battery and occurs during peak periods, when electricity demand and pricing is high. Pumping and generating will generally follow a daily cycle, reducing the levelised cost of electricity produced. In New Zealand there are no PHES dams, however the naturally filled hydro lakes act as a demand buffer on a yearly cycle, typically entering winter peak periods full, then slowly emptying over approximately 12 weeks [6].

In New Zealand typically 65% of total electricity production is from hydropower [7], reducing the need for new forms of energy storage. However many other countries have a stronger imperative to develop and build new forms of energy storage, as only 17% of the world's electricity is produced by hydropower [8].

1.3.2. Compressed Air Energy Storage

Compressed air energy storage (CAES) uses air as a storage medium, air is compressed into underground caverns by an electrically driven compressor and electricity is then produced when the stored compressed air is released, driving a turbine generator. Individual projects are capable of storing over 1 GWh of electricity, making it an attractive grid scale energy storage option. However, the efficiency of current plants is below 54%, lower than both PHES and batteries therefore limiting its use [9].

1.4. Chemical Energy Storage Technologies

1.4.1. Lithium-ion Batteries

Conventional rechargeable lithium-ion batteries; found in cell phones, laptops and increasingly vehicles, provide a simple and efficient way to store electricity [10]. Recently large scale lithium-ion batteries have been deployed around the world, in particular where improved grid reliability is required, such as South Australia, South Korea and California [11]. These batteries have higher energy density than any other form of energy storage mentioned in this work, except for hydrogen. Higher energy density is desirable for portable applications, but for grid storage size is typically not a constraint, thus reducing the comparative advantage usually provided by this characteristic.

1.4.2. Lead Acid Batteries

Lead acid batteries are the most common batteries in the world, primarily used as starter batteries for internal combustion engine vehicles [4], due the low upfront cost of $175–250 per kWh. When used as an energy storage option to improve reliability, this upfront cost advantage is eroded due to the relatively short lifetime of 500-800 charge / discharge cycles [12].

1.4.3. Redox Flow Batteries

Flow batteries have been identified as promising technologies for providing large scale energy storage to support the increase of renewable electricity generation on the grid or through the development of micro-grids [13-15]. Many different variants of redox flow batteries exist, in particular all-vanadium, zinc-bromide, iron-vanadium and organic molecule based systems [16]. Each variant has underlying characteristics, as a result of the specific chemistry and cell design.

Redox flow batteries (RFB) utilise two liquid electrolyte solutions, each containing charge carrying compounds, typically in the form of metal ions, the most common form of which is the Vanadium Redox Flow Battery (VRFB), (Figure 1.1).

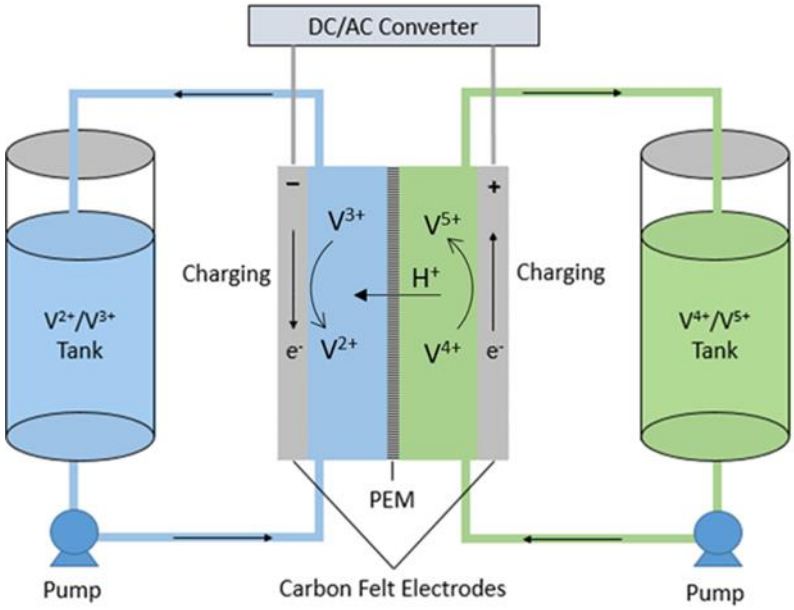

Figure 1.1: Vanadium redox flow battery (VRFB) schematic, adapted from [17].

In a VRFB, during discharge, V^{2+} is oxidized to V^{3+} in the negative electrolyte, with the electrons flowing through the external circuit to positive electrode where VO_2^+ is reduced to VO^{2+} in the positive electrolyte. While this redox reaction is occurring, hydrogen ions (H^+) diffuse across the ion exchange membrane, maintaining the charge neutrality and completing the circuit. To charge the VRFB, electrical work is provided from an external source; such as a renewable generator, in order to oxidise VO^{2+} to VO_2^+ and reduce V^{3+} to V^{2+}. During charging and discharging the charge carriers remain dissolved in the fluid electrolyte.

The electrolytes flow through porous electrodes, typically made from a carbon felt or paper. The electrodes are separated by a membrane, often a proton exchange membrane (PEM) such as Nafion. This allows protons to pass through, but limits cross-over of the charge carriers that store the energy. In order to charge and discharge the stored electrolytes they must be pumped from the tanks through the electrodes [18]. Current research topics include; organic redox couples for cheaper storage, development of lower cost membranes and improved electrodes for increased current density and cyclic efficiency [19-21].

1.4.4. Electrolysis and Fuel Cells for Hydrogen

The hydrogen economy is a term coined by proponents favouring the use of hydrogen as a storage medium. The basis of the hydrogen economy is that hydrogen can be formed by splitting water using electricity, then converted back to water in a fuel cell to produce electricity. One of the main advantages of this system is the high energy density of hydrogen when stored as a compressed gas or liquid. Battery technology is likely years away from overtaking the energy density of hydrogen, but the development of the hydrogen economy has been hampered by one major and fundamental disadvantage, low round trip efficiency [22], (Figure 1.2).

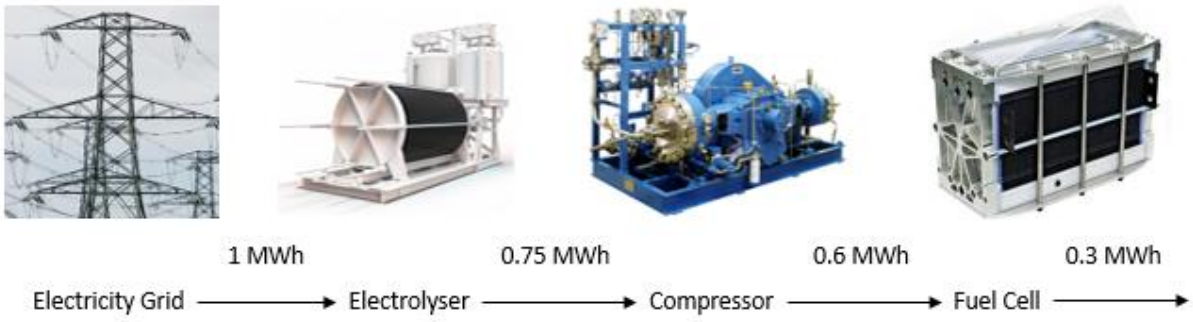

Figure 1.2: Indicative, major sources of round trip efficiency losses for use of hydrogen as an energy storage technology.

When making hydrogen electrochemically using an electrolyser, approximately 75% of the electricity is converted into hydrogen and when the hydrogen is converted back into water the efficiency can be below 50%.

Additionally, 15-35% of the stored energy is required to compress or liquefy the hydrogen, to enable higher energy density. Therefore, the resulting round trip efficiency is typically around 30% [22].

Due to the low round trip efficiency, the difference in price between the electricity used to produce hydrogen and the electricity produced when the hydrogen is converted back to water, must be significant. There appears to be no obvious solution to this problem, as the highest possible level of efficiency is set by the thermodynamic limit, at 83% [23]. The upper level of efficiency is not achievable in practice, as there will always be losses associated with the redox reaction overpotentials and electrical resistance within the cell.

1.5. Energy and Power

The different technologies previously mentioned have varying levels of energy and power density, governed by the chemical and physical processes behind their operation. The relative values for these characteristics can be viewed together, (Figure 1.3).

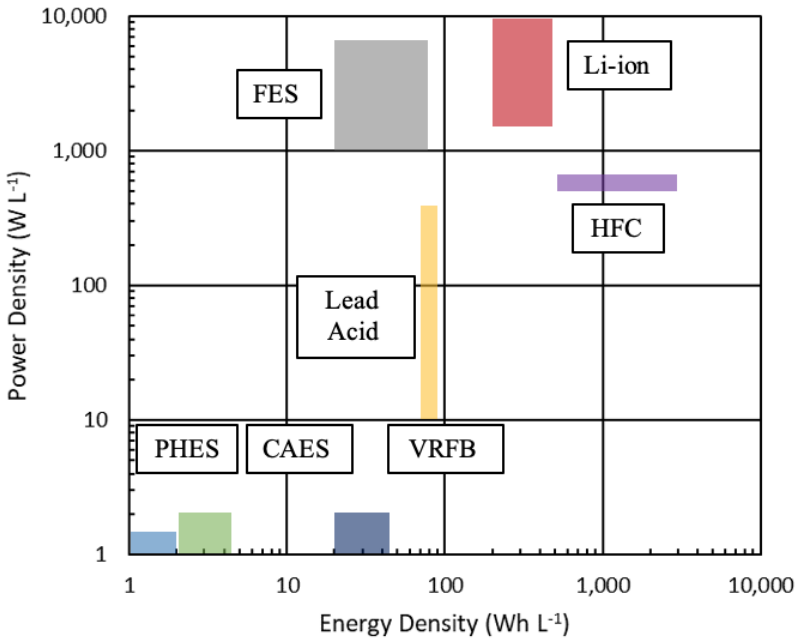

Figure 1.3: Energy and power density of various storage technologies, adapted from [24].

Li-ion and Fuel cells are towards the higher end for energy and power density, thus they are the natural choice for mobile transport applications [10]. The power and energy density of VRB is well below that of Li-ion, by approximately a factor of 1,000 and 10 respectively. However, the energy density of VRFB is around 10 times greater than PHES, which is the most common form of grid level storage, highlighting that in stationary applications energy density is not a critical parameter. The different forms of energy storage have varying characteristics, in particular rated power output and stored energy differ by storage type, (Figure 1.4).

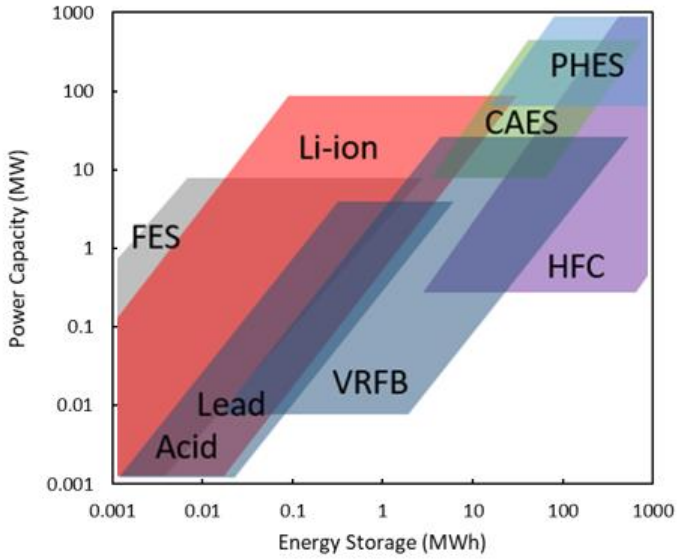

Figure 1.4: Power and energy scale of different storage technologies, adapted from [18].

Technologies shown to the top right of the graph can store large quantities of energy and meet high power demands. The relative position of different technologies on Figure 1.4 does not determine whether one technology is superior to another, it does however indicate the limitations of different technologies. Of note, PHS and CAES both have low power and energy density, but due to the large physical size of typical projects, higher levels of absolute power and energy are achievable. Li-Ion covers a larger area of the graph, indicating that it is suitable for use in a wide range of applications. Like Li-Ion, VRB have a wide range of applications, but tend to be used for longer time periods due to the low cost of energy storage and relatively higher cost of power capacity.

1.6. Levelised Cost of Electricity

In addition to the power and energy requirements for a project, the cost of storage is of importance. One measure is the upfront capital cost, measured in \$ kWh^{-1} or \$ kW^{-1}, however this does not account for the longevity and operating costs of the technology. The most useful metric to quantify the true cost of storage is the levelised cost of storage (LCOS), also measured in \$$kWh^{-1}$. Unlike the upfront cost, the LCOS considers the amount of energy delivered over the lifetime of the storage technology, not just the capacity for one discharge.

If the LCOS is below the expected difference in electricity price between charging and discharging over the project period, installing the storage technology will be economically viable. The main parameters that influence the LCOS are upfront cost, number of expected cycles, useful lifetime in years, round trip efficiency and the maintenance and operating costs [25]. Different methodologies will result in different final LCOS, as many variables are not set and depend on a range of factors. One such comprehensive study [26], has quantified the LCOS for a range of technologies and applications, notable values have been selected, (Table 1.1).

Table 1.1: Levelised cost of electricity for a transmission system sized at 100 MW and 800 MWh.

Storage Type	PHES	CAES	Li-Ion	VRFB	Lead Acid	Flywheel
LCOS (\$ MWh^{-1})	152-198	116-140	267 - 561	314-690	425-933	342-555

From Table 1.1, it is clear that battery storage technologies are more expensive than pumped hydro and compressed air storage. The cheapest form of chemical storage is Li-ion batteries, whilst installed capacity is significantly below pumped hydro, deployments are growing quickly [27]. The above values are based on a modelled system with 8-hour discharge duration and uses values from 2016.

For distribution services batteries are preferred as they can be installed almost completely independently of site [26]. Based on a 10 MW and 60 MWh system for distribution services, a Li-ion system would cost 272 - 338 $ MWh^{-1}, against 184 - 338 $ MWh^{-1} for a VRFB [26]. Whilst the difference in electricity spot price between charging and discharging is likely below this cost, batteries can provide other services to the grid, increasing total revenue [28], (Table 1.2).

Table 1.2: Electricity grid services that can be provided by energy storage systems, [28].

Service / revenue	Definition of service
Energy arbitrage	Average daily "off-peak" to "peak" market price changes.
Spin/non-spin reserves	Extra generating capacity available from generators connected to the grid.
Frequency regulation	Maintains the grid frequency at close to 50 Hz.
Voltage support	Maintains the voltages on the system within Code limits.
Black start	Restarts system after a blackout, generating station must self-start without using power from the grid.
Peaking capacity	Plants that run only during periods of high demand for electricity.
Transmission deferral	Savings made by deferring transmission upgrades.
Distribution deferral	Savings made by deferring local network upgrades.
Time-of-use	Encourages use of electricity when demand on the system is lowest.
PV self-consumption	Enables customers to source more of their energy demand from PV.
Demand charge reduction	For large commercial customers, reflects the extra cost of distribution equipment to service customers with high peak power demand.
Backup power	Provides power to a customer in the event of a blackout.
Demand response	Rewards customers who alter demand to reduce grid demands.

1.7. Thesis scope

VRFB have environmentally and social cost benefits relative to lithium-ion batteries, primarily due to the longer lifetime and ease of recycling. It can be seen that for grid storage applications VRFB are already cost competitive with lithium-ion batteries, but a greater understanding of the kinetics at the carbon felt electrodes is required. Each chapter is written in the form of a research paper and Chapters 4 and 5 have been published.

Chapter 2 - Vanadium Redox Flow Batteries Review

Chapter 2 provides an overview of the current design and performance of VRFBs. This covers each main cell component of VRFBs, as well as the effect of the electrolyte. From this review, we conclude that the carbon felt electrodes are currently limiting performance significantly.

Chapter 3 – Electrode Modifications

Chapter 3 details an array of different methods used to modify carbon felt electrodes, including metal deposition, metal oxide deposition, surface modifications and structural modifications. The relevant physical properties that change as a result of these modifications and how these changes influence electrode performance is also detailed.

Chapter 4 - EIS at Carbon Fiber Cylindrical Microelectrodes

The theoretical mass-transport impedance at cylindrical microelectrodes has previously been identified, but an experimental verification is given here for the first time. Nonlinear least squares fitting of the impedance spectrum of a redox couple at the reversible potential enables accurate evaluation of a composite parameter. From the composite parameter the standard rate constant and mean diffusivity was calculated, without needing to measure the fiber diameter, length or area.

Chapter 5 - Single Fibre Electrode Measurements - a Versatile Strategy for Assessing the Non-Uniform Kinetics at Carbon Felt Electrodes

The electrochemical performance of carbon felts is commonly tested by calculating the energy efficiency for charge / discharge cycles of electrochemical cells. This method whilst useful does not provide a direct measure for the kinetics of the redox reactions at the electrode surface. This work demonstrated that the kinetics of carbon felts can be directly measured using experimental cyclic voltammetry and simulations of individual carbon fibers and carbon felt.

Chapter 6 - Using Individual Carbon Fiber Electrodes to Quantify Effects of Thermal Activation

The electrochemical performance of four different carbon fiber types for the $Fe(CN)_6^{3-}$ / $Fe(CN)_6^{4-}$ redox couple before and after thermal activation is quantified. With calculations carried out using analysis of cyclic voltammetry discussed in Chapter 5 and the EIS modelling of cylindrical microelectrodes described in Chapter 4.

Chapter 7 – Thermal Activation of carbon Felt for the Positive Vanadium Redox Couple

The electrochemical performance of three different thermally treated carbon felts towards the positive VRFB redox couple (VO^{2+} / VO_2^+) was investigated, using the previously developed analytical methods described in Chapter 5. Thermal treatment improved the performance of all felts, likely due to increases in the electrically active surface area from increased surface roughness and improved wettability.

Chapter 8 – Half-Cell Performance of Carbon Felt Samples

Kinetic measurements of carbon felts from cyclic voltammetry in stagnant solutions were validated using half-cell measurements with pumped electrolyte. The results were consistent, as the felts that were found to have higher rate constants from cyclic voltammetry also had higher rate constants as measured from polarization curve analysis. Additionally, the felts with higher rate constants had higher efficiencies during charge / discharge measurements.

2. Vanadium Redox Flow Batteries Review

Vanadium redox flow batteries (VRFBs) have displayed promise for use in grid-scale energy storage, as they can store large amounts of energy with independent power capacity and no capacity loss for over 20 years [29]. This technology has been proven on the large scale and has the potential to become cheaper than lithium-ion and lead-acid batteries [16]. Wider adoption is currently hindered by a high upfront capital cost, that means the levelised cost of electricity is higher than the revenue the batteries can generate in most cases. Extensive reviews of VRFB covering a wide range of aspects have previously been published [12, 17, 29-53].

The purpose of this project is to better understand the kinetics of the redox reactions to enable future improvements in VRFB performance. Reductions in cost could be achieved by using cheaper materials or reducing the volume of materials required. Reductions in required materials can be achieved by improving performance of the cell through higher power density. Increasing power density can be achieved by improving the electron transfer kinetics of the electrode material, which are typically carbon felts.

Some advantages of all-vanadium battery design are related to the stability of vanadium at multiple oxidation states. This allows for vanadium to occupy oxidation states of V^{2+}, V^{3+}, V^{4+} and V^{5+}, thus if ions cross-over through the membrane, the round trip efficiency reduces, but the overall capacity of the battery is not affected [10]. Once the vanadium is dissolved in solution it will remain as vanadium indefinitely, thus the capacity of the battery will stay constant, unless precipitation occurs. If some of the vanadium precipitates it can be easily re-dissolved to restore the original capacity. This is a clear advantage relative to lithium ion batteries, which lose capacity over time and when recycled require the electrodes to be completely remade, which is a lot more expensive and energy intensive.

In VRFBs the power is produced in an electrolytic cell during discharge, with power consumed in the same cell during charging. In these cells, inert carbon felt electrodes are typically used and are separated by ion exchange membranes, to prevent ion crossover. Typically, graphite bipolar plates are used to enable stacking of electrodes, increasing the cell voltage. Current collectors made from highly conductive materials, such as copper are then wedged against end plates which provide structural support, (Figure 2.1).

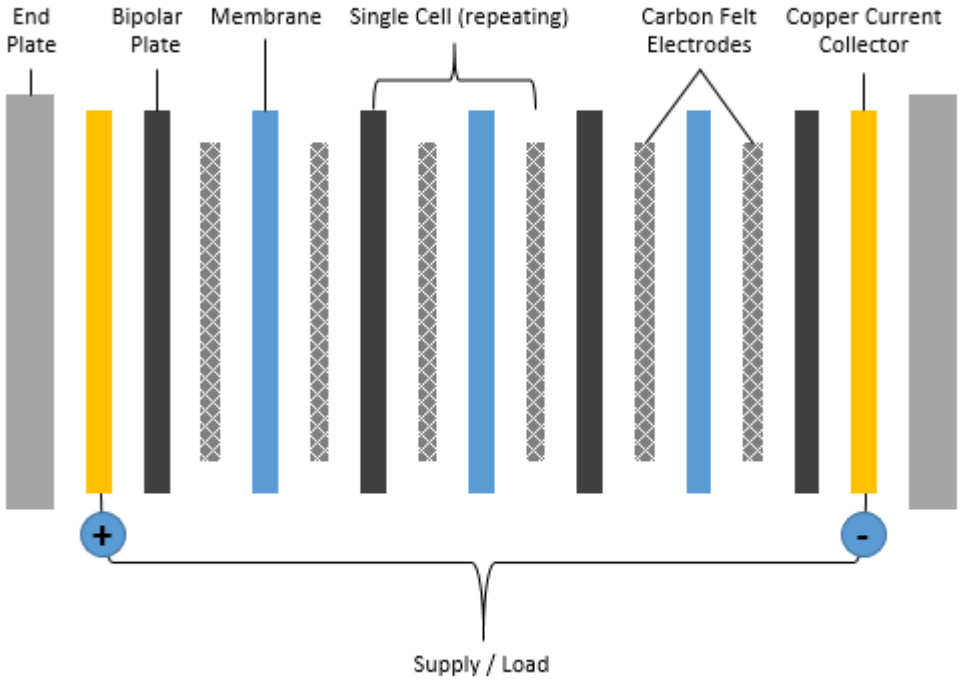

Figure 2.1: *Simplified cell structure of a typical RFB.*

2.1. Current Performance of VRFB

The stored energy capacity of a VRFB is defined by the amount of electrolyte, hence the minimum battery cost achievable is \$84 kWh^{-1} at 2015 market prices [25]. This price excludes the cell cost, but currently the full battery cost is as low as \$264 kWh^{-1}. The minimum levelised cost of electricity is \$184 MWh^{-1} when used for distribution services, which is equal to or cheaper than Li-ion [17]. The typical operating current density of approximately 100 mA cm^{-2} used commercially, which is well below hydrogen fuel cells of a similar design [54].

2.2. Electrochemical Processes within a VRFB

In a VRFB oxidation of V^{2+} and reduction of V^{3+} occurs at the negative electrode:

$$V^{3+} + e^- \rightleftharpoons V^{2+} \ (E^0 = \ -0.255\, V\ vs\ SHE) \tag{2.1}$$

The oxidation of VO^{2+} and reduction of VO_2^+ occurs at the positive electrode and is also a one electron transfer reaction:

$$VO_2^+ + 2H^+ + e^- \rightleftharpoons VO^{2+} + H_2O \ (E^0 = \ +0.991\, V\ vs\ SHE) \tag{2.2}$$

Many applications will require higher voltages, thus cells are often connected together by bi-polar plates, mechanically in parallel but electronically in series to create stacks with higher voltages.

For the redox couples described in Equations 1 and 2, the reversible cell potential, E_{rev} can be found from a modified verison of the Nernst equation. During charging and discharging the state of charge (SOC) of the battery is constantly changing, this influences the reversible cell potential, as the concentration of each vanadium ion depends on the SOC. As two protons participate in the reduction of VO_2^+, the reversible cell potential is related to the log of the squared proton concentration. Additionally, with the Donnan potential which accounts for differences in the proton concentration across the membrane, between the positive and negative electrolyte [55, 56]:

$$E_{rev} = E^0 + \frac{RT}{nF} ln\left(\frac{C_{VO_2}{}^+ . C_{V^{2+}} . \left(C_{H^+}^{pos}\right)^2 . C_{H^+}^{pos}}{C_{VO^{2+}} . C_{V^{3+}} . C_{H^+}^{neg}}\right) \tag{2.3}$$

2.3. Performance Limiting Aspects of VRFB

As previously mentioned, key characteristics for an effective energy storage system include high roundtrip efficiency, low cost and long term reliability. Whilst VRFB can store energy at a reasonable cost, the roundtrip efficiency is below that of Li-ion and the cost of power is dependent on the cell cost. By looking at the underlying principles, it is possible to identify areas to improve both of these characteristics. There are three main efficiency losses in VRFB, concentration polarization, η_{con} from mass transfer limitations, electrode activation overpotential, η_{act} required to increase the current density and ohmic losses from electrical resistance. Therefore, the cell potential during charging is greater than the reversible cell potential:

$$E_{cell} = E_{rev} + \eta_{con} + \eta_{act} + IR \tag{2.4}$$

Where: IR is the voltage drop from sources of resistance within the cell, including across the membrane, within the electrodes and the current collector. These values depend on a range of variables and can be estimated based on empirical data [57]. During discharging the cell potential is below the reversible potential, as the positive signs in Eq. 2.8 are replaced with minus signs. The difference in potential between charging and discharging can be used to calculate the voltage efficiency, VE of the cell:

$$VE = \frac{E_{cell_{discharge}}}{E_{cell_{charge}}} \tag{2.5}$$

The cell potentials in Eq. 2.9 are the average potential for the duration of the charge / discharge cycle. Energy efficiency of the cell can be reduced further by the presence of unwanted side reactions and crossover of vanadium ions through the membrane. The most common side reaction in a VRFB is the parasitic hydrogen evolution reaction at the negative electrode, although water splitting and carbon oxidation can occur at the positive electrode. Therefore, the coulombic efficiency, CE (also known as the Faradaic efficiency) is defined as ratio of the usable charge to the amount of charge stored intially:

$$CE = \frac{C_{discharge}}{C_{charge}} \tag{2.6}$$

However, this efficiency is very sensitive to the cell voltage limits and current density applied during the operation of the battery. The overall energy efficiency, EE is the ultimate measure of battery performance and is the product of the voltage and coulombic efficiency:

$$EE = CE \times VE \tag{2.7}$$

2.4. Electron Transfer Kinetics

Improving the kinetics of the vanadium redox reactions can improve the voltage efficiency through reduced electrode activation overpotentials. The reduced cell potential therefore can also improve the coulombic efficiency by reducing the cell potential, limiting the amount of charge that goes towards the unwanted side reactions. Combined this can have a dramatic effect on the overall energy efficiency of the cell.

The electron transfer kinetics depend on the overpotential applied to the electrodes and the rate constant for the reaction. The rate of the forward reaction is given by:

$$k_f = k_f^0 \, exp^{-anF(E_{cell}-E_{rev})} \tag{2.8}$$

Where kf, is the rate of the forward reaction, α, is the charge transfer coefficient, n, is the number of electrons transferred during the oxidation and reduction reactions, F, is Faraday's and $E - E_{rev}$, is known as the electrode activation overpotential, also denoted as η_{act}. When considering the reaction in both the forward and reverse directions, the net electron transfer rate at a surface can be calculated using the Butler-Volmer equation:

$$i = FAk^0 \left(C_{Red} e^{\frac{-\alpha nF(E-E_{rev})}{RT}} - C_{Ox} e^{\frac{(1-\alpha)nF(E-E_{rev})}{RT}} \right) \tag{2.9}$$

Where i, is the current, A, is the surface area of the electrode, k^0, is the standard rate constant, C_{Red}, is the concentration of the reduced species at the surface of the electrode, C_{Ox}, is the concentration of the oxidised species at the surface of the electrode, R, is the universal gas constant and T, is the temperature of the system, measured in kelvin.

Thus, the current density is proportional to the standard rate constant, but exponentially related to the overpotential. Operation of a cell is deemed to be kinetically limited if the current density is below the mass transfer limit. Improving the electron transfer kinetics leads to a larger k^0 value, enabling larger current densities at a given overpotential, or requiring a lower potential to achieve the same current density.

2.5. Mass Transfer

Mass transfer relates to the movement of the ions from the solution to the electrode surface. The rate of mass transfer to the surface can limit the current and hence power density. The current density becomes limited by mass transfer when the electron transfer kinetics are fast, occuring at large overpotentials. As reactants are quickly consumed at the surface the concentration of reactants at the surface reduces, reducing the current as defined in Eq 2.9 [58]. In a stagnant solution the only form of mass transfer is from diffusion, with the rate of mass transfer dependent on multiple variables, including the diffusion coefficient of the ions in solution, the concentration of ions and the solution temperature and viscosity [59]. When the solution is forced through an electrode, convection is the dominant source of mass transfer and is dependent on the flow rate of solution and the cell geometry [60].

During charging and discharging of VRFB the vanadium reactant species must be transported to the carbon felt electrode surface to enable high power densities in the cell. This becomes very challenging at both high and low SOC, as the concentration of the reactant is reduced significantly. If the mass-transport becomes too limited it can cause electrode degradation from oxidation, gas formation and a reduction in efficiency. Battery management systems are often used to control the current and electrolyte flow rate, managing pumping losses from increased flowrate whilst maintaining sufficient power output. At these extreme SOC conditions the power density of VRFB systems becomes limited and is termed concentration polarization [31, 61]. As a result, the concentration overpotential, η_C becomes the main source of energy loss within the cell, which is typically dominated by kinetic and contact resistance losses. The limiting current density i_L, is defined as [61]:

$$i_L = nFk_mC_b \tag{2.10}$$

Where C_b is the bulk reactant concentration and k_m is the local mass transfer coefficient, which is a function of the convective fluid velocity, v [61]:

$$k_m = 1.6 \times 10^{-4} v^{0.4} \tag{2.11}$$

2.5.1. Electrolyte Considerations

Whilst the cost of the vanadium electrolyte is essentially fixed by the market price for vanadium, the performance of a VRFB is heavily influenced by the chosen electrolyte [43]. Typically, vanadium ions are dissolved in sulphuric acid, with the maximum concentration of vanadium limited by the lowest solubility of the four different redox states, within the chosen operating temperature range. The solubility of the V^{2+}, V^{3+} and V^{4+} ions increase with increasing temperature, but decrease with increased sulphuric acid concentration. The decrease in solubility with sulphuric acid is due to the common-ion effect, whereby each of these vanadium redox states precipitate as vanadium sulphate salts. However, the solubility of the V^{5+} ion decreases with temperature and increases with sulphuric acid concentration, as the V^{5+} species precipitates as V_2O_5. The electrolyte concentration is typically 1.6 – 2 M of vanadium and 2 – 5 M sulphate, with higher sulphate recommended for operation in warmer climates.

Using a mixed electrolyte with hydrochloric acid and sulphuric acid enables higher vanadium concentrations, by reducing the common ion effect. However, the presence of Cl^- ions in the electrolyte introduces a significant safety issue. During charging the cell potential increases and as the SOC approaches 100%, the charging becomes mass transfer limited and the overpotential increases. If the potential goes too high, Cl^- ions will be oxidised to form Cl_2, a toxic gas. The performance advantages of the mixed electrolyte however are significant, with a stable 2.5 M vanadium concentration. This increased concentration reduces concentration polarization losses, increasing the efficiency, power density and energy density of the battery.

Addition of phosphoric acid has been shown to increase the kinetics for the positive redox couple. The apparent rate constant for the VO^{2+} / VO_2^+ redox couple in a 1 M solution of phosphoric acid was 6.1×10^{-4} cm s^{-1}, 70 times larger than the 9.2×10^{-6} cm s^{-1} recorded with a 1 M sulphuric acid solution. When a mixed acid electrolyte of 0.5 M phosphoric and 0.5 M sulphuric was used, the rate constant was still significantly higher at 1.2×10^{-4} cm s^{-1}. As the phosphoric acid is not consumed this is a form of homogenous catalysis, which may be the result of the phosphate ion forming a complex that increases the inherent rate constant [62].

2.5.2. Felt compression

Previous research has demonstrated that felt compression and the resulting porosity of felt electrodes in assembled VRFB cells alters the performance of the cell. One study showed that the coulombic efficiency (CE) was highest at a compression of 38.5%, relative to the other ratios tested (23.1 % and 53.8%). The voltage efficiency was the same at 38.5% and 53.8%, both higher than at 23.1%. The improved VE at higher compression was likely due to a reduction in the ohmic resistance of the felt. The highest EE recorded was 73% at 38.5% compression and an operating current density of 80 mA cm^{-2}, with an electrolyte flow rate of 100 mL min^{-1} [63]. These improvements in electrical efficiency do however, come at a cost of increased pumping energy expenditure. Due to the lower porosity, the pressure drop through the felt from pumping is increased and thus more energy is required to force the electrolyte through the felt [64].

2.5.3. Flow Fields

VRFB cells typically have a flow field machined into the bipolar plates to improve the convective mass transport through the carbon felt or paper electrodes. The flow fields distribute the electrolyte more evenly through the electrodes, improving electrical efficiency and reducing pressure drop. Many different flow fields have been tested in the highly developed area of fuel cells [65-72] and these flow field designs are often applied to VRFB cell flow fields [73, 74]. Some common flow field designs include flow through (no machined pattern), parallel, serpentine and interdigitated patterns [75], (Figure 2.2).

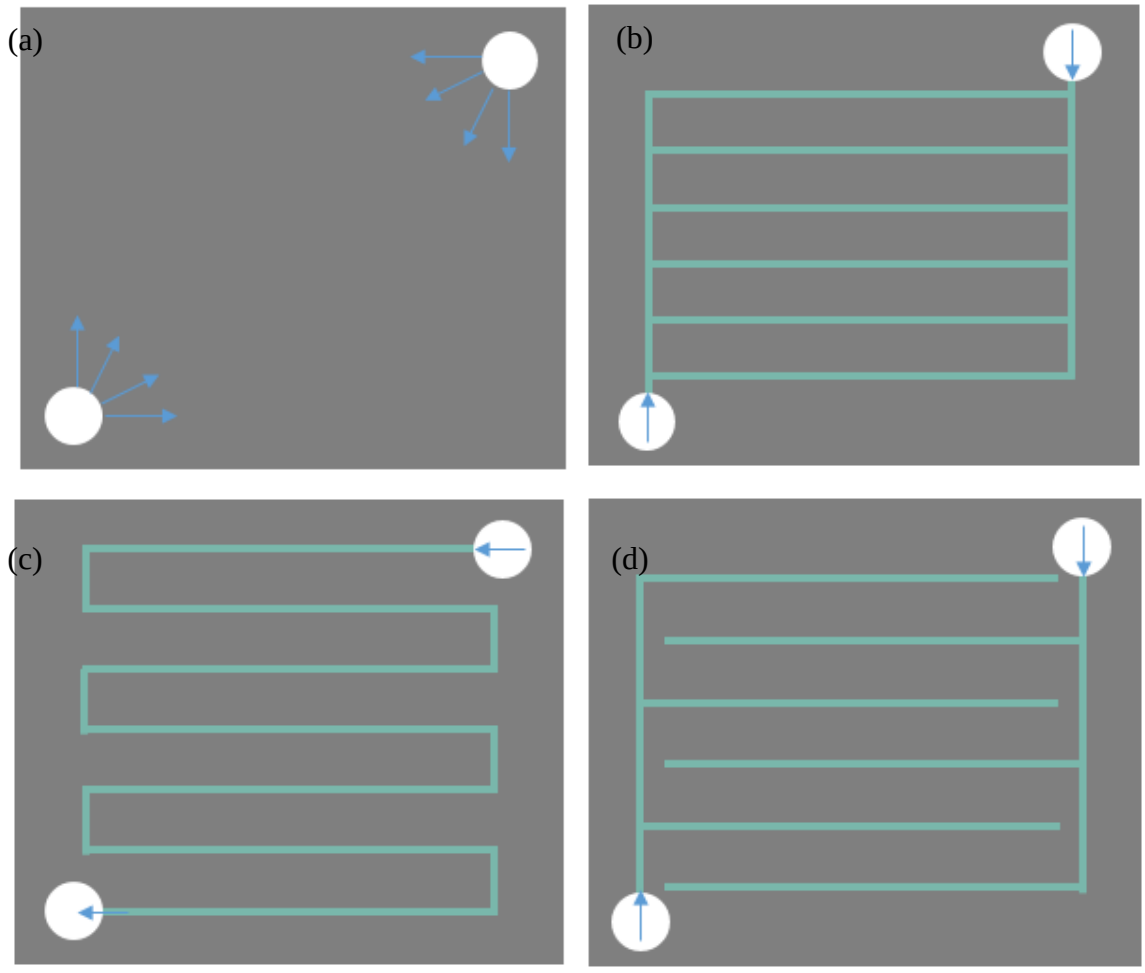

Figure 2.2: The main type of flow patterns machined into bipolar plates, blue arrows indicate direction of electrolyte flow. a) Flow through, b) parallel, c) serpentine and d) interdigitated.

The performance of a VRFB cell with a serpentine flow field was compared to a flow through design. The serpentine flow field improved the distribution uniformity of the electrolyte and reduced the overpotential in the electrode. The cell with the serpentine flow field had an energy efficiency of 80.7% at 40 mA cm^{-2} and 2.5 mL s^{-1}, outperforming the cell with flow through design which returned a maximum energy efficiency of 75.9% at 40 mA cm^{-2} and 1.2 mL s^{-1}. This higher energy efficiency of the serpentine flow field is significant enough to overcome a 1% higher pumping cost, relative to the flow through design [76].

VRFB cells with interdigitated flow fields have been demonstrated to outperform cells with flow-through carbon electrodes. Thicker electrodes are required in flow through configurations to reduce the pressure drop, the thicker electrodes increase the ohmic losses due to contact resistances, lowering the performance of the cell. When scaled up to larger active area electrodes, the pressure drop increases less for interdigitated flow field configurations and thus they are more suited for use in large cells with higher power output [77]. However, analysis of a range of different interdigitated variants showed that they were susceptible to poor distribution of electrolyte within the cell and therefore the performance is typically below that achievable using serpentine flow channels in large cells [78].

New methods to improve electrolyte distribution through electrodes include the use of static mixers and toroidal cell designs [79]. Toroidal cell designs using wedge-shaped cells enables varied felt compression, with higher electrode compression at the outlet, optimising the material properties through the cell. Wedge cells tested without mixers had smaller overpotentials than traditional parallel plate designs and resulted in a 15% increase in energy efficiency. This in turn increased the energy capacity, due to larger depth of charge and discharge between voltage cut-offs. The addition of static mixers can further improve mass transport, with minimal increased pumping cost by reducing the concentration gradients across the cell. It is expected that with the addition of static mixers, energy efficiency improvements of over 20% could be achieved.

2.6. Effect of Improving Kinetics on Economic Viability

As the vanadium electrolyte price is dominated by the market price of vanadium, changes to the design and operation of the electrolytic cell are most likely to improve the economic viability of the VRFB. The estimated costs for the cell components depicted in Figure 2.1 vary significantly, (Table 2.1).

Table 2.1: Cost breakdown of some common VRFB components, retrieved from [80].

Component	Cost ($ kW^{-1})
Carbon Felt	70
Membrane	500
Bi-polar Plate	55
Current Collector	0.15
End Plate	0.2

From Table 2.1, it is clear that the cost of membranes is the most significant factor in terms of $\$kW^{-1}$. The total membrane cost could be decreased by reducing the purchase price in $\$ m^{-2}$, or by increasing the power density of the cell. Cells with higher current density would require smaller membranes, electrodes and auxiliary equipment [81]. Reducing the size of the cell would require the operating current density to increase beyond 100 mA cm^{-2}, that is typically used commercially [54].

The biggest hurdle to increasing current density is the electrode kinetics of the carbon felt. In many cases electrode kinetics are too slow for practical use, but can be improved using electrocatalysts or electron-transfer mediators [41]. The limiting current for redox flow batteries is dependent on flow rate and flow field design and can range from 200 $mAcm^{-2}$ to over 600 $mAcm^{-2}$ [82-84]. Thus, the development of electrodes with higher activity could reduce the cost of producing VRFBs.

Doubling the cell power density would reduce the price per kWh of a 5-hr charge/discharge system significantly [54]. Improving the electrode kinetics not only decreases the cell stack cost, it can also improve the efficiency and SOC window under which the VRFB can operate. Both the improved efficiency and increased SOC reduce the cost per kWh of electrolyte, as the same electrical energy storage capacity can be achieved using less vanadium [85].

2.7. Membrane Technology

Ion exchange membranes of the Nafion type have been identified as the most expensive component in VRFB, costing \$500 m^{-2} and contributing up to 44 % of overall battery cost [80]. Alternative membranes are being considered, namely SPEEK and size exclusion membranes [20]. Membranes should limit cell resistance, maintain high selectivity to prevent crossover losses and have high durability for long lifespan for thousands of cycles [86]. One option is to add a microporous separator to limit crossover through a 20 micron thick Nafion membrane, this is claimed to maintain good selectivity whilst reducing resistance [87]. Membrane improvements can work synergistically with improved kinetic performance to decrease the cell stack size, increase efficiency and improve the overall economic viability of VRFB.

3. Electrode Modifications

Redox Flow Batteries research almost exclusively uses carbon based electrodes in experimental work. Some fundamental work has been carried out using planar glassy carbon (GC) electrodes, allowing for easier calculation of parameters such as the diffusion coefficient and the inherent rate constant. However, the most common form of electrode used in working cells is carbon felt. Others have used carbon paper electrodes in no gap architecture derived from fuel cell designs, which reduces electrical resistance but increases electrode activation losses. The choice of carbon materials for the electrodes is informed by the widespread use in industrial scale VRFB. Carbon felt is often chosen due to a number of positive properties

- Low cost and widely available carbon material (Polyacrylonitrile (PAN) and Rayon based fibers)
- Inert to corrosion from the highly acidic and oxidative electrolytes
- Mechanical stable and can handle the typical flow rates
- Suitable porosity with reasonable surface area

3.1. Electrode properties

Whilst carbon felt electrodes are suitable for use in VRFB cells, they can be improved further by manipulating the following properties:

- Increasing this inherent rate constant
- Increasing the surface area of the electrode through a rougher / more porous surface
- Improving the wettability of the electrode to increase the electro active surface area
- Improving the conductivity of the electrodes to reduce ohmic losses.
- The coloumbic and hence energy efficiency of a cell can also be improved by suppressing hydrogen evolution at the negative carbon felt electrode

It has been shown that the inherent rate constant for vanadium redox reactions is well below that of other common redox couples such as iron and ferricyanide [88, 89]. There is growing evidence that the V^{2+} / V^{3+} redox reactions are kinetically slower than the VO^{2+} / VO_2^{+} reactions.

Increasing the electrode roughness is analogous to increasing the inherent rate constant, as the current density is linearly related to both, Equation 2.9. However, the electroactive surface area of the electrode is dependent on the physical surface area of the electrode as well as the wetted fraction. Therefore, the performance improvements from increasing the surface area through increased roughness will only be realised if the increased physical area is also wetted by the electrolyte.

The importance of carbon felt wetting on reaction kinetics has been previously demonstrated, electrolyte containing V^{2+} / V^{3+} was forced through a carbon felt electrode in a flow channel. The electrode was then removed from the flow channel and immersed in a stagnant solution of the same electrolyte. During cyclic voltammetry a significant increase in the peak current during oxidation was observed. The higher peak current was assigned to increased wetting, filling the internal pores and not changes to the inherent kinetics, surface roughness or conductivity [90, 91].

Reduction of protons to form hydrogen gas at the negative electrode lowers the coulombic and energy efficiency of the cell. Hydrogen formation occurs as a parasitic side reaction because the standard reduction potential of the V^{2+} / V^{3+} reaction is below that of the hydrogen evolution reaction [92]. Therefore, inhibiting the formation of hydrogen at the carbon felt electrode will have a positive influence on overall cell performance. Addition of nitrogen functional groups on the carbon felt surface has been shown to promote the hydrogen evolution reaction, thus a low nitrogen surface content is desirable for the negative electrode [92, 93].

In this review each of these properties will be discussed in relation to many of the different electrode modification methods described in literature. These modification methods have been grouped into four distinct categories:

- Metal deposition onto electrode surfaces
- Metal oxide deposition onto electrode surfaces
- Chemical and thermal surface treatments
- Structural modification of the electrode

Structural modifications are differentiated from chemical and thermal surface treatments by defining them as the addition of non-metallic material to the carbon electrode surface, typically a different form of carbon that may contain other elements such as nitrogen and oxygen.

3.2. Metal Deposition

Metal deposition is the process of depositing metallic compounds onto a carbon electrode surface. Metals can be electrodeposited with under or over potential deposition, whereby under-potential deposition occurs at electrode potentials above the Nernstian potential [94-98]. Metal impregnation of porous carbon and attachment of metallic nanoparticles have also been used to deposit metals onto carbon surfaces [99-111]. Some important considerations with metal deposition include the cost of the metals, as noble metals such as Pt, Au and Ag are typically expensive [112]. The method of deposition is also important as the deposited metal must be stable, as VRFB typically have decades long lifecycles. As previously mentioned the kinetics of the hydrogen formation reaction are important for the energy efficiency of the cell, it is known from hydrogen electrolyser literature than many metals catalyse this reaction and these would therefore not be suitable for use in VRFB [113]. Whilst water splitting at the positive electrode is not as commonly a problem as hydrogen formation, due to the higher standard reduction potential, use of metal deposition at the positive electrode only is ill advised. If the deposited metal detaches or dissolves from the surface of the positive electrode, over time these metals may migrate to the negative electrolyte and lead to increased rates of hydrogen formation.

3.2.1. Inherent Kinetics

Metal deposition has been shown to improve the inherent kinetics, with a strong focus on bismuth deposition. One paper showed that bismuth nanoparticles improved the electroactivity of the negative electrode for a graphite felt and a carbon felt, observed through cyclic voltammetry [102]. Whilst another paper demonstrated that at the positive electrode bismuth dissolves to form Bi^{3+} in solution and does not alter electrode kinetics, but when the bismuth is deposited at the negative electrode increased peak currents and reduced peak separation was recorded during cyclic voltammetry. These results were confirmed by a smaller charge transfer resistance measured by electrochemical impedance spectroscopy (EIS). The optimum loading was found to be 2 wt.%, returning an energy efficiency of 79% at a current density of 160 $mAcm^{-2}$ for over 300 cycles [105].

The effectiveness of bismuth deposition was improved by etching carbon felt with KOH before depositing bismuth nanoparticles. The etching produced micropores and oxygen-containing surface groups that increased bismuth deposition. The KOH etched and bismuth deposited electrodes returned smaller peak separations in cyclic voltammograms (CVs) and reduced charge transfer resistance as measured by EIS. An energy efficiency of 79.3% was achieved at a current density of 160 $mAcm^{-2}$, which was 36.2% higher than with an unmodified carbon felt electrode [106]. Another group electrodeposited bismuth nanoparticles onto graphite felt and observed improved kinetics from cyclic voltammetry. They proposed that Bi nanoparticles form an intermediate BiHx, which in turn reduces V^{3+} to V^{2+}, subsequently inhibiting the formation of hydrogen and improving coulombic efficiency [101].

In addition to bismuth, tin was deposited in-situ by dissolving 0.02 M or less into the negative vanadium electrolyte. As the tin is deposited a clear increase in kinetics was observed during cyclic voltammetry [98]. Using a similar in-situ electrodeposition method, antimony (Sb^{3+} ions) were added to the vanadium electrolyte solution. An optimal concentration of 5 mM was found and as the Sb^{3+} ions were reduced onto the negative electrode, a decrease in the charge transfer resistance was measured by EIS. The energy efficiency of the cell was increased to 67.1% from 57.5% at a current density of 120 $mAcm^{-2}$ to 67.1% [107].

3.2.2. Surface Area and Roughness Effects

Bismuth nanoparticles 35-50 nm in diameter were attached to graphite felt by immersion in a Bi_2O_3 solution, with a 1% loading by weight achieved after immersion. The felt was then treated thermally at 450 ºC in air for 3 hours and the surface area increased from 0.92 m^2g^{-1} for a thermally treated graphite felt, to 3.36 m^2g^{-1} for the felt that was immersed in bismuth and then thermally treated. It was hypothesized that the bismuth nanoparticles catalysed the oxidation of the graphite felt. An increase in electrode conductivity was also observed, contributing to the improved performance [103].

Copper nanoparticles were formed on graphite felt before use as a negative electrode with in-situ electrodeposition. $CuSO_4$ was added to the negative vanadium electrolyte in 0, 0.0025, 0.005 and 0.01 M concentrations. Cyclic voltammetry showed a small increase in peak current, possibly due to increased wetting, but no change in peak potential separation was recorded. However, EIS measurements showed a 49% reduction in charge transfer resistance, which could be achieved if the electrically active surface area of the electrode had doubled, but there appears to have been no attempt to measure this [110].

3.2.3. Electrode Wettability

Pt and $CuPt_3$ nanocubes approximately 5 nm in size were deposited via drop casting onto separate hydrazine treated graphene oxide electrodes. Both catalysts performed better for the VO^{2+} / VO_2^+ redox couple than a hydrazine treated graphene oxide electrode without deposited nanoparticles. The $CuPt_3$ electrode was more active than the Pt electrode, which was believed to be a result of a 105% increase in electroactive surface area, whereas the area only increased by 32% for the Pt modified electrode [108, 109]. The increase in electrically active surface area of the $CuPt_3$ modified graphene oxide electrode relative to the Pt modified electrode may have been due to improved wettability, as a result of the formation of –OH groups at the Cu–Pt surface from water dissociation [108]. Indium deposited on carbon paper improved electrode performance, increasing the limiting current from 72 mA cm^{-2} to 125 mA cm^{-2}. This was likely due to the increase in wettability observed from contact angle measurements [100].

3.2.4. Electrode Conductivity

Iridium was reduced onto graphite felt using pyrolysis and tested as a positive electrode in a VRFB. It was found that the electronic conductance of the felt increased and accompanied a reduction in cell resistance and an improved cell energy efficiency [114].

3.3. Metal Oxide Deposition

Metal oxides have been deposited onto carbon surfaces to act as catalysts for the vanadium redox reactions. As with metal deposits, electrodeposition can be employed to deposit metal oxides [115, 116]. Hydrothermal and solvothermal processes for attachment of metal oxides have been studied [117, 118]. $KMnO_4$ was co-reduced with graphene oxide in the presence of NH_3 before the solution was drop cast onto a GC electrode [119].

3.3.1. Inherent Kinetics

A solvothermal Mn_3O_4 / multi walled carbon nanotube (MWCNT) modified graphite felt electrode was credited with improving the electrocatalytic kinetics for the VO^{2+} / VO_2^+ redox reactions. However, no attempt was made to identify changes in electrically active surface area and therefore the improvements in electrochemical performance may have been due to an increased electrically active surface area not faster inherent kinetics [118]. Graphite felt modified by hydrothermal deposition of MnO_2 was shown to have improved electrocatalytic activity towards the VO^{2+} / VO_2^+ redox couple. This was identified through a reduction in peak separation during cyclic voltammetry and a 12.5% increase in energy efficiency, at a current density of 150 mA cm^{-2}. However, once again no mention of surface area or capacitance was made and thus it is possible improvements were solely from increased electrically active surface area [117].

3.3.2. Surface Area and Roughness Effects

Electrochemical reduction of functionalized MWCNTs and $W_2O_{11}^{-2}$ onto a graphite plate was shown to form a nanoporous structure with a large specific surface area. Subsequent cyclic voltammetry measurements showed a noticeable reduction in peak separation for the VO^{2+} / VO_2^+ redox couple, highlighting the importance of the electrically active surface area [116].

3.3.3. Electrode Wettability

No mention of electrode wettability was made in the metal oxide deposition that was reviewed, though not every piece of research has been covered. Whether this lack of emphasis is because there is no obvious link between the tested metal oxide deposition methods and electrode wettability, or because researchers are not widely aware of the importance of electrode wettability is unknown.

3.3.4. Electrode Conductivity

Deposition of metal oxides is not aimed at improving electrode conductivity, due to the typically poor conductivity typical of metal oxides. Therefore, many of the methods used to attach metal oxides also use carbon nanotubes to act as a conductive bridge between the oxide particles and the underlying carbon electrode [118].

3.4. Chemical and Thermal Surface Treatments

Chemical and thermal surface treatments are commonly used and have been extensively studied. Thermal and chemical treatments in particular can be easily carried out, often requiring only one step and minimal preparation, making them very suitable for use on an industrial scale. Chemical modifications are typically achieved through exposure to concentrated acids which oxidise and acidify the surface. Electrochemical treatment can accelerate surface modifications, by applying highly oxidising and or reducing potentials to the electrodes. Thermal treatments are often carried out in an air atmosphere at a range of temperatures, as the presence of oxygen means the formation of oxygen groups at the carbon surface can be achieved, although inert atmospheres are also occasionally used.

3.4.1. Inherent Kinetics

An alkaline mediated hydrothermal process was applied to a carbon cloth, increasing the number of oxygen containing functional groups. The increase in functional groups did not change the surface area, as the increase in capacitance that was observed was attributed to pseudo-capacitance from redox reactions of quinone / hydroquinone groups on the surface. From cyclic voltammetry little to no change in peak separation for the VO^{2+} / VO_2^{+} reaction was observed, but there was a noticeable decrease in peak separation for the V^{2+} / V^{3+} reaction [120].

Chemical treatment of carbon fibers was carried out by boiling graphite felt in highly concentrated solutions of sulphuric acid, nitric acid and mixtures of both acids for 3 to 15 hours [121]. The felts treated with sulphuric acid alone had the lowest cell resistance, with the improvement in performance attributed to the formation of oxygen functional groups at the surface. The functional groups C-OH and C=OH were observed via XPS and the following 3-step reaction mechanism was proposed, Figure 3.1.

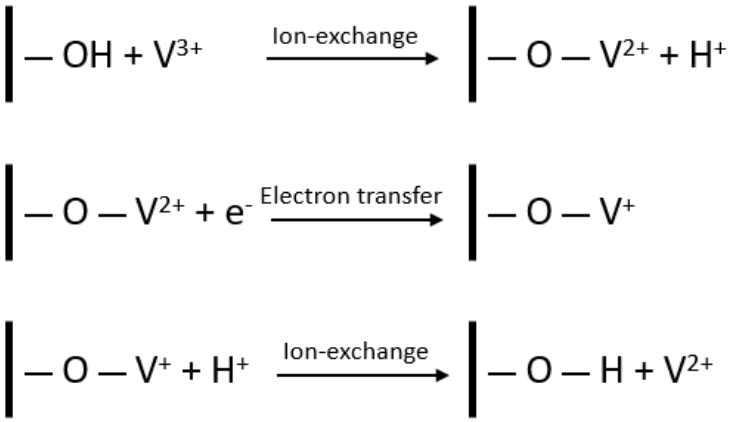

Figure 3.1: Reaction mechanism proposed by [121] to explain the improved kinetic performance of a sulphuric acid treated graphite felt electrode.

The increase in surface oxygen functional groups may have also increased the felt hydrophilicity and subsequently the electroactive surface area.

Electrochemical pre-treatment of carbon fibers is one method that has been carried out to influence the performance of carbon based electrodes. One such treatment involved cycling carbon fiber micro-electrodes in 1 M Sulfuric acid, with a potential sweep from -1.0 V to 2.0 V vs a saturated calomel electrode at 20 V s^{-1} for 5 minutes [122]. The potential limits applied enabled the electrode to be oxidised at the higher potentials, before being reduced at the lower potentials [123]. The electrochemical pre-treatment was found to improve the heterogeneous electron transfer rate for the redox reactions of methylene blue [122].

Carbon fiber microelectrodes were used to simplify the complexities involved with kinetic analysis of carbon felt materials. Linear sweep voltammetry and electrochemical impedance spectroscopy analysis methods were used to calculate the rate constant for the V^{2+} / V^{3+} and VO^{2+} / VO_2^+ redox couples, as well as the effect on kinetics of electrochemical oxidation and reduction. It was found that electrochemical reduction inhibits the kinetics of V^{2+} / V^{3+} redox couple, but enhances the kinetics of VO^{2+} / VO_2^+. These changes were assigned to inherent kinetics of different functional groups, as the capacitance was consistent during testing after a pre-treatment procedure was carried out. XPS analysis demonstrated that electrochemical oxidation increased the oxygen content on the surface. Interestingly, there was a clear difference in treatment potential between activation and de-activation. For instance, electrochemical reduction below -0.3 V, relative to a mercury sulfate reference electrode, was required to increase the rate constant for the VO^{2+} / VO_2^+ reaction. However, the increased rate constant remained until the potential increased to over 0.9 V. The same phenomenon was observed for the V^{2+} /V^{3+} reaction, with application of electrode potentials over 0.1 V increasing the rate constant, but a reduction potential of – 1.3 V was required to reverse this improvement. Similar results were observed at a range of different carbon surfaces in other work by the same authors [124, 125].

It is possible to combine different surface treatment methods, for instance graphite felt was soaked in 98% sulphuric acid for 5 hours before thermal treatment at 450 ^oC for 2 hours. An increase in COOH groups was observed, with kinetic performance improvements determined from a reduction in peak separation during cyclic voltammetry, with only a minor increase in physical surface area, measured by Brunauer–Emmett–Teller theory of gas adsorption (BET) [126].

3.4.2. Surface Area and Roughness Effects

Many of the electrode treatments used to alter surface functional groups also increase the electrochemically active surface area of carbon fibers, for instance nitric acid treatment has been shown to considerably increase the surface area [105]. Graphite felts were treated in an atmosphere of ozone for up to 12 minutes at 25, 160, 180 and 200 °C and compared to thermal treatment in air for 5 h at 500 °C. Felt treated in air had a noticeable increase in surface area measured by BET, from 1.82 m^2 g^{-1} to 3.05 m^2 g^{-1}. Ozone treatment resulted in even more pronounced increase in surface area, up to 10.1 m^2 g^{-1}. The ozone treatments also increased the quantity of oxygen functional groups relative to thermal treatment in air, despite the lower process temperature and the shorter duration. The reduction in charge transfer resistance, R_{ct} correlated with the increased surface area, with one felt treated at 180 ºC in ozone having an $R_{ct} = 0.88$ ohm, while the unmodified graphite felt and the graphite felt thermally treated in air had higher values of $R_{ct} = 11.9$ and $R_{ct} = 3.16$ ohm. This implies that there was also a change in the inherent charge transfer kinetics or an increase in wettability, as the decrease in charge transfer resistance for both the thermal treatment in air and ozone was larger than the increases in surface area as measured by BET, by a factor of around 2 [127].

3.4.3. Electrode Wettability

Oxidising a carbon paper electrode with a 1500 mV pulse lead to an increase in the interfacial surface area, capacitance and more complete wetting in a V^{2+} / V^{3+} electrolyte. The increase in capacitance was proportional to an increase in the rate of the vanadium redox reactions at the electrode. Applying a larger pulse of more than 1500 mV gave a further increase to the capacitance and electrode kinetics, but over time in the V^{2+} / V^{3+} electrolyte the effect faded [90].

Electrochemical activation of a graphite disc electrode was carried out by applying potentials of 1.5, 1.6, 1.7, 1.8 and 1.9 V for 10 minutes in a solution of 0.1 M $VOSO_4$ dissolved in 3 M H_2SO_4. It is not overly clear what the potential is in reference to, whether it is relative to S.H.E, the calomel counter electrode or if it is the cell potential with a platinum counter electrode. A modest increase in the rate constant for the positive VRFB redox reaction was observed, from 1.93×10^{-3} cm s^{-1} to 2.63×10^{-3} cm s^{-1}, as the treatment potential was increased from 1.5 V to 1.9 V. The wettability was observed to improve with increasing treatment potential, possibly explaining the modest increase in rate constant [128].

Carbon paper was etched with chlorosulfonic acid, introducing sulfonic acid groups to the surface. Enhanced wettability was observed from a reduction in water droplet contact angle. Etching assisted by ultra-sonication improved the wettability further. When the ultrasonicated carbon paper was used as a positive VRFB electrode, the charge transfer resistance from EIS meaurements was significantly reduced. The improvement in performance may be due to the increased electrically active surface area from the enhanced wetting [129].

3.4.4. Electrode Conductivity

When a carbon felt electrode was electrochemically treated at 2.5 V for 2 hours in a solution of 0.2 M $VOSO_4$ dissolved in 2 M H_2SO_4, a large increase in oxygen content, from 4.12% to 22.83% was observed. This increase in oxygen led to a large increase in electrical resistance from 0.28 Ω cm^{-2} to 1.3 Ω cm^{-2}. This work compared a number of different graphite-based electrodes with and without chemical and electrochemical activation treatments and found an optimal oxygen content of 5%, with higher oxygen concentrations increasing electronic resistance and charge transfer resistance [130].

3.5. Structural Modifications

Structural modification is a loose term and there will be numerous methods that could be applied to change the surface of carbon based materials. Graphene oxide appears to be a popular material used for surface modifications. Often structural modifications involve a thermal treatment step, which we know from literature can have a significant influence on performance, so it is important to compare modified electrode results to a suitable control.

3.5.1. Inherent Kinetics

Electrodes were prepared from reduced graphite and graphene oxide; however, it is unclear what porosity or geometry these electrodes exhibited or if they required a support. The graphene obtained from thermal reduction of graphene oxide exhibited better kinetic performance than graphene obtained from exfoliation. The improved performance was credited to higher electronic conductivity and more residual oxygen functional groups as active reaction sites [131].

Mesoporous carbon was dispersion coated using a sol-gel process onto PAN-based carbon felt and subsequently annealed at 900 to 1100 °C. The sol-gel coating increased the surface area and the number of oxygen containing surface functional groups. There was a significant increase in peak currents for the positive electrode reaction on the mesoporous carbon felts, relative to a thermally treated carbon felt (420 ^{o}C for 3 h). This increase was attributed to the higher surface area of up to 9.5 times the thermally treated felt. However, the thermally treated felt had a smaller charge transfer resistance as measured by EIS and thus there is likely a difference in inherent kinetics between the mesoporous surface and the thermally treated carbon felt. Additionally, the mesoporous felt may have had lower electronic conductivity, further reducing the performance [132].

3.5.2. Surface Area and Roughness Effects

Graphite felt was modified by pyrolysing sucrose onto the surface, creating an activated charcoal coating. The pyrolysed sucrose increased the surface area to 13.8 m^2 g^{-1} from 6.3 m^2 g^{-1}, as measured by BET. Additionally, the oxygen content was found to have increased slightly. An improvement in kinetics was observed from cyclic voltammetry and EIS measurements, although the charge transfer resistance reduced by only 20 %. Therefore, the increase in physical surface area did not lead to a linear increase in electrically active surface area, which would imply a reduction in wettability, or the modified electrode had slower inherent kinetics towards the vanadium redox reactions [133].

A macroporous graphitic nanoweb of three-dimensionally entangled nanoribbons was synthesized for use as an electrode, in contrast to the traditionally used carbon paper or felt electrodes. The specific surface area was found to be 213 m^2 g^{-1} from BET measurements, which is significantly larger than typical values for carbon felts. Cyclic voltammetry using the macroporous nanoribbons electrodes returned smaller peak separation than a commercial carbon felt sample. No obvious effort was made to quantify the kinetics or assign the improvement to surface area or functional groups, however it seems safe to assume the EASA was larger at the macroporous nanoribbons than the carbon felt [134].

3.5.3. Electrode Wettability

Highly porous carbon felt electrodes were prepared using a method known as Holey-engineering [135]. The highly porous carbon felt was found to have improved wettability and a 20-fold increase in surface area. This felt demonstrated improved performance for both the positive and negative vanadium electrodes, with current densities of up to 300 mA cm^{-2} recorded and good stability demonstrated by completing 3,000 cycles at 150 mA cm^{-2} [136].

Graphite felt electrodes were decorated with carbon dots using a solvothermal method. The modified felts exhibited improved wettability and enhanced catalytic activity, as evidenced by a reduction in the peak separation of recorded cyclic voltammetry. Additionally, an increased peak current was observed, likely due to the enhanced wettability increasing the electroactive surface area [137].

3.5.4. Electrode Conductivity

Graphene oxide nanoplatelets were prepared using a modified version of the Hummer's method. Presumably these nanoplatelets were deposited onto a polished glassy carbon electrode, although this part of the methodology is not explicitly clear. The nanoplatelet material showed a 6-fold increase in surface area, relative to glassy carbon, as measured by BET. Typically an increase in surface area would result in improved electrochemical performance, however the increased area was linked to a large decrease in electronic conductivity, resulting in reduced performance [138].

4. EIS at Carbon Fiber Cylindrical Microelectrodes

4.1. Abstract

The theoretical mass-transport impedance at cylindrical microelectrodes has been known for some time, but an experimental verification is given here for the first time, using carbon fiber electrodes taken from a commercial carbon felt. Nonlinear least-squares fitting of the impedance spectrum of a redox couple at the reversible potential enables accurate evaluation of a composite parameter containing the standard rate constant and mean diffusivity, without measuring the fiber diameter, length or area.

4.2. Introduction

The use of fiber-based materials in electrochemistry has seen a resurgence recently, with the use of carbon felts as electrodes in redox flow batteries and electrospun polymers in emerging energy technologies. It is important to be able to characterize individual fibers and relate this information to the properties of the assembled material. At the time when microelectrodes were being developed, there was an interest in cylindrical microelectrodes [139-144], but they were harder to manipulate and there were indications that convection effects disrupted the desired radial diffusion [145, 146]. There are reports of fits of cyclic voltammetry and chronoamperometry data to numerical simulations involving cylindrical diffusion [140]. The mass transport impedance has an analytical solution, but has apparently not been applied to the case of long cylindrical microelectrodes, for which the radius is less than the diffusion length. We here study the $Fe(CN)_6^{3-}$ / $Fe(CN)_6^{4-}$ redox couple at individual carbon fibers, and show that electrochemical impedance spectroscopy (EIS) enables accurate extraction of the standard rate constant.

The dc diffusion field between two concentric cylinders has a logarithmic dependence on the cylinder radii, Eq. (1), as known for a long time, e.g., from the analogous current distribution problem [147].

$$c(r_\delta) - c(r_0) = -\frac{rJ(r)}{D} \ln \frac{r_\delta}{r_0} \tag{4.1}$$

Here r_δ and r_0 are the radii of the outer and inner cylinders, D is the diffusivity, $J\,(r)$ is the radial flux (mol m^{-2} s^{-1}), and the product $rJ\,(r)$ is independent of r. The case of interest here is a large solution volume $r_\delta \to \infty$. In that case, the logarithmic factor tends to infinity and so the system does not reach a true steady state. However, as in the 1-D semi-infinite case, we proceed to solve the ac problem as though there were a steady state, recognizing that the impedance will go to infinity at low frequencies. Fleischmann et al. [146] derived the impedance for a quasi-reversible redox couple at a cylindrical microelectrode. The solution was given as a complicated expression involving the Kelvin functions Kei and Ker. They stated that the real and imaginary parts increase to infinity because there is no steady state, but their complex-plane plot suggests that the imaginary part tends to a constant value at low frequencies. Later, Jacobsen and West [148] gave the solution for the dimensionless mass transport impedance in terms of Bessel functions as Eq. (2), where K_0 and K_1 are the modified Bessel functions of the second kind of order 0 and 1, and τ_d is a diffusion time constant.

$$z = \frac{\tilde{c}D}{\tilde{J}r_0} = \frac{K_0\left(\sqrt{i\omega\tau_d}\right)}{\sqrt{i\omega\tau_d}K_1\left(\sqrt{i\omega\tau_d}\right)} \tag{4.2}$$

$$\tau_d = \frac{r_0^2}{D} \tag{4.3}$$

They correctly pointed out that the imaginary part tends to a constant value of $-\pi/4$ at zero frequency. (The similar case of insertion and diffusion into a cylindrical electrode was earlier solved in terms of Bessel functions by Barral et al. [149]). The mass transport impedance in usual units is given by $Z_d = \sigma'\sqrt{\tau_d}z$, which replaces $Z_d = \sigma'/\sqrt{i\omega}$ for the more usual 1-D semi-infinite case.

Aside from this substitution, the mass transport impedance is coupled to the reaction kinetics in the usual way. For the standard redox reaction and kinetics, Eqs. (4.4,4.5)

$$R \rightleftharpoons P + e^- \tag{4.4}$$

$$\frac{j}{F} = k_f c_R - k_b c_P \tag{4.5}$$

The derivation of the Randles circuit [150, 151] gives σ' as in Eq. (4.6).

$$\sigma' = \sqrt{2\sigma} = R_{ct}\left(k_f D_R^{-\frac{1}{2}} + k_b D_P^{-\frac{1}{2}}\right) \tag{4.6}$$

In coupling the mass transport, and for the rest of the paper, we make the common assumption that $D_R = D_P = D$, and σ' then reduces to Eq. (4.7), where $k = k_f + k_b$. It is convenient to fit directly to the composite parameter ψ, Eq. (4.8), which is independent of electrode area.

$$\sigma' = R_{ct} k D^{-\frac{1}{2}} \tag{4.7}$$

$$\psi = \frac{\sigma'}{R_{ct}} = \frac{k}{\sqrt{D}} \tag{4.8}$$

If both species are present in equal concentrations c^b and their activity coefficients are equal, then at the reversible potential the standard rate constant $k^0 = k_f = k_b$, and the simple relationships of Eqs. (4.9) – (4.11) apply.

$$\psi = \frac{2k^0}{\sqrt{D}} \tag{4.9}$$

$$R_{ct} = \frac{RT}{F^2 c^b k^0} \tag{4.10}$$

$$\sigma' = \frac{2RT}{F^2 c^b D^{\frac{1}{2}}} \tag{4.11}$$

4.3. Materials and Methods

Single carbon fibers were extracted from a carbon felt sample (GFE1, Ceramaterials, USA) and glued to electrical wire using carbon glue. The wire was housed in a glass capillary tube and the end sealed with epoxy resin, leaving only the carbon fiber exposed to the electrolyte. Data were collected at 23 ± 1°C. SEM images of the felt showed fiber diameters averaging 10 μm with a standard deviation of 1 μm. Detailed EIS data were collected for two fibers, but the results are here reported for a single 3.4 mm long fiber, which had lower EIS noise. The solution was 1 mol dm^{-3} KNO_3 with 10.0 mmol dm^{-3} each of $K_3Fe(CN)_6$ (Vickers Laboratories Ltd) and $K_4Fe(CN)_6$ (BDH AnalaR). The diffusivities in 1 mol dm^{-3} KNO_3 were calculated from the limiting current reached during steady state polarisation curves on a polished gold rotating disk electrode (5 mm diameter, Pine Research Instrumentation), rotated at speeds from 100 to 600 rpm. The Levich equation was applied to relate the limiting current to the diffusivities, which were found to be 8.6×10^{-6} cm^2 s^{-1} for $Fe(CN)_6^{4-}$ and 8.37×10^{-6} cm^2 s^{-1} for $Fe(CN)_6^{3-}$. Here we use the mean value $8.50 \pm 0.05 \times 10^{-6}$ cm^2 s^{-1}, where the quoted 1σ error is somewhat arbitrarily estimated so that $\pm 2\sigma$ spans the two measured diffusivities. This is similar to the literature mean value in 0.5 mol dm^{-3} K_2SO_4 of 8.45×10^{-6} cm^2 s^{-1} [152]. Potentiostatic EIS data were collected with a Gamry 3000 potentiostat, and were fitted to the impedance expression Eq. (4.12) for the Randles circuit for cylindrical diffusion and with a CPE replacing the double-layer capacitance.

$$Z = R_u + \frac{1}{Y_0(i\omega)^{\emptyset} + \frac{1}{R_{ct}\left(1 + \psi\sqrt{\tau_d z}\right)}} \tag{4.12}$$

The complex nonlinear least squares fitting was done using Maple's NLPSolve routine using the nonlinearsimplex option, with a custom calling program that also derives the standard errors in the usual way, i.e., from the values of the derivatives of the impedance with respect to the parameters at the minimum [153]. No weighting was used.

Fitting failed to converge using the Bessel function expression Eq. (4.2), probably because the numerical evaluation of the real and imaginary parts is subject to error. Therefore, the expression was replaced by the approximation

$$z = \ln\left(\frac{1+\sqrt{i\omega\tau_d}}{\sqrt{i\omega\tau_d}}\right) \tag{4.13}$$

or which the real and imaginary parts have analytical expressions known to Maple. It matches the logarithmic dependence on frequency of the real part and constant imaginary part $-\pi/4$ at low frequencies and $(i\omega)^{-1/2}$ dependence at high frequencies [148] and interpolates between them. The relative errors (with respect to Eq. (4.2)) in the real and imaginary parts do not exceed 4%. For the fitted data, the resulting systematic error in the parameters can be estimated by individually varying the parameters to find the minimum in the residual sum of squares. For example, for the 0 V case below, these errors were about 2% for ψ, 9% for τ_d and 1% for R_{ct}. The statistical errors given below used the fitted function, but in the plots comparing the experimental and theoretical values, the full Eq. (4.2) is shown. The data were analyzed without regard to the electrode area, but Figure 4.1 presents data relative to the area, which was estimated from the length and the radius determined from τ_d as described below.

4.4. Results and discussion

Figure 4.1 shows impedance spectra at two selected potentials.

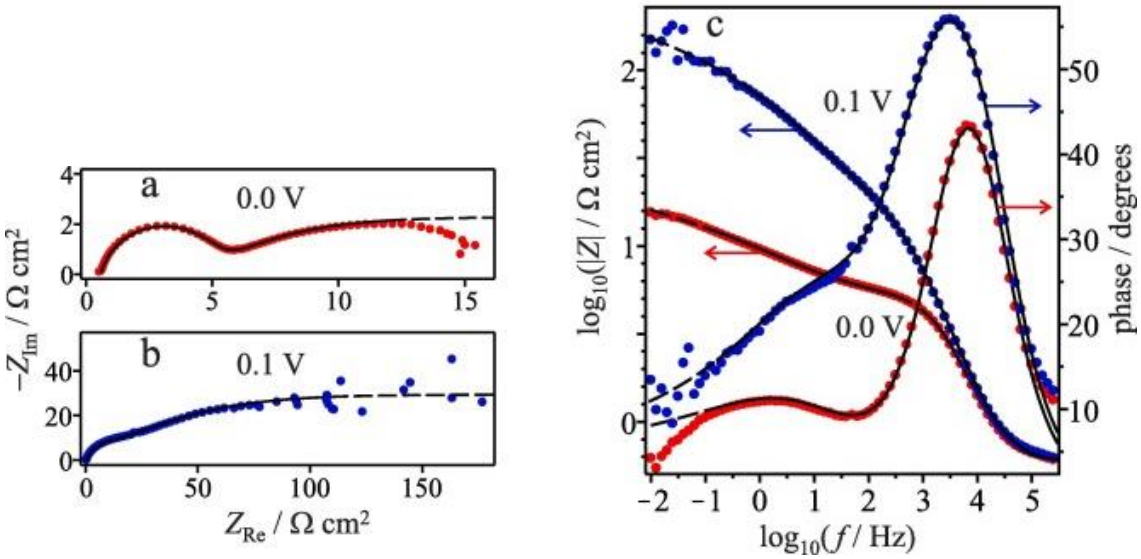

Figure 4.1: Impedance spectra for a carbon fiber. Red points are experimental data at the reversible potential, blue points are at an overpotential of +0.1 V. Black solid lines are fitted curves; dashed lines are extensions into the lower frequency region that was not used in the fit.

As usual, the high-frequency semicircle in the Nyquist plots arises from the charge-transfer resistance and double-layer capacitance. The lower frequency feature is the mass transport impedance, which rises to a plateau as predicted. In the case of the reversible potential, at the lowest measured frequencies the imaginary part of the impedance decreased again, possibly due to convection. At higher overpotentials, the low-frequency region became noisy and this decrease was not seen. The value of d determines the frequency at which the rise to the plateau occurs and the value of determines the height of the plateau.

At the reversible potential, the fitted parameters were $\psi = 5.28 \pm 0.07\ s^{-1/2}$, $\tau_d = 13.7 \pm 0.4\ ms$, $R_{ct} = 6470 \pm 30\ \Omega$, $Y_0 = 56 \pm 2\ nF\ s^{1-\phi}$, $\phi = 0.843 \pm 0.003$ and $R_u = 790 \pm 9\ \Omega$. Using Eq. (3), the radius of the fiber was estimated from the values of τ_d and the mean diffusivity (Section 2) to be 3.42 ± 0.05 μm. The standard rate constant calculated from Eq. (4.9) is k^0 = 7.70 ± 0.11 × 10^{-3} cm s^{-1}. The value of R_{ct} at the reversible potential can then be estimated from Eq. (4.10) to be 3.4 Ω cm^2. The errors in k^0 and r_0 are dominated by the fitting errors in ψ and τ_d respectively, and not the error in the mean diffusivity. The quoted errors are fitting errors only, and a more extensive study of many fibers will be required to clarify systematic errors. As in impedance methods for other geometries, no measurement of the surface area of the fiber is required. If the measured area is available, then a consistency check may be carried out by comparing R_{ct} above with the directly fitted R_{ct} in Ohms multiplied by the area. In the present case, the area was estimated from the radius found above and the known length, which gives R_{ct} = 4.7 Ω cm^2. Instead of starting with a known mean diffusivity, an alternative approach to this analysis would be to use the measured radius to estimate the diffusivity, and in turn the rate constant. Literature standard rate constants for the $\mathrm{Fe(CN)}_6^{3-/4-}$ system vary widely depending on the solution, the type of carbon surface and the surface pretreatment, and span the range 0.005 - 0.5 cm s^{-1} [154]. For the fastest rate constants (> 0.1 cm s^{-1}) an activation procedure is generally required [155]. Lower values similar to that obtained here are typically obtained for unactivated surfaces such as regularly polished glassy carbon 0.005 cm s^{-1} [154, 156] or carbon paste 0.001 - 0.007 cm s^{-1} [157]. The analysis here assumes smooth surfaces, or at least a roughness scale small compared to the radius, in which case the true rate constant is the quoted value divided by the roughness factor, and the radius determined will be an average value. The effective double-layer capacitance calculated from the Brug formula (Eq. (8.12), Ref. [150]) is small, 12 μF cm s^{-2}, similar to literature values [140, 158] for untreated fibers. Much higher capacitances are found for activated and severely roughened surfaces, for which the effective radius may underestimate the true radius [140].

A distribution of rate constants is expected for the different fibers in a carbon felt [159-161], and the present method can be useful in determining the variation in rate constants. For the type of fibers used here, numerical modeling of voltammograms gave standard rate constants for 13 fibers with a mean of 7.3×10^{-3} cm s^{-1} and a standard deviation of 4.7×10^{-3} cm s^{-1}. The individual determinations by the impedance method were more accurate. Measurements were also carried out away from the reversible potential. These could also be fitted to the same impedance expression, but the high-frequency semicircle and the mass-transport feature were less well resolved, which led to higher errors in τ_d and the other parameters. Allowing for the larger errors, the parameters $\tau_d, Y_0, \emptyset$ and R_s did not depend much on potential as expected. The parameters R_{ct} and ψ are expected to be potential dependent, and although they were higher for higher overpotentials, the potential dependence was weak. Simulations showed that the potential dependence did not fit the expectations of a simple one-electron reaction with Tafel-like potential dependence of rate constants. Non-ideal behavior for the $\mathrm{Fe(CN)}_6^{3-/4-}$ system at C electrodes has been seen before and attributed to adsorption [162] or other interactions with the surface [155]. In the specific case of KNO_3 solutions, Fletcher and Varley saw Tafel slopes as low as 62 mV/decade and invoked a chemical step [163]. Another possibility is electrode aging due to deposition of a film, which limits electron transfer and reduces the potential dependence, though the constancy of the double-layer parameters argues against this mechanism. We also note that measurements away from the reversible potential can be affected by ohmic drop along the fiber itself, which has a resistance of the order of 400 Ω mm^{-1}. Another possibility is that convection, which dogged early experiments with microcylindrical electrodes, is operating at higher overpotentials, where a dc concentration gradient is present in solution. Unlike other methods, EIS can fully determine the standard rate constant without significant excursions away from the reversible potential. There is therefore no requirement for a dc concentration gradient, only an ac one, for which modern instruments excel at noise rejection. The resolution of this issue is outside the scope of the present work, where good results were always achieved for pristine fibers at the reversible potential.

4.5. Conclusions

The Bessel function form for the impedance of the cylindrical diffusion problem was experimentally verified for the first time by nonlinear least-squares fitting to impedance data measured for the $\mathrm{Fe(CN)}_6^{3-/4-}$ redox system at carbon fiber electrodes. Accurate results were facilitated by fitting directly to an approximation of the theoretical expression for the impedance. By making the combined parameter $k/\sqrt{D}$ one of the fit parameters, the need for error propagation was minimized and the rate constant could be accurately found. Provided the mean diffusivity is known, this method does not require measurements of the electrode length, radius or area.

4.6. Acknowledgements

Financial support is acknowledged from the Natural Sciences and Engineering Council of Canada (Discovery Grant RGPIN-2017-04045) and the University of Canterbury (PhD scholarship for L. Landon-Lane).

5. Single Fibre Electrode Measurements - a Versatile Strategy for Assessing the Non-Uniform Kinetics at Carbon Felt Electrodes.

Abstract

Redox flow batteries (RFBs) are a promising technology for the storage of intermittent renewable energy. Graphite and carbon felts electrodes are commonly used in RFBs as they typically exhibit good conductivity, high liquid permeability, high surface area and are relatively inexpensive. The electrochemical performance of carbon felts is commonly tested by calculating the energy efficiency for charge-discharge cycles of electrochemical cells containing the felt electrodes. This method whilst useful does not provide a direct measure of the kinetics of the redox reactions at the electrode surface. Furthermore, the standard electrochemical methods (e.g. cyclic voltammetry) commonly used to determine the electron transfer kinetics cannot be easily applied to carbon felt electrodes due to the complex mass transport behaviour within the porous felts. In this work we have shown that kinetics at carbon felts can be determined by performing cyclic voltammetry on single carbon fibre electrodes extracted from the carbon felt. This approach avoids the complex mass transport behaviour while also providing a method to determine the distribution of rate constants within a carbon felt electrode. By combining this measured rate constant distribution with the void size distribution of the carbon felt, the cyclic voltammetry of carbon felt electrodes can be successfully simulated over a wide range of sweep rates. Importantly, this approach highlights the necessity of accounting for the rate constant distribution within carbon felt electrodes.

5.1. Introduction

Redox flow batteries are a good option for large-scale storage of renewable energy and are being deployed at an increasing scale [32, 35]. One of the major advantages of RFBs over other battery technologies is that the electrodes are inert, so have little to no degradation over time or number of charge-discharge cycles under normal operating conditions. Traditionally, RFBs use carbon or graphite felt electrodes as they are stable, conductive and relatively low cost [46, 164, 165]. However the electrochemical performance of these electrodes for the desired reactions can be poor, with current densities typically below 200 mA cm^{-2}, compared to fuel cells which can operate at 1500 mA cm^{-2} or more [166]. Increased current density would enable cost reductions, as the cell stack in RFBs contributes significantly to the overall capital cost of the battery, where the quantity of expensive ion exchange membranes required to achieve a target power output is proportional to the power density of the cell [80]. Therefore, improving battery performance by increasing the current density will positively influence the economic viability of these batteries.

RFB electrode performance depends on many factors: wettability, electrical conductivity, surface area, hydrodynamics, and inherent kinetics of the electrode reactions. It is often hard to decouple these factors in order to understand their role in overall RFBs performance. For example, while the thermal pre-treatment of carbon felts has been suggested to improve the reaction kinetics [167], the improved performance of the electrodes may also be due to an increase in the wettability of the carbon felt or to an increase in surface roughness [90].

For some electrodes, it is relatively easy to determine the kinetics of redox reactions using cyclic voltammetry. For instance, the standard heterogeneous rate constant for a redox reaction at a semi-infinite planar electrode assuming 1D diffusion can be determined from the peak potential separation [168]. This approach has been used to qualitatively compare the reaction kinetics on different carbon felt electrodes [169-171]. Whilst the rate constant will influence the peak potential separation, determining the rate constant from these measurements is very challenging due to the complex mass transport behaviour within these electrodes. Electrode porosity and surface roughness lead to complex diffusion domains which alter measured cyclic

voltammograms [172-176]. These effects may explain the wide range (four orders of magnitude) in the reported standard heterogeneous rate constants obtained at carbon felt electrodes for the redox reactions that occur in vanadium redox flow batteries [177]. Recently, others have overcome these challenges by modelling carbon felt as a system of micro-cylinder electrodes to allow the rate constant to be determined using cyclic voltammetry at carbon felt electrodes [178]. While this approach is very promising, as the rate constant and felt void size distribution influence the voltammograms in a similar way, a manual fitting procedure was required in that work [178] and it was assumed that the rate constant was a fixed value throughout the felt.

In this work, to quantify the influence of non-uniform kinetics at carbon felt electrodes, the electron transfer kinetics of the ferri/ferrocyanide redox couple are measured directly at 12 single carbon fibre electrodes extracted from a carbon felt sample. Ferri/ferrocyanide was used as a model redox couple for this work as has a standard redox potential which is far from the hydrogen and oxygen evolution potentials, and thus these reactions do not interfere with the data analysis. The advantage with using single fibre electrodes extracted from felt, is that the standard heterogeneous rate constant is determined at an electrode with the identical surface chemistry as found in the felt, without the complex mass transport behaviour. Importantly, for the first time, the distribution of rate constants for a felt sample is determined and then used along with the measured void size distribution to successfully model cyclic voltammograms at the carbon felt electrode.

5.2. Experimental Methods

Electrochemical experiments were carried out using solutions of $K_4Fe(CN)_6$ (BDH AnalaR) and $K_3Fe(CN)_6$ (Vickers Laboratories Ltd) dissolved in 1 M KNO_3. For single fibre electrode measurements, concentrations of 10 mM $K_4Fe(CN)_6$ and 10 mM $K_3Fe(CN)_6$ were used. This concentration was chosen to increase the faradaic current measured at these small electrodes. When using carbon felt electrodes, as the total surface area was much larger, 0.1 mM $K_4Fe(CN)_6$ and 0.1 mM $K_3Fe(CN)_6$ were used to ensure that the total current and thus uncompensated ohmic resistance was minimised.

A standard three electrode configuration was employed for all electrochemical measurements, using a Gamry 3000 potentiostat. Dissolved oxygen was purged prior to each experiment by bubbling argon through the electrolyte, and an inert atmosphere was maintained above the electrolyte during all measurements. The temperature of the cell was maintained at 23 ± 1^{o}C. Single carbon fibre electrodes were fabricated using a procedure similar to those reported in literature [179, 180]. Briefly, single carbon fibres from carbon felt (GFE-1, Ceramaterials, USA) were attached to copper wire using electrically conductive carbon glue. This contact was then sealed in epoxy resin to ensure that only the carbon fibre was exposed to the electrolyte. Carbon fibre electrodes were 3-5 mm in length. For the carbon felt electrodes, a section of the same felt, measuring 1 cm by 1 cm with a thickness of 3.5 mm, was held in a 3-D printed holder with only the 1 cm^2 front face open to the electrolyte. Electrical contact to the felt was made using a glassy carbon plate attached to a conductive wire insulated from the electrolyte using epoxy resin.

The resistance between the working and reference electrodes was quantified using electrochemical impedance spectroscopy (EIS), measured at the open circuit potential with a 10 mV rms sinusoidal potential excitation at frequencies between 1 MHz and 1 Hz. 80% of the resistance measured by EIS was corrected for using positive feedback compensation during cyclic voltammetry at the carbon felt electrodes, with the remaining 20% used to correct the data after the measurements were complete.

The diffusion coefficient for $Fe(CN)_6^{3-}$ and $Fe(CN)_6^{4-}$ was calculated from the limiting currents obtained from steady state voltammograms at a glassy carbon electrode, rotated at rates from 100 to 600 rpm. The Levich equation was applied to relate the limiting current to the diffusion coefficient and the average value ($8.35 \times 10^{-6} \pm 0.05$ $cm^2\ s^{-1}$) was used for both redox species for ease of modelling. This value is in agreement with those reported in literature [152].

Measured currents are reported as current densities to allow for easy comparison against other works. For single carbon fibre electrodes, the area was calculated by assuming that the electrode was a perfect cylinder of 10 μm diameter (based on SEM analysis), with the length measured using an optical microscope. For the felt electrodes, the area used to determine the current density was the cross sectional area of the front face (1.00 ± 0.02 cm^2). Based on the micro-CT and SEM imaging, the total surface area of the fibres within a 1 x 1 cm felt samples is estimated to be 86.2 cm^2. When simulating the cyclic voltammetry at felt electrodes, the total surface area (A_{tot}= 86.2 cm^2) is used, with the results reported as current densities based on the projected surface area (1 cm^2).

The morphology of the carbon felt sample was investigated using a Bruker SkyScan1272 X-ray micro-CT scanning unit. The distance from the camera and object to the source were 274.5 mm and 18.7 mm respectively, with a source voltage and current of 42 kV and 143 μA. Images were taken in slices with a resolution of 0.50 μm per pixel. From the 2D image slices, the total void volume and void size distribution of the felt was calculated using imageJ image processing software, by identifying the area of the slice taken up by fibres.

5.3. Simulations

Numerical models were used to simulate the cyclic voltammetry at single carbon fibre and carbon felt electrodes. For the single carbon fibre electrodes, a 1D partial differential equation model was developed in cylindrical coordinates, with the surface of the fibre assumed to be homogenous, so that a single standard heterogeneous rate constant (k^0) could be used.

The partial derivatives were solved via a system of ODEs using the method of lines and the ode15s solver in Matlab, with the electron transfer rate following Butler-Volmer kinetics.

The change in concentration of the oxidised and reduced species with respect to time is governed by the cylindrical-PDE:

$$\frac{\partial C_I}{\partial t} = D\left[\frac{\partial^2 C_I}{\partial r^2} + \frac{1}{r}\frac{\partial C_I}{\partial r}\right] \tag{5.1}$$

where I can be either the oxidised species O or the reduced species R, r is the radial position relative to the centre of the carbon fibre.

To solve the system, two boundary conditions were defined at the bulk and at the surface. At a large and arbitrary distance from the electrode (r^*) the bulk concentration was assumed to be constant and equal to the initial solution concentration, and thus the bulk boundary condition was defined as:

$$r = r^*: \quad \left.\frac{\partial C_I}{\partial r}\right|_{r=r^*} = 0 \tag{5.2}$$

The surface boundary condition was defined by equating the change in concentration at the surface to the reaction rate at the surface:

$$r = r_e: \left.\frac{\partial C_R}{\partial r}\right|_{r=r_e} = \frac{k^0\left(C_{O,e}\exp\left(-\frac{\alpha nF\eta}{RT}\right) - C_{R,e}\exp\left(\frac{(1-\alpha)nF\eta}{RT}\right)\right)}{D} \tag{5.3}$$

where r_e is the radius of the electrode, $C_{O,e}$ is the concentration of the oxidised species at the electrode surface, $C_{R,e}$ is the concentration of the reduced species at the electrode surface., k^0 is the rate constant, α is the charge transfer coefficient, n is the number of electrons exchanged (equal to one for this reaction), F is the Faraday constant, R is the universal gas constant, T is the absolute temperature, η is the activation overpotential and D is the average diffusion coefficient of the redox species.

This boundary condition was also applied to the flux of the oxidised species to the surface, where $\frac{\partial C_R}{\partial r}\Big|_{r=r_e}$ is replaced by $-\frac{\partial C_O}{\partial r}\Big|_{r=r_e}$ in Eq. (5.3).

In this work only one parameter, k^0 was altered in order to obtain an accurate fit for the single carbon fibre electrodes. The electrode length was measured and the fibre diameter was assumed to be equal to the average from SEM imaging. The diffusion coefficients were calculated from LSV measurements and the temperature recorded during the experiment, thus the only two variables that were unknown were α and k^0. With this redox couple it can be seen that the peak currents for the forward and reverse sweeps are very similar, thus α is likely to be close to 0.5. For ease of fitting α was fixed at 0.5 and only k0 was manipulated, which is similar to the approach used by McCreery, where α was also assumed to be 0.5 [89].

In this work the fitting was carried out using an automated and simple bisection root finding method in Matlab. The initial upper and lower k^0 values for the solver were set to 0.1 cm s^{-1} and 0.0001 cm s^{-1} respectively, with the difference between the experimental and the simulated peak potential separations minimised to within a tolerance of 0.5 mV. Obtaining an accurate fit by minimizing the difference in peak separation is the logical choice in this work due to the correlations previously reported by Aoki and Kaneko [142] and Neudeck and Dittrich [181].

The uncertainties were estimated by finding the k^0 values at which the simulated peak separation differed from the experimental peak separation by more than 2 mV, providing upper and lower limits for the rate constant (Table 5.1).

Table 5.1: Fitted rate constants from simulated voltammograms recorded at 200 mV s^{-1} at single carbon fibre electrodes in 10 mM ferricyanide and 10 mM ferrocyanide.

Fibre	**k^0**
#	(cm s^{-1})
1	0.0098 ± 0.0003
2	0.0160 ± 0.0006
3	0.0087 ± 0.0002
4	0.0100 ± 0.0003
5	0.0097 ± 0.0002
6	0.00160 ± 0.00003
7	0.0064 ± 0.0002
8	0.0123 ± 0.0001
9	0.0100 ± 0.0003
10	0.0027 ± 0.0002
11	0.00096 ± 0.00003
12	0.00140 ± 0.00002
Average	0.0075 ± 0.0030

To simulate the cyclic voltammetry of the carbon felt electrodes, the approach of treating the carbon felt electrode as an array of micro-cylinders was adopted [178]. This model treats the carbon felt as an array of micro-cylinders with a no-flux boundary condition imposed at a set distance from the fibre surface, with the distance chosen to reflect the inter-fibre spacing within the felt. Here each carbon fibre within the felt is modelled in the same way as the single fibres in a bulk solution, but with a no-flux boundary condition imposed at a set distance from the fibre surface instead of a constant concentration boundary condition. In practice the Neumann-Boundary equations are the same, but as the radii of the void size distribution measured by x-ray computed tomography are much smaller than the arbitrarily large radius imposed for the single fibre simulations. The concentration of redox species at the boundary changes during the cyclic voltammetry simulation.

In our work the cyclic voltammograms were simulated at 10 discrete void sizes, with the 12 discrete rate constants found from experimental results on single fibres. In total 120 different cyclic voltammograms were computed at each sweep rate, each with a unique combination of void size and rate constant. The voltammetry of the felt was taken as the sum of these voltammograms, where the current was weighted by the fraction of the felt represented by each void size. The void size distribution was calculated from micro-CT imaging measurements of the felt (see section 5.2).

5.4. Results and Discussion

The cyclic voltammetry of ferricyanide / ferrocyanide at the carbon felt electrode shows a pair of broad redox peaks centred around 0.27 V vs Ag|AgCl (Figure 5.1a). At 100 mV s^{-1} the potential peak separation (ΔE_p) for this redox couple is 77 mV, compared to the reversible limit of 59 mV for a planar electrode with semi-infinite diffusion. The relatively small ΔE_p value of 77 mV could lead to the assumption that the redox reaction is relatively fast [172, 182]. However at slower scan rates, ΔE_p decreases to values significantly smaller than 59 mV (Figure 5.1b) and it is clear that the complex mass transport within the porous network in the carbon felt must be understood before attempting to extract information about the kinetics of the redox couple.

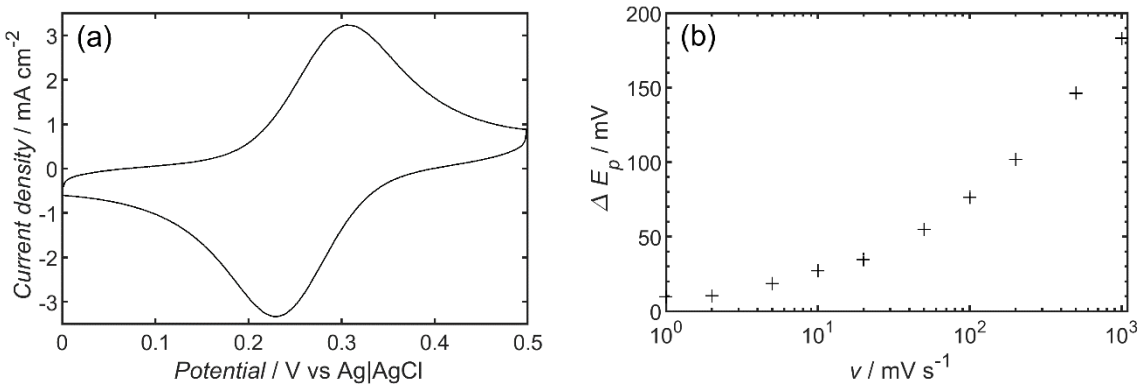

Figure 5.1: a) Cyclic voltammetry of a carbon felt electrode in 0.1 mM $K_4Fe(CN)_6$ and 0.1 mM $K_3Fe(CN)_6$ dissolved in 1 M KNO_3, at a sweep rate of 100 mV s^{-1}. The potential was compensated for ohmic resistance as outlined in the Experimental section. b) Peak separation dependence on sweep rate for porous carbon felt electrode in 0.1 mM $K_4Fe(CN)_6$ and 0.1 mM $K_3Fe(CN)_6$ dissolved in 1 M KNO_3.

The cyclic voltammograms obtained here are similar to those reported by others using carbon felt electrodes under similar conditions [178, 183, 184], and are a result of the contribution of thin-layer like behaviour within the voids of the carbon felt. This behaviour arises when the concentration of one of the redox species is completely depleted within the void volume surrounding each of the fibres in the felt electrode, resulting in ΔE_p values approaching the theoretical value of 0 mV when the scan rate is very slow.

For some porous electrodes, it is possible to find two distinct pairs of peaks from a redox couple with only a single electron transfer process due to the differing transport behaviour within the porous electrode and between the outer electrode surface and the bulk electrolyte [175]. However, as the felt electrode is thick in this case (3.5 mm), the voltammetric response of the felt electrode is dominated by the redox reaction within the felt, with diffusion between the outer surface of the felt and the bulk electrolyte expected to have only a minor contribution, as seen later in this work.

The complex mass transport behaviour within felt electrodes can be avoided by performing cyclic voltammetry at a number of single carbon fibres extracted from the felt. Others have shown that kinetics of redox reactions can be measured and the cyclic voltammetry simulated at micro cylindrical electrodes [142, 181, 185-187]. Aoki *et al.* [142] originally demonstrated that the peak separation from cyclic voltammetry can be related to the rate constant at a cylindrical electrode, however they determined that the relationship between peak separation and experimental conditions for quasi-reversible cases was too complex to be expressed with simple equations. Neudeck *et al.* [181] showed that using non-linear regression approximate values for the rate constant and diffusion coefficient can be calculated from experimental cyclic voltammograms at cylindrical electrodes.

In the present work, the cyclic voltammograms recorded at these single carbon fibre electrodes can then be modelled assuming that the mass transport is controlled by semi-infinite cylindrical diffusion in 1D, allowing electron transfer rate constants to be obtained for each fibre. Figure 5.2 demonstrates that a good fit can be obtained between experimental and simulated voltammograms under these conditions.

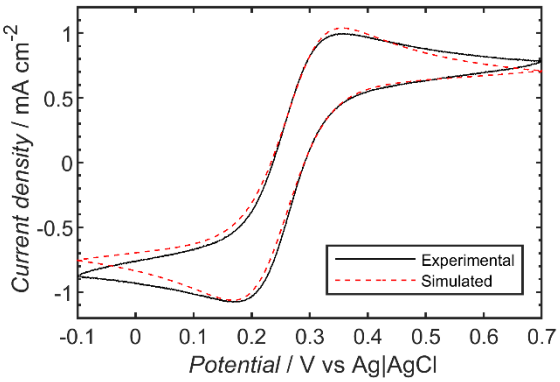

Figure 5.2: Comparison of a typical experimental cyclic voltammogram obtained at a single carbon fibre electrode with a simulated cyclic voltammogram calculated to achieve the best fit. Cyclic voltammetry recorded at 200 mVs^{-1} in a solution of 10 mM ferricyanide and 10 mM ferrocyanide.

For the example in Figure 5.2, the rate constant determined for the single carbon fibre (k^0 = 0.0111 cm s^{-1}) compares well with the rate constant measured at a polished GC electrode (k^0 = 0.0096 cm s^{-1}) in the same solution, and is similar to that measured on other carbon electrodes [154] and identical fibres measured by EIS [188]. This value is also very similar to that reported by Neudeck and Dittrich [181] at carbon micro-cylindrical electrodes (k^0 = 0.00998 cm s^{-1}).

Importantly, by repeating these measurements on 12 single fibre electrodes, multiple rate constants were found (average k^0 = 0.0075 ± 0.0030 cm s^{-1}) which is likely due to the heterogeneous nature of carbon felt [159, 160] (Table 5.1).

In order to use these measured rate constants to simulate cyclic voltammetry at carbon felt electrodes, the void size distribution was determined by taking 3,100 2D slices every 0.5 µm from micro-CT imaging of the carbon felt (Figure 5.3a). The predominant direction of fibers was normal to the slice direction and for each slice a void size distribution was calculated by finding the average distance between each fibre within each slice using image analysis (ImageJ). These average distances were converted to equivalent void diameters and then overall felt void size distribution was then calculated as an average of the distributions from each slice. The void size distribution was discretised by finding the fraction of voids within each 10 µm diameter increment (Figure 5.3b). This experimentally determined void size distribution is similar to those reported by others who also used micro-CT imaging on carbon felt electrodes, although the felt type and analysis method differed [178, 189].

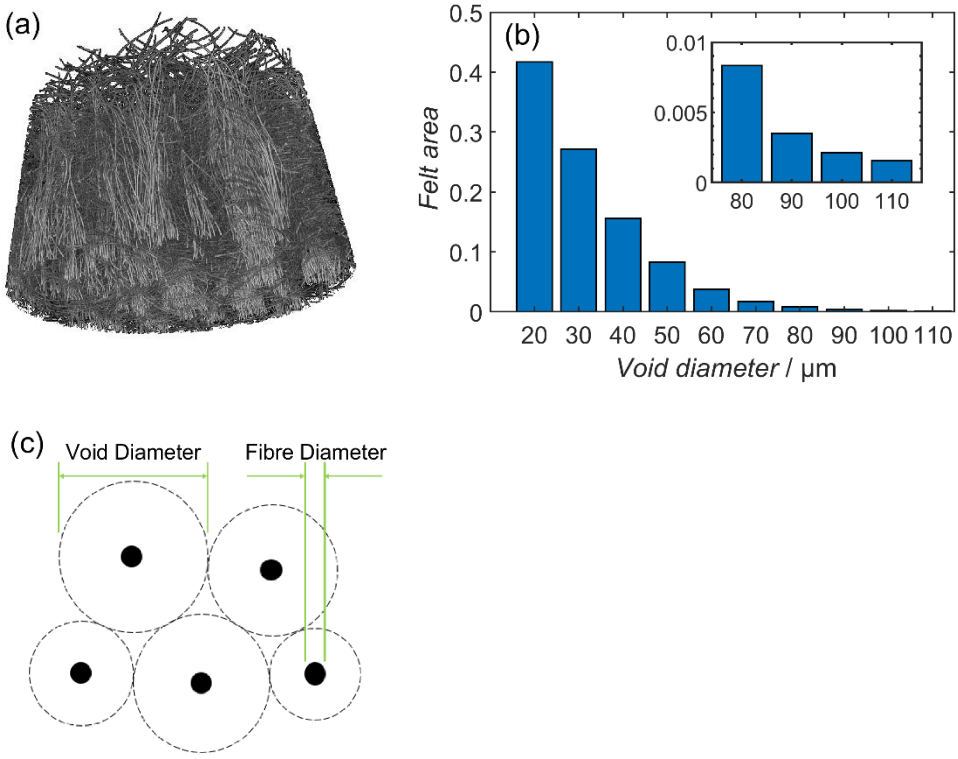

Figure 5.3: a) CT image of carbon felt; b) void diameter distribution: felt area is defined as the fractional area of fibres within the felt within a given void diameter range; c) representation of how the void diameters were calculated from the micro-CT slices

Using kinetic parameters measured at single carbon fibre electrodes and the void size distribution measured by CT imaging, the cyclic voltammetry of carbon felt electrodes was simulated using the numerical model described above (Section 3) and compared to experimental measurements over a range of sweep rates (Figure 5.4). It is important to note that simulated cyclic voltammograms describe the experimental data very well without requiring the use of any unconstrained fitting parameters (all inputs for the model were determined from CT and SEM imaging and the single fibre electrode measurements).

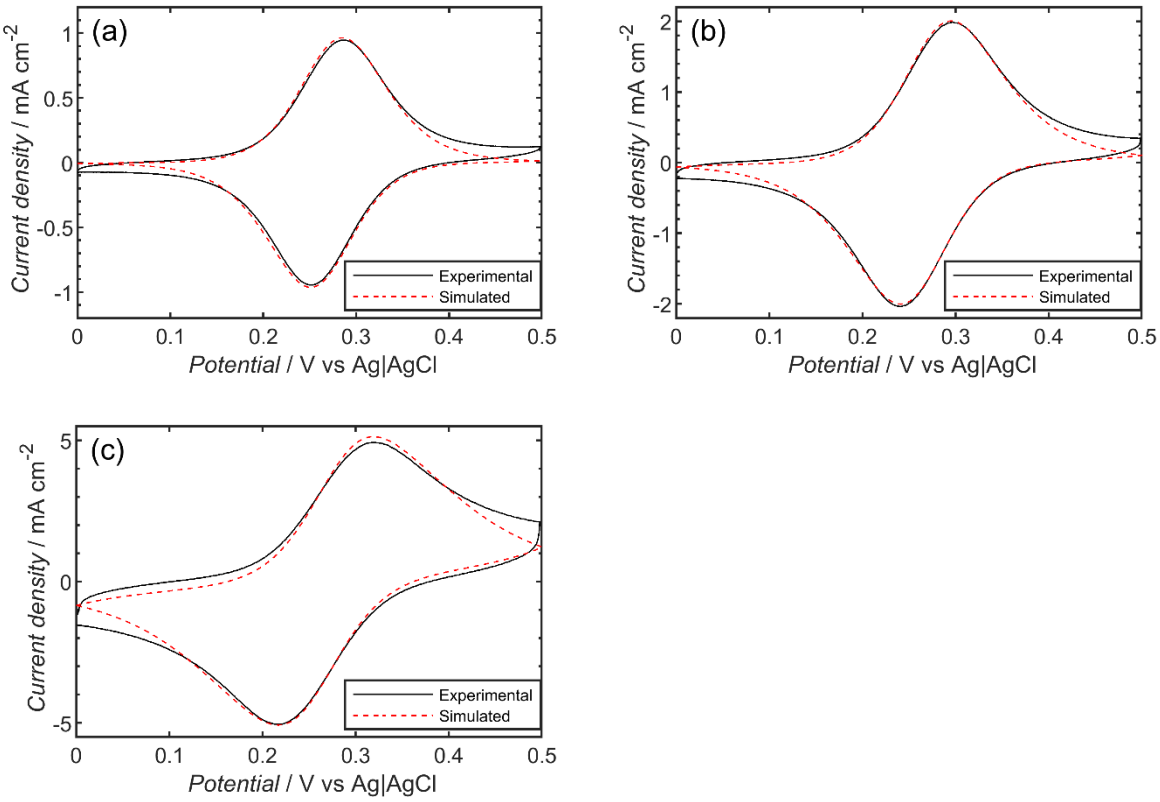

Figure 5.4: Simulated cyclic voltammetry compared to experimental results in a solution of 0.1 mM ferricyanide and 0.1 mM ferrocyanide, at sweep rates of, a) 20 mV s^{-1} b) 50 mV s^{-1} c) 200 mV s^{-1}. The simulated cyclic voltammograms use the calculated void distribution (Figure 3b) and the measured rate constant distribution (Table 5.1).

Discrepancies between the simulated and experimental cyclic voltammograms can be seen in the non-peak regions in Figure 5.4c, even after both the void size distribution and rate constant distribution have been considered. This is likely due to the electrode capacitance, which is not included in the model. The fraction of capacitive current relative to the faradaic current from the redox reaction increases as the sweep rate increases. Because of this, there is poorer agreement between the simulated and measured voltammograms in the non-faradaic regions as the sweep rate increases. The presence of capacitance has also been shown to alter the peak separation, voltammogram shape and peak current at planar electrodes, particularly at faster sweep rates and this likely contributes to the discrepancies observed in (Figure 5.4c) [190].

To illustrate the combined influence of the void size and rate constant distributions, an experimental cyclic voltammogram was compared to simulations based on four different combinations of parameters. These were the average void diameter size (40.8 μm) and average rate constant (0.0075 cm s^{-1}) (Figure 5.5a); the measured void size distribution and the average rate constant (Figure 5.5b); the average void size and the rate constant distribution (Figure 5.5c); and the measured void size and rate constant distribution (Figure 5.5d).

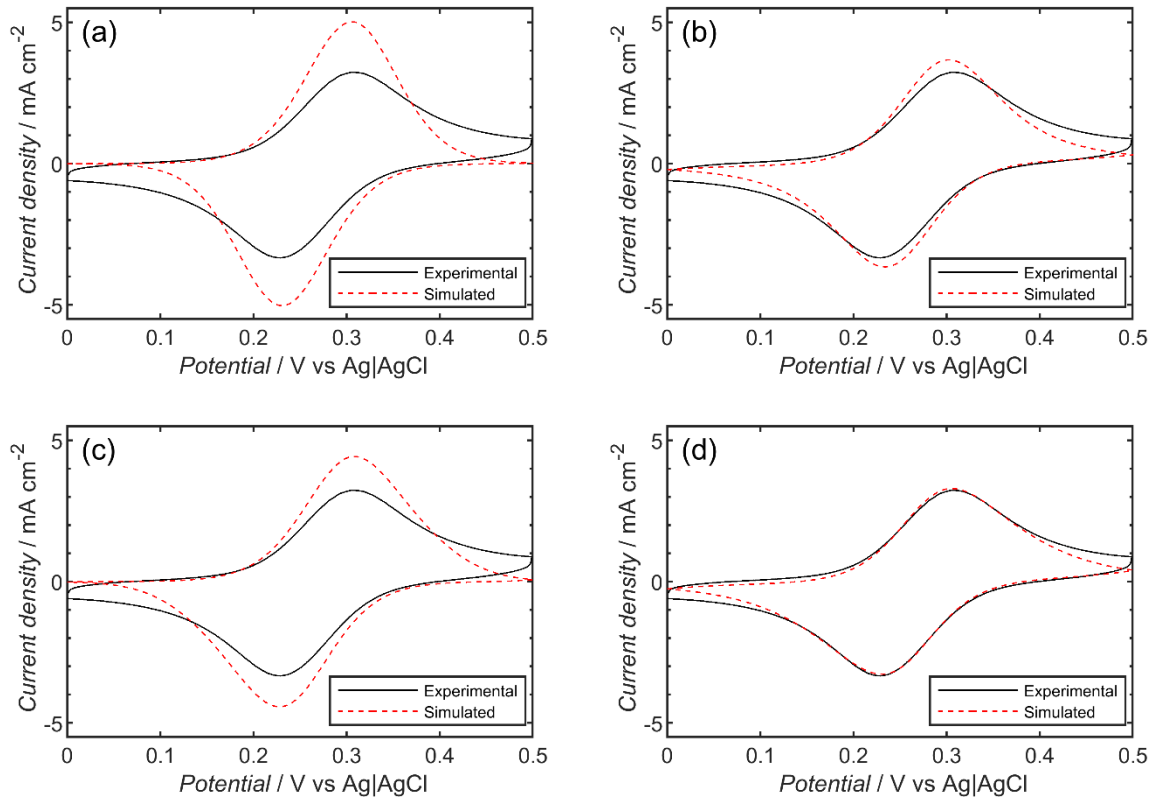

Figure 5.5: Comparison of experimental and simulated cyclic voltammograms, calculated using different combinations of parameters. The experimental cyclic voltammograms were obtained at a carbon felt electrode in a solution of 0.1 mM ferricyanide and 0.1 mM ferrocyanide, at a sweep rate of 100 mVs^{-1}, compensated for ohmic resistance as outlined in Experimental section. a) Modelled using the average void diameter and average rate constant (40.8 μm and 0.0075 cm s^{-1}). b) Modelled using the calculated void distribution (Figure 5.3b) and the average rate constant. c) Modelled using the average void diameter and the measured rate constant distribution. d) Modelled using the calculated void distribution and the measured rate constant distribution.

The simulation results clearly show that the void size distribution has a significant effect on the cyclic voltammetry of the porous carbon felt electrode, (compare Figure 5.5a to Figure 5.5b and Figure 5.5c to Figure 5.5d). This is because the carbon fibres in the felt which are spaced furthest apart behave like single carbon fibre electrodes with semi-infinite cylindrical diffusion, and thus these fibres give a relatively large ΔE_p (Figure 6a, red lines). Conversely, the fibres which are spaced closer together, behave more like thin-layer electrodes, with a smaller ΔE_p (Figure 5.6a, black lines). When these effects are combined with the measured void size distribution, the peaks on the simulated cyclic voltammogram broaden, and the peak separation is dominated by the fibres located within voids of diameter around 20 to 40 µm (Figure 5.6b, black lines).

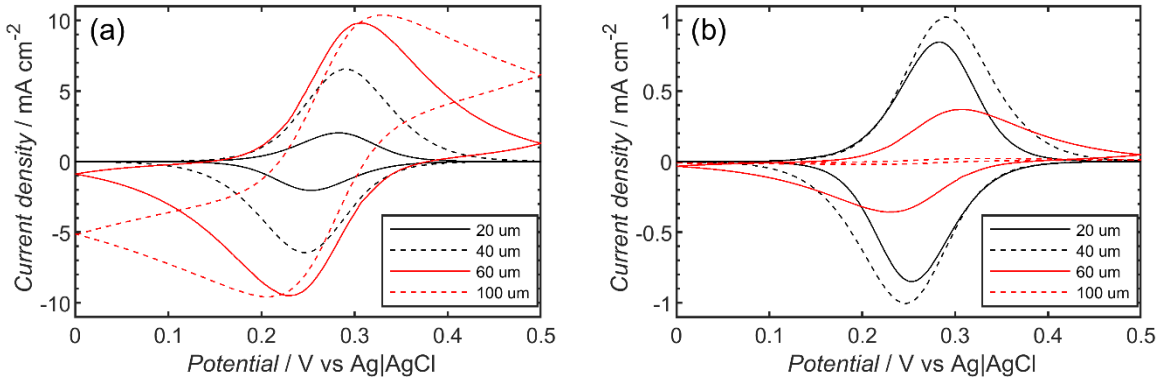

Figure 5.6: Simulated cyclic voltammograms at felt electrodes, using the average rate constant (0.0075 cm s^{-1}) with different void diameters in a solution of 0.1 mM ferricyanide and 0.1 mM ferrocyanide, at a sweep rate of 100 mV s^{-1}. a) Cyclic voltammograms for felts with different void sizes but equal electroactive surface areas. b) Cyclic voltammograms for felts with different void sizes weighted by the fractional surface area calculated from the void size distribution.

To investigate the importance of the measured rate constant distribution, an average rate constant which provides the best fit between the model and measured voltammograms at carbon felt electrodes was determined as a function of sweep rate (Table 5.2).

Table 5.2: Rate constants found by fitting the carbon felt electrode model to measured voltammograms, assuming a single rate constant and the previously shown void size distribution.

Sweep Rate	**Fitted Rate Constant**
(mV s^{-1})	(cm s^{-1})
20	0.0045 ± 0.0005
50	0.0057 ± 0.0005
100	0.0060 ± 0.0005
200	0.0063 ± 0.0004
500	0.0068 ± 0.0003
1000	0.0071 ± 0.0002

The values in Table 5.2 were obtained by fitting the peak potential separation from a felt electrode, with only one rate constant. The fitting method was the same as that used for the single fibres, with the fitting procedure (bisection method) minimizing the difference between the experimental and simulated peak separation by varying k^0. The fits show that the calculated average rate constant increases as a function of sweep rate. However, as the rate constant should be independent of sweep rate, we conclude that rather than an average rate constant, a rate constant distribution is required to account for behaviour over a wide range of sweep rates.

The largest influence of the rate constant distribution on the cyclic voltammetry occurs at high sweep rates where the void size distribution becomes less important. This can be seen by simulating cyclic voltammetry at 1000 mV s^{-1} at single fibre electrodes contained within cylindrical voids.

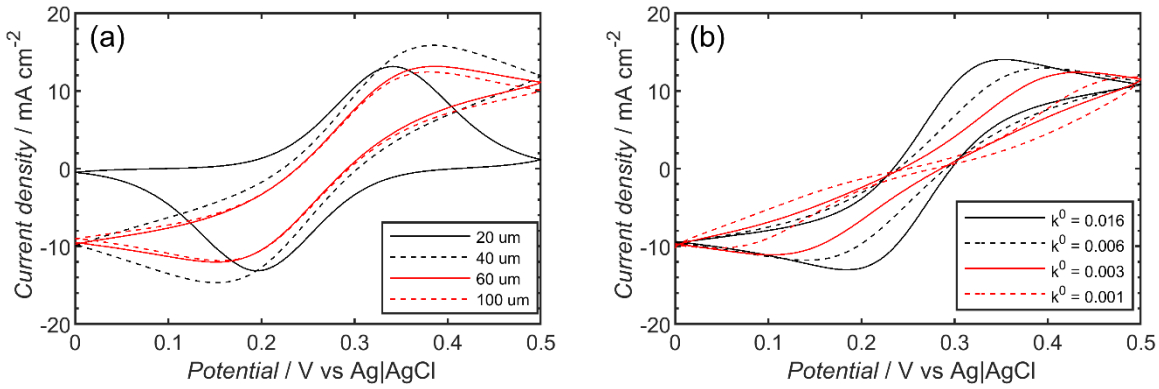

Figure 5.7: Simulated results of cyclic voltammograms at fibres in a solution of 0.1 mM ferricyanide and 0.1 mM ferrocyanide, at a sweep rate of 1000 mVs^{-1}. a) using the average rate constant (0.0075 cm s^{-1}) with different void diameters. b) 60 µm void modelled with a selection rate constants (in cm s^{-1}) from Table 1.

These simulations show that the voltammetric response starts to become independent from the void diameter at diameters greater than 40 µm (Figure 5.7a). This is because the diffusion layer thickness only grows to around 20 µm from the fibre surface and thus fibres in voids with diameters greater than around 40 µm are not affected by the no-flux condition at the void boundary. However, as expected, the cyclic voltammograms of fibres in voids with large diameters are still clearly influenced by the rate constant (Figure 5.7b); thus including the rate constant distribution when modelling carbon felt electrodes is most important at high sweep rates.

As the influence of void size on the cyclic voltammetry at a felt electrode decreases as the sweep rate increases, a felt electrode will approach the average single fibre electrode as the sweep rate increases. Therefore, the rate constant determined by fitting a model which assumes a single rate constant and a void size distribution should also approach the average rate constant determined from measurements at multiple single fibre electrodes. This is indeed found in this work, with the best fit single rate constant obtained for cyclic voltammograms measured at 1000 mV s^{-1} for the carbon felt electrode (0.0071 cm s^{-1}, Table 5.2) agreeing very well with the average value calculated from 12 single fibre electrode measurements (0.0075 ± 0.0030 cm s^{-1}, Table 5.1).

The model used to describe the voltammograms at carbon felt assumes that the reaction occurring on the outer face of the electrode can be excluded from the calculation. To confirm that this assumption is reasonable, the charge transferred between the felt electrode and the redox couple within the felt was calculated based on the felt parameters and compared to the experimental results. For a total felt volume of 0.35 cm^3, void volume fraction of 0.938 and with the felt initially containing 0.1 mM ferricyanide and 0.1 mM ferrocyanide, complete transformation between the two forms of the redox couple would result in 6.4 mC of charge passed. The anodic and cathodic charge was measured from cyclic voltammograms obtained at 50 mV s^{-1} as 6.2 and 5.9 mC respectively, suggesting that the voltammetric response of the felt is dominated by the redox reaction within the felt and that the model can safely exclude the contribution of the outer surface.

5.5. Conclusions

We have presented an innovative approach to quantify the kinetics at single carbon fibre electrodes using experimental results and a simple 1D computational model. Using this method, the rate constant for the ferricyanide and ferrocyanide redox reaction was calculated at 12 different carbon fibres extracted from the same sample of carbon felt. These measurements demonstrated that there were non-uniform kinetics within the carbon felt electrode. Using the experimentally determined rate constant distribution and void size distribution of the carbon felt electrode, it is then possible to accurately simulate cyclic voltammograms at the felt electrodes over a wide range of sweep rates. Importantly, while it is possible to fit the cyclic voltammograms obtained at a single sweep rate to the model using a void size distribution and a single rate constant, it is found that the fitted rate constant varies as a function of sweep rate, highlighting the necessity of accounting for the rate constant distribution in these electrodes.

This new method provides researchers with a more detailed means to quantify the performance of carbon felt electrodes, including the distribution of rate constants in a felt sample. Quantifying the kinetics and rate constant uniformity of the carbon felt electrodes will make it significantly easier to identify and design effective carbon felt modification methods for RFB applications.

5.6. Acknowledgements

The authors thank Dane Gerneke, University of Auckland, for assistance with the micro CT imaging.

6. Using Individual Carbon Fiber Electrodes to Quantify Effects of Thermal Activation

Abstract

The capacitance and standard heterogeneous rate constant for the $Fe(CN)_6^{3-}$ / $Fe(CN)_6^{4-}$ redox couple was measured on four different carbon fiber materials, before and after thermal activation. Thermal activation was carried out in air for 60 minutes at 450 ºC, with up a 38 x increase in capacitance. This showed that the electrochemical active surface increases upon thermal treatment. The apparent rate constant was measured by cyclic voltammetry and electrochemical impedance spectroscopy. It was found that for the largest rate constants, accurate and precise measurements require the use of electrochemical impedance spectroscopy. The apparent rate constant increased after thermal activation for all fibers, by up to a factor of 20,000. For this redox couple the rate constant depends on the surface functionality as well as the electrochemically active surface area, as the increase in the apparent rate constant was much larger than the increase in capacitance.

6.1. Introduction

Grid-scale energy storage is required to enable increased deployment of intermittent renewable energy sources, such as solar and wind generation [191]. Vanadium redox flow batteries have the potential to store large amounts of energy, as the stored energy can be scaled independently of the batteries power output [35]. Graphitic carbon felts are typically used as the positive and negative electrodes, owing to their low cost, conductivity, and favourable surface area / porosity and are mostly inert at the applied potentials during normal operation [192]. However, VRFB performance can still be limited by a number of properties, including poor wettability and electrochemical activity [48, 193, 194].

To improve the performance of the graphite felt electrodes in VRFB, the felt is typically activated or pre-treated with a range of different methods. These methods include but are not limited to oxygen plasma [195, 196], thermal treatment [197-199], electrochemical [91, 200], wet chemical [201], hydrothermal [202], corona discharge [164], hydrogen peroxide [164, 196] and gas-phase modification [203].

The area of an electrode can be calculated from the electric double layer capacitance, C_{DL} if the specific capacitance, c_{DL} is known. However, the c_{DL} of carbon surfaces can vary significantly depending on the nature of the material. For highly ordered pyrolytic graphite (HOPG) the c_{DL} of the basal plane is 2 μF cm^{-2}, $60-70$ μF cm^{-2} for the edge plane and $24-36$ μF cm^{-2} for glassy carbon (GC) [204, 205]. The c_{DL} of the basal plane value is low in part due to its partial semiconducting nature [204].

Felt samples made by the same manufacturer, using the same production methods, but from different production runs (termed a charge in the cited work) varyied in their response to thermal activation [159, 206]. For instance, it was found that charge B had a higher rate of mass loss over the tested temperature range (400-575 ^{o}C) by approximately one order of magnitude compared to charge A, even though the bulk physical properties (proportions of X-ray amorphous carbon, graphitic phases, ash content and crystal lattice parameters) of both charges were very similar.

The untreated felts of both charges had a similar C_{DL} of 40 mF g^{-1}, however the C_{DL} of charge B reached 266-300 mF g^{-1} at the highest treatment temperature of 575 ºC. Meanwhile the C_{DL} of charge A increased steadily reaching only 151 -277 mF g^{-1} at 575 ºC. The area density of the felts was subsequently reported as 0.45 g m^{-2} for charge A and 0.51 g m^{-2} for charge B [207]. Therefore the specific capacitance, c_{DL} for charge A, after treatment at 575 ºC was $33.6 - 61.6$ µF cm^{-2} and $52.2 - 64.7$ µF cm^{-2} for charge B. The results indicate that the thermal treatment increased the ratio of edge to basal plane sites of the two felt samples, as stated in subsequent analysis by the same authors [207].

When activation has been shown to improve the performance of the graphite felt electrodes, there is an ongoing discussion about the mechanism by which these improvements have occurred. Numerous papers identified the presence of oxygen functional groups as the source of improved kinetic performance [109, 169, 197, 201], whilst others have suggested that the increase in performance is largely due to increases in felt electrochemically active surface area. The electrochemically active surface area can be increased with greater surface roughness or improved wettability [177, 208, 209]. Improved wettability has been shown to occur as a result of the polar oxygen groups that are added to the surface during thermal and acid treatments. In both cases the improvement in felt performance is attributed to the oxygen groups added to the surface, but the distinction between increased electrochemically active surface area and electrochemically active functional groups is important for designing the most effective treatment procedures.

Perhaps the source of conjecture is that it is currently difficult to quantify the effect on the felt performance from each felt property. For example, the measured current at an electrode is related to the electrochemically active surface area and the inherent rate constant of a material, as described by the Butler-Volmer equation:

$$i = FAk^0\left(C_{Red}e^{\frac{-\alpha nF(E-E_{rev})}{RT}} - C_{Ox}e^{\frac{(1-\alpha)nF(E-E_{rev})}{RT}}\right) \quad (6.1)$$

Where; i is the recorded current, A is the electrochemically active surface area of the electrode, k^0 is the inherent rate constant, C_{Red} is the concentration of the reduced species at the surface of the electrode, C_{Ox} is the concentration of the oxidised species at the surface of the electrode, R is the universal gas constant and T is the temperature of the system in kelvin.

In this work and often in literature, the electrochemically active surface area (A_{ea}), is assumed to be equal to the geometric area of the electrode (A_g). For instance, this assumption is often applied when using the Nicholson method at planar electrodes and is acceptable as the electrodes are typically finely polished to produce a very smooth surface. However, when using carbon fibers the A_{ea} is likely larger than the geometric surface area, due to surface roughness and or the presence of pores. This means the rate constant value that is calculated from electrochemical measurements is not the inherent rate constant (k^0_{in}), but in fact an apparent rate constant (k^0_{app}):

$$A_g \times k^0_{app} = A_{ea} \times k^0_{in} \quad (6.2)$$

As mentioned previously, both the wettability and roughness of an electrode will change the electrochemically active surface area relative to the geometric area:

$$A_g \times R = A_{tot} \quad (6.3)$$

$$A_g \times R \times W = A_{ea} \quad (6.4)$$

Where R is the roughness factor of the electrode, A_{tot} is the total area of the electrode and W is the wetted fraction of the electrode.

Therefore, it is possible to increase A_{ea} by either increasing the roughness of the surface (likely through the production of pores) or by improving the wettability of the surface. Both of these factors directly influence the electric double layer capacitance of the electrodes. The importance of accounting for the differences in electrochemically active surface area is described further in literature, in terms of the exchange current density which is directly related to the inherent rate constant [177]. It is possible to identify differences in wettability by comparing physical area as measured by BET, relative to electric double layer capacitance. Increases in physical area should be shown with BET analysis, but if the electrolyte cannot wet into the new pores the electric double layer capacitance will remain unchanged.

In this work, thermal activation is used as a model procedure, introducing oxygen groups to the graphite felt surface. We show that by using cyclic voltammetry and electrochemical impedance spectroscopy at single fibers, we can separate the performance effects from the surface area, wettability, inherent rate constant and conductivity.

6.2. Experimental

Four different carbon fiber samples were tested. Three of these fiber samples were extracted from PAN based carbon felts (GFE-1 graphite felt, Cera Materials, USA, G100 and C100, AvCarb, USA) and another was extracted from continuous carbon fiber tows (Toray T700SC 12000-50C).

To thermally activate these carbon fibers, samples were heated in air at 14.2 ^{o}C min^{-1} to 450 ^{o}C and held for 60 minutes, before cooling to room temperature. Each carbon fiber microelectrode was made by gluing a single fiber to an electrical wire using conductive carbon glue. The connection between the carbon fiber and the electrical wire was sealed with epoxy resin. The length of each microcylinder electrode was then determined by optical microscopy and the mean diameter of the different felt samples was calculated from scanning electron micrographs (SEM) collected using a JEOL 7000F.

Electrochemical measurements were made using a Gamry 3000 potentiostat. The electrical double layer capacitance was measured using cyclic voltammetry in 1 M KNO_3 at sweep rates of 0.05, 0.1, 0.2, 0.5 and 1 V s^{-1}. The capacitance was then calculated using the following equation:

$$C = \frac{I_f - I_r}{2v} \tag{6.5}$$

The forward current, I_f and reverse current, I_r were taken at 0.4 V vs Ag|AgCl, as at this potential there were no obvious faradic processes from the surface functional groups (often termed pseudo-capacitance) [210]. All of the capacitance values in this work are from the cyclic voltammetry recorded at 50 mV s^{-1}. The specific capacitance for each electrode was calculated by dividing the total capacitance by the electrode area, calculated using the length and the mean fiber diameter for each fiber type.

Electrochemical measurements were also recorded in a 1 M KNO_3 solution containing 1 mM $K_3Fe(CN)_6$ (Vickers Laboratories Ltd) and 1 mM $K_4Fe(CN)_6$ (BDH AnalaR). The diffusion coefficients were calculated from the limiting current reached during the recording of steady-state polarisation curves and is described further in our previous work [188]. The diffusion coefficients were found to be 8.6×10^{-6} cm^2 s^{-1} for $Fe(CN)_6^{4-}$ and 8.37×10^{-6} cm^2 s^{-1} for $Fe(CN)_6^{3-}$. In this chapter, simulations were carried out using the mean value of $8.50 \pm 0.05 \times 10^{-6}$ cm^2 s^{-1}. Cyclic voltammetry was again recorded at sweep rates of 0.05, 0.1, 0.2, 0.5 and 1 V s^{-1}. Electrochemical impedance spectroscopy (EIS) was recorded at each fiber at open circuit potential, with a 5 mV rms AC perturbation, between 1 MHz and 0.1 Hz frequencies. Calculation of apparent rate constants was carried out using a one-dimensional numerical model for cylindrical electrodes solved using a method of lines approach. A more in depth discussion of the numerical model can be found in Chapter 5.

Raman spectra of each carbon fiber surface was obtained and analysed to identify potential differences in the surface chemistry of the different carbon fibers, before and after thermal activation. Raman spectra measurements were performed using an alpha 300R+ confocal Raman microscope (WiTec, Ulm, Germany) equipped with a 532 nm excitation laser. Spectra acquisition were performed as maps scan across carbon fibers fastened onto a glass slide, over a spectral region of -52 to 3789 cm^{-1}, using a 50x air objective and 15 mW laser power.

6.3. Results and Discussion

Cyclic voltammetry at microcylinders depends on the radius of the electrode, therefore the mean diameter of the four fiber samples calculated from SEM images, Table 6.1.

Table 6.1: Mean diameters calculated from 15 different fibers for each of the four fiber types.

Felt Sample	Diameter (μm)
C100	8.2 ± 0.2
Toray	8.2 ± 0.2
G100	8.7 ± 0.2
GFE	10.0 ± 0.2

The specific capacitance was calculated for individual fibers using the current at 0.4 V vs Ag|AgCl from CVs recorded at 50 mVs^{-1}. The fiber area was calculated by assuming each fiber was a perfect cylinder, with the mean diameters given in Table 6.1. The mean capacitance and related uncertainties for each fiber type was then calculated, with clear differences between the different fibers and a noticeable increase after thermal treatment, (Figure 6.1).

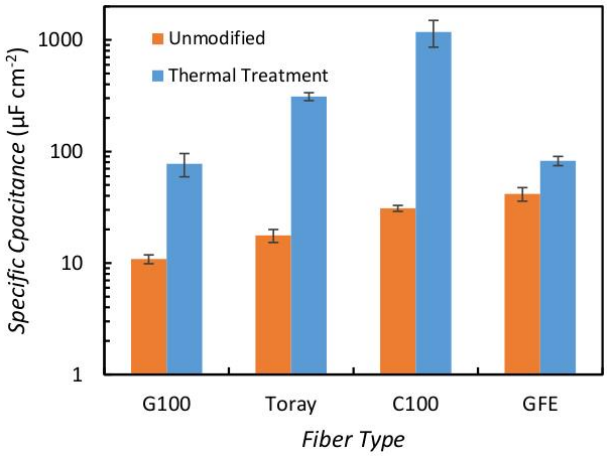

Figure 6.1: Capacitance of each felt type recorded before and after thermal treatment, recorded in 0.5 M H_2SO_4 at a sweep rate of 50 mVs^{-1}.

The difference in measured capacitance between the untreated fiber types could be a result of wettability, surface roughness or differences in the c_{DL} of the carbon material [177]. The c_{DL} reported in this work for the G100, Toray and C100 fiber samples is between that of the HOPG basal plane (2 µF cm^2) and GC (24 – 36 µF cm^2), whilst the c_{DL} of the GFE fibers is at the upper end of the GC range. Therefore, the fibers likely have a low roughness factor and the actual surface area is similar to the geometric surface area.

In literature it was shown that after thermal treatment the fraction of edge plane sites increases, contributing to an increase in capacitance and that thermal treatment improves the wettability of carbon felts [211]. Therefore, the increase in capacitance summarized in (Table 6.2), can be considered as the upper limit for the increase in electrochemically active surface area.

Table 6.2: Change in specific capacitance for each fiber type after thermal treatment.

Felt	**Capacitance Before**	**Capacitance After**	**Factor Increase**
	(µF cm^{-2})	(µF cm^{-2})	
G100	11 ± 1	80 ± 20	7 x
GFE	42 ± 6	83 ± 8	2 x
Toray	18 ± 2	310 ± 30	18 x
C100	31 ± 2	1200 ± 30	38 x

An increase in the electrochemically active surface area should lead to improved electron transfer kinetics at the carbon fiber surface. The current density at a given over-potential should increase linearly with increased surface area, providing that the inherent rate constant has not changed and mass transport limitations are ignored.

To determine if the changes in the capacitance and hence electrochemically active surface area resulted in improved electron transfer kinetics, the electrochemical behaviour of the $Fe(CN)_6^{3-}$ / $Fe(CN)_6^{4-}$ redox couple at the carbon fiber samples was measured using cyclic voltammetry (Figure 6.2).

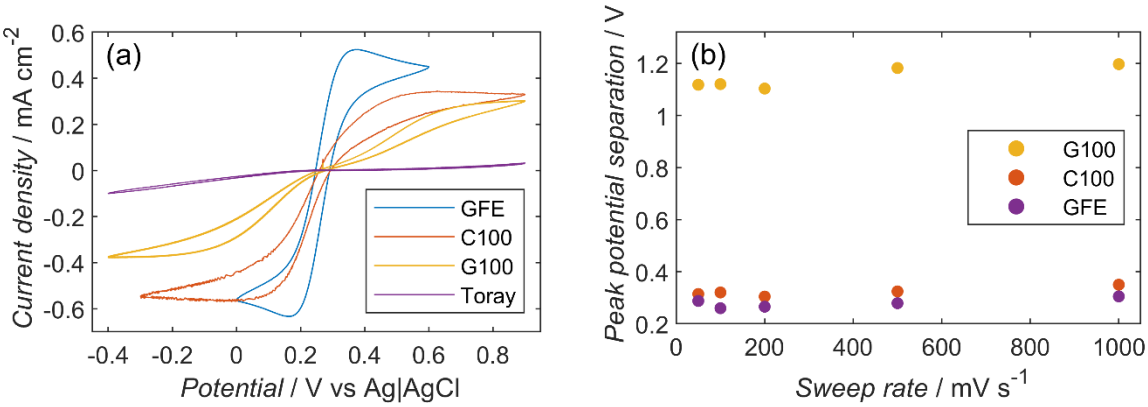

Figure 6.2: a) Cyclic voltammograms of single carbon fiber microelectrodes recorded at 100 mVs^{-1} in a 1 M KNO_3 solution containing 1 mM $K_3Fe(CN)_6$ and 1 mM $K_4Fe(CN)_6$. b) peak separation at different sweep rates for each fiber type, recorded in a 1 M KNO_3 solution containing 1 mM $K_3Fe(CN)_6$ and 1 mM $K_4Fe(CN)_6$.

It has been demonstrated that at cylindrical electrodes the peak potential separation is related to the activity of an electrode towards a redox reaction [142]. Smaller peak separation at a given sweep rate and radius indicates faster electrode kinetics and a larger apparent rate constant. It can be seen from (Figure 6.2b) that the GFE electrodes typically had the smallest peak separations, followed in order by C100, G100 and Toray (not shown as no peaks were present in the recorded CVs).

Thermal treatment was shown to increase the capacitance of each fiber type significantly, as shown in (Figure 6.1). This increase was accompanied by a clear increase in kinetic performance, identified by reduced peak potential separation for each fiber type tested, (Figure 6.3).

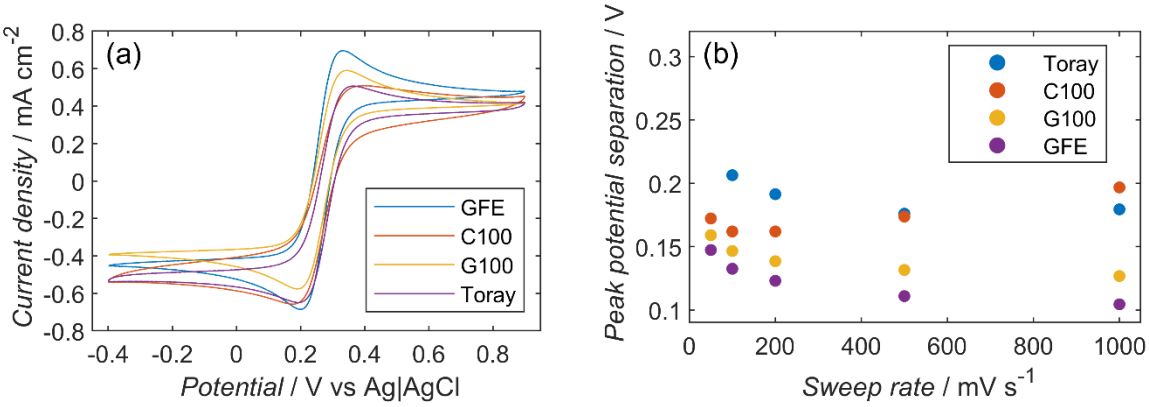

Figure 6.3: a) Characteristic CVs for thermally treated fibers, recorded at 100 mVs^{-1}. b) peak separation at different sweep rates for thermally treated fibers, recorded in a 1 M KNO_3 solution containing 1 mM $K_3Fe(CN)_6$ and 1 mM $K_4Fe(CN)_6$.

From visual inspection of the recorded cyclic voltammetry presented in (Figure 6.3a) it is difficult to distinguish any difference in kinetic performance between the different felt types after thermal treatment. This is due to the much closer spread of peak potential separation between fibers, relative to the peak separations at non-activated fibers shown in (Figure 6.2b).

However, it is not known whether the reduction in peak separation is due to larger inherent rate constants, or due to an increase of the electrochemically active surface area, as observed by the increased capacitance. Therefore, the apparent rate constant must be quantified before and after thermal treatment for each fiber. For this purpose, we use the numerical model detailed in Chapter 5, developed to calculate the rate constant at a cylindrical electrode from the peak potential separation and sweep rate.

Using the model numerical was proven, the apparent rate constant for each tested fiber was calculated, using the peak separations displayed in Figure 6.2. The mean value and uncertainty for each fiber type was then calculated and is summarized in (Table 6.3).

Table 6.3: Mean apparent rate constant for each as-received fiber type, calculated from CVs recorded at 200 mV s^{-1}.

Fiber Type	**Rate Constant**
	(cm s^{-1})
GFE	$4 \times 10^{-3} \pm 3 \times 10^{-3}$
C100	$3 \times 10^{-3} \pm 2 \times 10^{-3}$
G100	$3 \times 10^{-6} \pm 4 \times 10^{-7}$
Toray	$< 2 \times 10^{-7}$

As expected GFE had the largest apparent rate constant, closely followed by C100. The apparent rate constants for GFE and C100 are three orders of magnitude larger than for G100 and at least four orders of magnitude larger than for Toray. This variation is significant and larger than expected, based on the modest expected differences in electrochemically active surface area observed from capacitance measurements. This shows that there are significant differences in the performance of the different fiber surfaces, with larger inherent rate constant values at GFE and C100 fibers, probably due to functional groups at the surface.

As demonstrated earlier, thermal treatment led to reduced peak separations during cyclic voltammertry for all four of the fiber types. To quantify the changes in the kinetic performance, the apparent rate constant was calculated using the previously discussed numerical model, with the mean values are presented in (Figure 6.4).

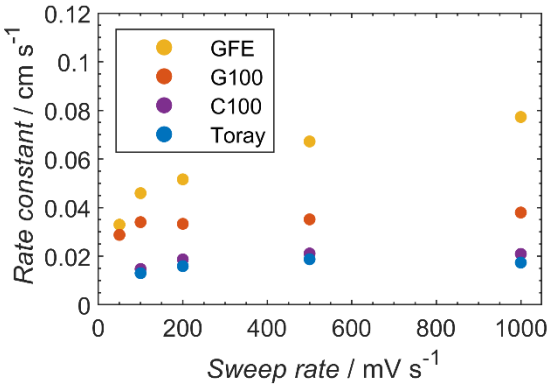

Figure 6.4: Calculated apparent rate constant at different sweep rates for thermally treated carbon fibers in a 1 M KNO_3 solution containing 1 mM $K_3Fe(CN)_6$ and 1 mM $K_4Fe(CN)_6$.

The apparent rate constants calculated using the peak separation are smaller at the slower sweep rates, approaching an asymptote at 1000 mV s^{-1}. At faster sweep rates, the uncertainty associated with identifying the peak potential is reduced. The increased uncertainty at low sweep rates is compounded when the peak separation is relatively small, (Figure 6.5).

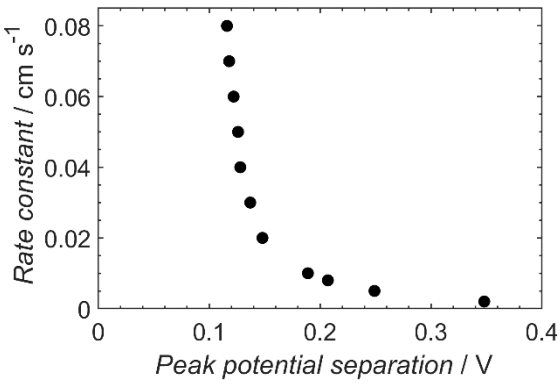

Figure 6.5: Peak separation dependence on apparent rate constant for a 10µm diameter fiber, specific values from CVs modelled at a sweep rate of 200 mVs^{-1}.

When the peak separation is small it becomes very difficult to accurately estimate the apparent rate constant, as small changes in peak separation lead to large changes in the calculated apparent rate constant. For instance, a peak separation of 0.128 V will return $k^0_{app} = 0.04\ cms^{-1}$, whilst a peak separation of 0.116 V will return $k^0_{app} = 0.08\ cms^{-1}$. This sensitivity increases further with smaller peak separation and thus for large apparent rate constants the peak separation is sensitive to the diameter of the fiber, (Figure 6.6).

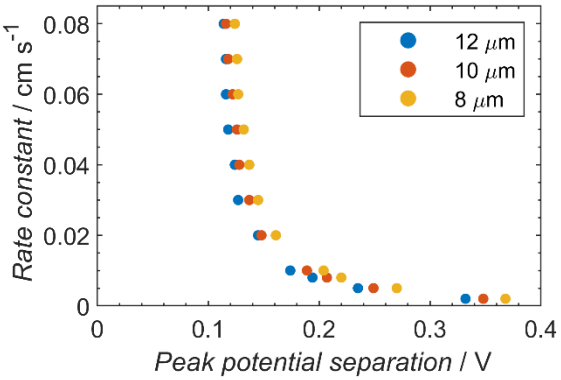

Figure 6.6: Peak separation dependence on fiber diameter and apparent rate constant, specific values from CVs modelled at a sweep rate of 200 mVs^{-1}.

As an example, a 0.124 V peak potential separation at a 12 µm electrode will return $k^0_{app} = 0.04$ cm s^{-1}, but with a 8 µm electrode the same peak potential separation will give $k^0_{app} = 0.08$ cm s^{-1}. As the apparent rate constants calculated from cyclic voltammetry are sensitive to small errors in the calculation of the peak separation and differences in fiber diameter, a more reliable method for calculating the apparent rate constant of these activated fibers is desired.

A model for the electrochemical impedance spectroscopy (EIS) response of cylindrical fibers has been developed and can be used to accurately measure the standard heterogeneous rate constant [188]. This method is described in detail in Chapter 4 of this thesis. Briefly, the modelled response can be fitted to the experimental results using seven physical parameters, Ψ is a composite parameter independent of electrode radius, τ_d is a diffusion time constant, R_{ct} is the charge transfer resistance, R_s is the solution resistance, Υ_0 is the admittance constant which combined with the dimensionless constant ϕ models the double layer capacitance using a constant phase element, (Figure 6.7).

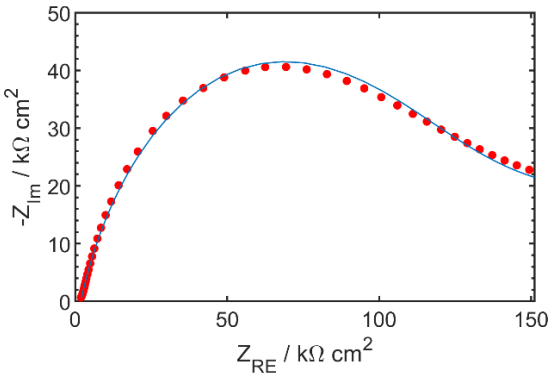

Figure 6.7: Example fit from a thermally treated Toray fiber, EIS recorded at OCP with a 5 mV rms AC perturbation between 10 kHz and 100 mHz. Red circles represent experimental data points; blue line is the fitted model response.

Unlike analysis of cyclic voltammetry, EIS enables the apparent rate constant to be calculated from a composite parameter Ψ, without prior knowledge of the fiber diameter. However, similarly to the numerical cyclic voltammetry model the electrochemically active surface area of the electrode is unknown. Therefore, the geometric area is assumed and the resulting values should be considered as apparent, not inherent rate constants. The apparent rate constant can also be calculated from the fitted R_{ct} parameter, with the electrode geometric area calculated from the measured length and by assuming the diameter of each fiber electrode is the same as the mean value found for that fiber type from SEM analysis, (Table 6.4).

Table 6.4: Rate constant values calculated from EIS measurements.

Fiber Type	**Rate constant (composite parameter)**	**Rate constant (charge transfer resistance)**
	(cm s^{-1})	(cm s^{-1})
GFE Thermal	0.12 ± 0.05	0.09 ± 0.05
G100 Thermal	0.04 ± 0.01	0.02 ± 0.01
C100 Thermal	0.01 ± 0.01	0.012 ± 0.008
Toray Thermal	0.004 ± 0.002	0.003 ± 0.002

The rate constants calculated from Ψ and R_{ct} are in good agreement, implying that there are only minor differences between the diameter of the tested fibers and the mean diameter of each fiber type. The average apparent rate constant values for GFE and G100, as calculated by EIS are in very close agreement with those calculated from CVs, Figure 6.4.

The EIS measurements showed significant differences in apparent rate constants between the different felt types, with all of the apparent rate constants being significantly larger than before the thermal treatment. The increase in apparent rate constants is not proportional to the increase in specific capacitance of the fibers, (Table 6.5).

Table 6.5: Change in electric double layer capacitance (EDLC), apparent and inherent rate constants of carbon fibers (before and after thermal treatment).

Fiber Type	k^0_{app} **Before**	k^0_{app} **After**	k^0_{app} **Increase**	**EDLC Increase**	k^0_{in} **Change**
	(cm s^{-1})	(cm s^{-1})			
G100	0.000003 ± 0.000002	0.04 ± 0.01	10,000 x	7 x	1,400 x
GFE	0.004 ± 0.003	0.12 ± 0.05	30 x	2 x	15 x
Toray	<0.0000002	0.005 ± 0.003	> 20,000 x	18 x	> 1,100 x
C100	0.003 ± 0.002	0.02 ± 0.01	6 x	38 x	- 6 x

The increase in rate constant for GFE, Toray and G100 are significantly larger than the increase in capacitance, which as discussed previously can be thought of as an upper limit for the increase in electrochemically active surface area. This strongly suggests that there was a change in the amount and or type of functional groups at the surface. As the thermal treatment was carried out in an air atmosphere, these functional groups likely contain oxygen, which has been shown in literature to improve performance for a range of redox couples [131, 197, 201].

Raman spectroscopy on the different fiber types before and after thermal treatment was carried out, with the aim of identifying differences in the surface structure which may relate to the difference in response to thermal treatment. The experimental measurements and analysis were done by Chima Robert and Keith Gordon, from the University of Otago, Department of Chemistry. Raman spectroscopy is often used to characterise carbon materials [212-216]. Empirical relationships using the intensity ratio of the defect-induced Raman D band and the bulk G band $\left(\frac{I_D}{I_G}\right)$, can be applied to calculate the mean crystallite sizes L_a [212]. Typically, larger crystallite sizes are indicative of a more ordered and highly graphitic carbon material. The D and G band intensities and calculated mean crystallite size are reported for each fiber type, (Table 6.6).

Table 6.6: Important Raman spectra properties for each fiber type tested in this work.

Fiber type	**Area (D-band)**	**Area (G-band)**	**I_D / I_G**	***La* (Å)**
C100	29,700	6,500	4.57 ± 0.10	9.63 ± 0.60
C100 thermal	15,500	3,900	3.93 ± 0.07	11.20 ± 0.24
G100	45,700	41,700	1.10 ± 0.03	40.00 ± 1.14
G100 thermal	44,500	41,100	1.08 ± 0.05	40.74 ± 1.06
GFE	71,500	40,600	1.76 ± 0.03	25.00 ± 0.39
GFE thermal	34,000	18,100	1.88 ± 0.11	23.40 ± 1.61
Toray	146,100	49,900	2.93 ± 0.07	15.02 ± 0.38
Toray thermal	13,100	4,200	3.14 ± 0.02	14.01 ± 0.21

C100 and Toray fibers had much higher D band intensities relative to the G band, indicating a larger mean crystallite size, higher level of disorder and lower graphitic content than the GFE and G100 fibers. Therefore, during thermal treatment in air, the C100 and Toray fibers should be more easily oxidised. The increase in capacitance for C100 and Toray fiber was more significant than for G100 and GFE fibers, which is consistent with the expected higher level of oxidation.

Thermal treatment did not appear to significantly alter the D to G band ratios and hence mean crystallite size, which is to be expected as higher temperatures would be required to increase the graphitic content. However, it is clear that the surface did change significantly, supported by both the CV and EIS measurements. Thus, the surface changes from thermal treatment were likely not related to the graphitic nature of the carbon, but instead an increase in the number of oxygen-containing functional groups at the surface, as previously reported for thermal treatment in air [126]. Surface oxygen groups are difficult to detect with Raman spectroscopy, as the G band from carbon is superimposed over the O-H bending and C=O Raman peaks [217]. Oxygen functional groups should improve the wettability of the fibers and provide active sites for the redox reactions, consistent with the increase in electric double layer capacitance and improved electrochemical performance that was recorded after thermal treatment.

6.4. Conclusions

Clear differences between the untreated four fiber types (GFE, G100, C100 and Toray) were present in electric double layer capacitance, as well as kinetic performance. Fibers were thermally treated for 1 hour at 450 ^{o}C, with a large increase in the electric double layer capacitance observed at C100, G100 and Toray fibers, whilst the electric double layer capacitance for GFE only doubled. Each fiber had clear improvements in kinetic performance, with significantly smaller peak separations observed for each fiber type. The apparent rate constant was then calculated for each fiber before and after thermal treatment. The inherent rate constant could not be directly calculated as only the geometric area of the fiber electrodes was known, not the electrochemically active surface area. EIS measurements were shown to be more accurate for fibers with higher apparent rate constants, where k_{app}^{0} approaches 0.1 cm s^{-1}. This was due in part to the sensitivity of the fitted k_{app}^{0} value to peak separation, as well as the ability to calculate k_{app}^{0} from EIS without the need to know the radius of the fiber.

7. Thermal Activation of Carbon Felt for the Positive Vanadium Redox Couple

Abstract

It has been reported that thermal activation of carbon felt electrodes improves the energy efficiency and maximum power of VRFBs. Some work in literature has assigned the improvements to formation of functional groups at the surface, increasing the inherent rate constant. Others have suggested the improvements are due to larger electrically active surface areas, from increased roughness of the surface or improved wetting. In this work we separate out these effects to identify the source of changes in felt performance, with thermal treatments carried out in air for one hour at 200 to 700 ^{o}C, for each of the three felts.

The capacitance of each felt was calculated from cyclic voltammetry, this was compared to the physical surface area, measured with BET. Raman spectroscopy and thermal gravimetric analysis provided insight into the different responses to thermal treatment between the three felts. The apparent rate constant for VO^{2+} oxidation and VO_2^{+} reduction at each felt was then calculated from cyclic voltammetry and compared to the changes in capacitance and physical surface area. Thermal treatment increased the capacitance and physical area for all three felts, however the relative increase was different for each felt type. The highest apparent rate constant was recorded for the GFE felt treated at 600 ^{o}C, with $k_{app}^{0} = 8.5 \times 10^{-5}$ cm s^{-1}. This value is in agreement with those reported in literature for the same redox couple at carbon electrodes.

7.1. Introduction

Thermal treatment has been shown in numerous studies to improve the round trip efficiency of VRFB cells [167, 218-220]. Explanations given for the improved efficiency include an increase in oxygen functional groups at the surface, increased electrode area from pitting and improved wettability. However, as discussed in Chapter 4, accurate quantification of the carbon felt kinetics is challenging. Accurate quantification of the inherent kinetics will enable identification of the most effective physical and chemical changes possible.

It has been shown that cyclic voltammetry and EIS of single carbon fibers electrodes can be used to calculate the apparent rate constant distribution of a carbon felt sample, Chapter 4. This data can then be used to accurately model the behaviour of a carbon felt sample, if the void size distribution is known. However, for the VO^{2+} to VO_2^+ oxidation reaction and subsequent reduction reaction, the standard reduction potential, $E^0 = 1.00\,V\ vs\ S.H.E$ is close to the standard reduction potential of the water splitting reaction, $E^0 = 1.23\,V\ vs\ S.H.E.$ As the kinetics for the VO^{2+} to VO_2^+ oxidation reaction is considerably lower than for the $Fe(CN)_6^{3-}$ / $Fe(CN)_6^{4-}$ redox couple, it is not possible to record a vanadium oxidation peak at a single carbon fiber electrode. The applied overpotential required to achieve vanadium redox peaks leads to large current contributions from water splitting, preventing accurate analysis of cyclic voltammetry measurements. However, as discussed in Chapter 2 due to the relatively small voids within carbon felt, the peak separation during cyclic voltammetry at carbon felt electrodes is significantly reduced, relative to a single fiber electrode. If the sweep rate is low enough for the rate constant of the chosen electrode, it is possible to record clear vanadium oxidation peaks. Whilst it has been shown that EIS is a more reliable method for calculating the rate constant of single carbon fibers, this is not a practical option for measuring the kinetics at a felt sample, as there is no validated model to account for the void size distribution within the felt.

7.2. Experimental

Three different carbon fiber samples were tested, all of which were PAN based carbon felts (GFE-1 graphite felt, Cera Materials, USA, G100 and C100, AvCarb, USA). Thermal treatment of the carbon felt samples was carried out by heating in air for 1 hour at 200 ^{o}C, 300 ^{o}C, 400 ^{o}C, 500 ^{o}C, 600 ^{o}C and 700 ^{o}C. With the mean diameter of the different felt samples calculated from scanning electron micrographs (SEM), as detailed in Chapters (4-6). The capacitance and kinetic performance of each felt was tested using cyclic voltammetry. The capacitance was recorded at 50, 100, 200, 500 and 1000 mVs^{-1} in solution of 0.5 M H_2SO_4. With the kinetic performance analysed from cyclic voltammetry recorded in a 1 mM $VOSO_4$ (Alfa Aesar) and 0.5 mM V_2O_5 in 0.5 M H_2SO_4 electrolyte solution at 2, 5 and 10 mVs^{-1}. All cyclic voltammograms were recorded in a custom designed and built cell, (Figure 7.1).

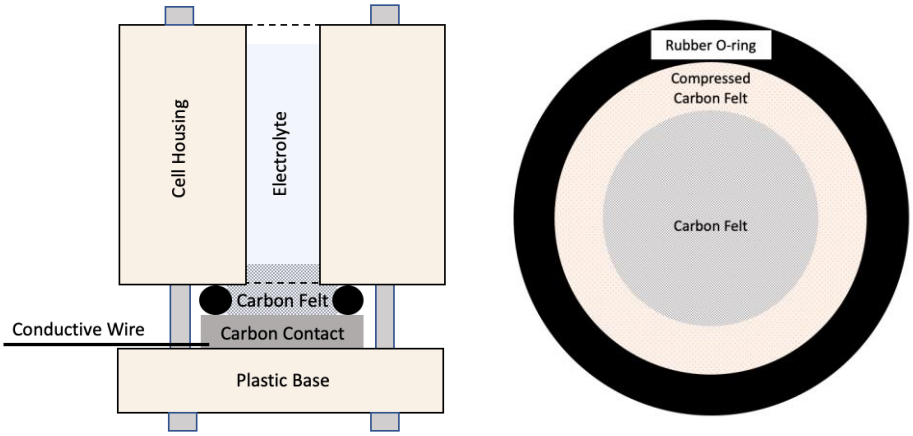

Figure 7.1: Cell design for measuring cyclic voltammetry at thermally modified carbon felt samples.

Preliminary tests in a similar cell used showed that G100 felt in particular was not easily wetted by the 1 mM VO^{2+} / VO_2^{+} in 0.5 M H_2SO_4 electrolyte. Therefore, this cell was designed to reduce the influence of wetting differences on kinetic measurements. Improvement in repeatability and wetting in this cell was made possible through the ability to flow electrolyte through the felt sample using a syringe. When electrolyte was forced through the felt air bubbles were visibly removed, increasing the wetted area of the felt.

The electrolyte concentration of 1 mM VO^{2+} and VO_2^+ was selected to balance faradaic, capacitive and resistive features. For a 1 mM concentration, the faradaic response was much larger than the electric double layer charging, but higher concentrations increase the uncertainties of calculating the peak separation, due to larger electrical resistance corrections. In this work electrical resistance was measured before cyclic voltammetry using hybrid EIS scans, recorded at frequencies between 200 kHz and 0.01 Hz with a 5 mV rms perturbation. The impedance recorded at 0^o phase angle was then taken as the electrical resistance for the felt and the solution. 80% of the resistance was corrected for using positive feedback correction during cyclic voltammetry, with the remaining 20% correct for post run.

The effect of thermal treatment on felt physical area and mass loss was investigated using BET and thermal gravimetric analysis (TGA) respectively. BET measurements were carried out using a Gemini VII 2390, Surface Area Analyzer. TGA measurements were carried out in an air atmosphere, starting at room temperature (23 °C) and ramping up to 1000 °C at 5 °C min^{-1}.

7.3. Results and Discussion

7.3.1. Capacitance

The capacitance of each felt was recorded in a 0.5 M H_2SO_4 solution, and was found to increase with thermal treatment temperature. The surface area of each felt was calculated from the mass of the sample and the geometric area, assuming the fibers perfect cylinders all with the mean diameter for that sample calculated from SEM imaging. Similar capacitance changes are reported in Chapter 6, but are now measured over a range of different treatment temperatures, (Figure 7.2).

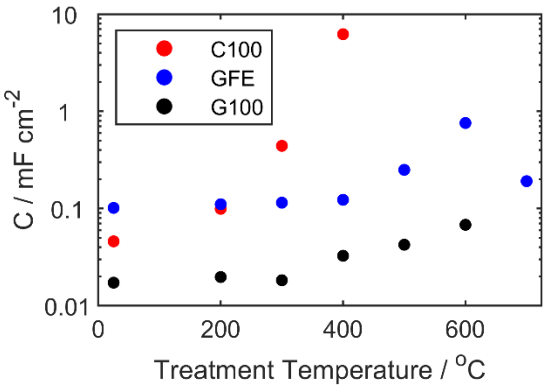

Figure 7.2: Capacitance of each treated felt measured in 0.5 M H_2SO_4 from cyclic voltammetry recorded at 100 mVs^{-1}.

Of the three samples, the capacitance of C100 increased the most with thermal treatment, confirming the results reported in the previous chapter. The larger increase in capacitance is consistent with the fact that C100 had a much smaller mean crystallite size of 9.63 ± 0.60 Å, compared to 40.00 ± 1.14 Å for G100 and 25.00 ± 0.39 Å for GFE, as calculated from Raman spectroscopy. The smaller crystallite size is indicative of lower graphitic content, and thus C100 is more readily oxidised during the thermal treatment in air.

Interestingly the capacitance of GFE felt declined between 600 ^{o}C and 700 ^{o}C. The cause of this is unknown, but it does coincide with a noticeable decrease in mass of the felt. The change in capacitance at each thermal treatment is quantified relative to the as-received felts, (Table 7.1).

Table 7.1:Change in capacitance relative to control felt for thermal treatment of each felt from cyclic voltammetry recorded in 0.5 M H_2SO_4 from cyclic voltammetry recorded at 100 mVs^{-1}.

Treatment	**Capacitance Increase**		
(^{o}C)	G100	GFE	C100
200	1.1	1.1	2.2
300	1.1	1.1	9.6
400	1.9	1.2	135.3
500	2.5	2.5	-
600	3.9	7.5	-
700	-	1.9	-

7.3.2. Physical area measurements using BET

As previously mentioned in Chapter 6, the increase in capacitance can be caused by a combination of three factors. Thermal treatment can oxidise the surface, forming pores and increasing the roughness of the electrode. This increases the physical area of the electrode and can be measured using BET isotherms. The ratio of basal to edge plane sites can also alter the capacitance significantly, as the specific capacitance of the basal plane is 2 μF cm^2, increasing to $60 - 70$ μF cm^{-2} for edge plane sites. Finally, the wettability of the felt also influences the capacitance, if only a fraction of the physical area of the felt is wetted the measured capacitance will be reduced. BET measurements were conducted on the untreated and thermally treated felt samples, with GFE felt thermally treated at 600 ºC, G100 at 500 ºC and C100 at 400 ºC. The expected specific surface area for each carbon felt was calculated assuming perfectly smooth cylindrical fibers, with the average fiber diameters for each felt reported in Chapter 6 and assuming a density of 2 g cm^{-3} for the carbon fibers, (Table 7.2).

Table 7.2: Specific surface area of the different carbon felts based on fiber diameter and BET measurements.

Felt Type	Expected	Untreated	Roughness	Thermally Treated	Increase
	(m^2 g^{-1})	(m^2 g^{-1})	Factor	(m^2 g^{-1})	Factor
C100	0.24	0.39	1.6 x	6.00	15.3 x
G100	0.22	0.37	1.7 x	0.61	1.6 x
GFE	0.2	0.36	1.8 x	6.92	19.1 x

The roughness factors are modest and feasible and suggest that there is a consistently high level of wetting.

The increase in GFE area from thermal treatment at 600 ^{o}C by a factor of 19.3, is larger than the increase in capacitance of 7.5 x. Thermal treatment is expected to increase the specific capacitance by increasing the number of edge plane sites, thus the smaller increase in capacitance may be a result of incomplete wetting of the thermally treated felt. Incomplete wetting of the felt is possible, in particular if there are small pores at the surface. The small pores can be filled by the nitrogen gas during BET measurements, but may be hydrophobic or too narrow to enable complete wetting by the electrolyte. The increase in G100 capacitance of 2.5 x was slightly larger than the increase in physical area of 1.6 x, this discrepancy is small and could be due to an increase in the number of edge sites, or improved wettability. C100 had a much larger increase in capacitance of 135.3 x, than physical area as measured by BET of 15.3, indicating a large increase in the ratio of edge plane to basal plane sites.

7.3.3. Thermo-gravimetric analysis

Thermal gravimetric analysis (TGA) was carried out to understand why the three carbon felts respond differently to thermal treatment. The felt mass was recorded as the temperature was linearly ramped at 5 ^{o}C min^{-1}, (Figure 7.3).

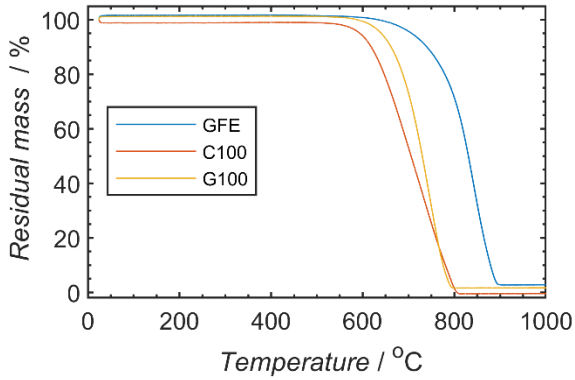

Figure 7.3: TGA measurements for the three tested felt samples, TGA measurements were carried out in an air atmosphere, starting at room temperature (23 °C) and ramping up to 1000 °C at 5 °C min^{-1}

GFE felt was the most thermally stable, losing the same mass percentage as G100 felt at approximately 100 °C higher temperature. This result is unexpected, as G100 felt had smaller increases in capacitance and physical area than GFE. The C100 felt began losing mass before G100 felt, however the slope of the mass loss was lesser, thus they both fully decomposed at approximately 800 °C. The onset of capacitance increases occurs at temperature below those at which TGA shows mass loss. This may be due to changes in basal to edge plane ratios at the surface, leading to electrical double layer capacitance increases before the formation of pores change the physical surface area. Alternatively, the surface area may increase significantly with very minor changes in felt mass, if the formation of pores only changes the total mass slightly. In the thermal treatment procedure, the felts are held at a fixed temperature for one hour, whilst the TGA data was recorded with a 5 ^{o}C min^{-1} ramp rate. This likely causes a lag in the temperature at which surface changes occur during TGA analysis.

7.3.4. Kinetics from cyclic voltammetry

In the previous chapter, it was found that the thermal treatment of single fiber electrodes had a significant effect on the kinetics of the $Fe(CN)_6^{3-}$ / $Fe(CN)_6^{4-}$ cyanide redox couple. In that investigation it was found that the apparent rate constant at untreated GFE felt was larger than at C100, which in turn was larger than at G100. Thermal treatment improved the kinetics at all three felts, with G100 increasing significantly. Here we investigate the apparent kinetics of the same felts for the VO^{2+} / VO_2^+ redox couple over a wide range of thermal treatment temperatures.

As previously mentioned, determining the kinetics of vanadium redox reaction on single fiber electrodes from cyclic voltammetry is not possible, but can be achieved at felt electrodes. However, direct comparison between the felt types based on peak separation is difficult, as the pore size distribution of each felt will vary. BET measurements showed the specific surface area of the three felts is very similar, Table 7.2, therefore large differences in peak potential separation are indicative of differences in kinetics. Clear differences in peak separation between the three felts was observed during cyclic voltammetry, (Figure 7.4).

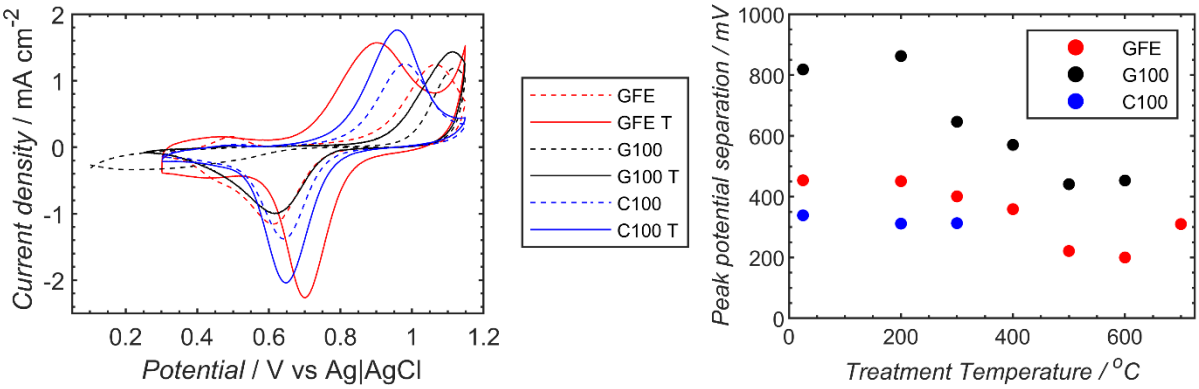

Figure 7.4: a) As-received and thermal treatment with closest peak separation cyclic voltammograms recorded for each felt type. B) peak separation of three different carbon felts. All recorded in 1 mM V^{4+} and V^{5+} in 0.5 M H_2SO_4. Cyclic voltammetry recorded at 5 mV s^{-1}, all data corrected for IR voltage drop, explained further in method section.

As expected the redox peaks in Figure 7.4 are centred around the standard reduction potential of the VO^{2+} / VO_2^+ redox couple, at 0.8 V vs Ag|AgCl. Peaks are seen at felt electrodes but not

at single fiber electrodes, due to depletion of the reactants in the felt voids, causing the concentration at the electrode surface to decline faster. The peak potential separation during cyclic voltammetry is an indicator of kinetics, with closer peaks indicating faster kinetics for a given void distribution. There is evidence of unwanted side reactions at the thermally treated GFE electrode. This is likely the oxygen evolution reaction, which has a standard reduction potential of 1.03 V vs Ag|AgCl. The thermal treatment of the GFE electrode therefore improved the apparent rate constant for the VO^{2+} / VO_2^+ redox couple as well as the water splitting reaction. The peak heights and distance from the standard reduction potential differ for a number of the electrodes, indicating that the charge transfer coefficient, α is not always close to 0.5, as was observed for the $Fe(CN)_6^{3-}$ / $Fe(CN)_6^{4-}$ redox couple, investigated in Chapters 4-6.

Of the untreated felts, C100 clearly had the smallest peak separation at 339 mV, compared to 452 mV for GFE and 818 mV for G100. Thermally treating the felts in air for 1 hour was shown to have a positive effect on the reaction kinetics, with large reductions in peak potential separation observed at GFE and G100 felts. Cyclic voltammetry could not be carried out for G100 at 700 °C, as the felt had oxidised and lost mechanical integrity, with the same phenomena occurring for C100 at 600 °C and GFE at 800 °C. Measurement of the peak potential separation during cyclic voltammetry using the C100 felt was not possible after treatment at 400 °C and above, due to the large increase in capacitance demonstrated in Figure 7.2.

From the peak separation the mean apparent rate constant of the carbon felts can be found, if the void size distribution is known. In this work we were restricted to only having micro-CT data for an uncompressed GFE felt sample. Identification of the mean rate constant in this cell set up is further complicated by the compression exerted around the outer rim of the felt sample, likely causing a reduction in the average felt thickness, changing the pore size distribution slightly.

The volume of the indirectly compressed section of felt was estimated by comparing the charge transferred during cyclic voltammetry to the number of moles of vanadium held within the felt, calculated from the felt void volume and the electrolyte concentration. GFE 400 ^{o}C was selected as it did not have a large water splitting contribution to the current, as observed on the GFE felts treated at 500 ^{o}C and above. However, it was more active towards the vanadium redox reaction than the felts treated at lower temperatures and therefore more likely to have fully oxidised and reduced the vanadium within the felt during each sweep.

From integration, the charge transferred during oxidation (C_{ox}) was found to be $C_{ox} = 0.0251\ C$ and during reduction $C_{red} = 0.0236\ C$. This charge transferred is equivalent to $n_{ox} = 0.245\ \mu mol$ and $n_{red} = 0.260\ \mu mol$ of vanadium. Based on the non-compressed felt thickness of 3.5 mm, the diameter of 7.5 mm, the porosity of 94% and total vanadium concentration of 2 mM, the number of moles of vanadium that can be oxidised or reduced each cycle is $n_{van} = 0.290\ \mu M$. Therefore, the number of moles of vanadium converted is between 85 and 90% of the expected value for an uncompressed felt. The discrepancy is small and can be explained by a combination of a small reduction in volume of the felt voids due to compression, as well as incomplete oxidation and reduction during the cyclic voltammetry. Therefore, the void volume reduction of the felt was minimal and it is reasonable to use the void size distribution calculated from micro-CT imaging at GFE for analysis of the felts tested in this work.

The charge transfer coefficient, α for the reaction at each felt sample tested was approximated as:

$$\alpha = \frac{I_{p_a}}{I_{p_a} + |I_{p_c}|} \tag{7.1}$$

This accounts for differences in kinetic performance for the oxidation and reduction reactions, enabling a more accurate apparent rate constant to be calculated.

The mean apparent rate constants for each felt and treatment procedure was then calculated, assuming the same pore size distribution as the GFE felt, defined in Chapter 5. It is likely that the C100 and G100 felts have a slightly different pore size distribution, however this is not expected to make a significant difference as previously mentioned all three felts have very similar porosity, (Figure 7.5).

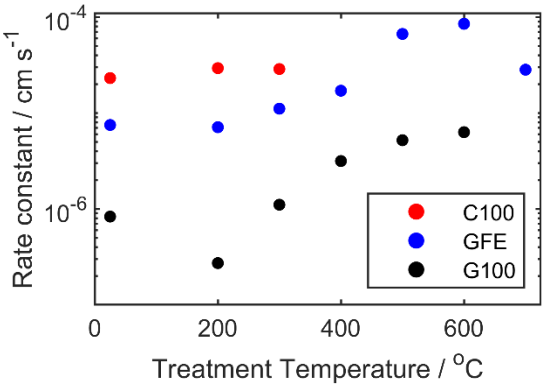

Figure 7.5: Mean apparent rate constant for the different treated and untreated felt samples.

As expected the GFE and C100 felts typically had much higher rate constants than the G100 felt. For the untreated felts G100 $k^0 = 8.31 \times 10^{-7}$ cm s^{-1}, GFE $k^0 = 7.5 \times 10^{-6}$ cm s^{-1} and C100 $k^0 = 2.31 \times 10^{-5}$ cm s^{-1}. The largest mean apparent rate constant measured was for GFE felt treated at 600 °C, with $k^0 = 8.52 \times 10^{-5}$ cm s^{-1}. These values are in close agreement with rate constant values stated in literature, Bourke et al. reported a rate constant of 1.83×10^{-5} cm s^{-1} at carbon felt for the same reaction, whilst Stimming et al reported $3.8 \pm .6 \times 10^{-6}$ cm s^{-1} for the same reaction at a carbon nanotube electrode [88, 125].

As with capacitance and physical area, the mean apparent rate constants of the thermally treated carbon felts generally increased with thermal treatment, (Table 7.3).

Table 7.3:Change in mean apparent rate constant for each felt treatment.

Treatment	**G100**	**GFE**	**C100**
^{o}C	Factor Increase	Factor Increase	Factor Increase
200	0.3 x	0.95 x	1.27 x
300	1.3 x	1.48 x	1.24 x
400	3.8 x	2.28 x	-
500	6.3 x	8.90 x	-
600	7.6 x	11.35 x	-
700	-	3.77 x	-

The increase in the apparent rate constant for GFE from thermal treatment at 600 ^{o}C by a factor of 11.35, is only slightly larger than the increase in capacitance of 7.5 x, but smaller than the increase in physical area of 19.3 x. Therefore, there is no clear evidence to suggest the thermal treatment changed the inherent rate constant of the GFE carbon felt, but the increased surface area clearly increased the apparent rate constant.

The increase in apparent rate constant for G100 felt thermally treated at 500 ^{o}C of 6.3 x, is larger than the recorded increase in capacitance of 2.5 x and physical area of 1.6 x. This indicates that the thermal treatment increased the inherent rate constant of the G100 felt, as well as the electrically active surface area. This result is consistent with the results from the $Fe(CN)_6^{3-}$ / $Fe(CN)_6^{4-}$ redox couple measurements at G100 in Chapter 6, where the apparent rate constant also increased significantly more than the capacitance. The increased inherent rate constant is likely the result of oxygen containing functional groups forming at the surface during thermal treatment.

No apparent rate constant could be measured at thermally treated C100 felt as previously mentioned. However, there appeared to be little change in kinetic performance at 300 ^{o}C, at which point the capacitance had already increased by a factor of 9.6 x. BET measurements at C100 treated at 400 ^{o}C showed 15.3 x increase in the physical area. This suggest that thermal treatment of C100 felt increases the electrically active surface area, but reduces the inherent rate constant. The same trend was seen in Chapter 6 with the $Fe(CN)_6^{3-}$ / $Fe(CN)_6^{4-}$ redox couple, where the C100 capacitance increased more significantly than the apparent rate constant.

These results show that increases in the electrically active surface area of the carbon felt electrodes are important, as stated by Stimming et al [177]. However, there is sufficient evidence to suggest that the inherent kinetics at the carbon surface do change with thermal treatment. Therefore, it is likely that there are functional groups that can be introduced or removed during thermal treatment, that alter the inherent rate constant for the VO^{2+} / VO_2^{+} redox couple. These results are supported by observations that oxygen functional groups alter the kinetics during electrochemical treatment, made by Miller et al [158].

7.4. Conclusions

Using our previously validated model for modelling cyclic voltammetry at carbon felts with specific void size distributions, we were able to calculate the mean apparent rate constant for three different felts (C100, GFE, G100), thermally treated in air for 1 hour at temperatures between 200 and 700 °C. Cyclic voltammetry showed significant differences in peak separation, in particular between the untreated felts. The difference in rate constants for the untreated felts range from $k_{app}^{0} = 8.31 \times 10^{-7}$ cm s^{-1} for G100, $k_{app}^{0} = 7.5 \times 10^{-6}$ cm s^{-1} for GFE and $k_{app}^{0} = 2.31 \times 10^{-5}$ cm s^{-1} for C100. The largest mean apparent rate constant measured was for GFE felt treated at 600 °C, with $k^{0} = 8.52 \times 10^{-5}$ cm s^{-1}. Increased electrically active surface area likely explains the increased apparent rate constant for GFE. However, the increase in rate constant for G100 was significantly larger than the increase in electrically active surface. Therefore, thermal treatment likely introduced oxygen containing functional groups on the G100 surface, increasing the inherent rate constant.

8. Half - Cell Performance of Carbon Felt Samples

Abstract

Polarization curve and charge / discharge cycling measurements are the most common methods for assessing the performance of VRFB cells in current literature. Both methods provide useful information, but neither provides a complete picture. Typically, only the discharging step is reported for polarization curve work, whilst charge / discharge cycling calculations are complicated by the crossover of vanadium ions during the long duration experiments. Often it is not known what contribution to the overpotential is from the positive and negative redox reactions. In this work, we have used half-cell measurements of the positive vanadium electrolyte, carrying out both polarization curves and charge / discharge cycling for a range of different felt samples. From the polarization curve measurements, the apparent rate constant of the different carbon felts was calculated and compared to the energy efficiency recorded during charge / discharge cycle measurements. Both methods were found to be in agreement, as felt samples with higher apparent rate constants had higher energy efficiencies during charge / discharge measurements.

8.1. Introduction

There appears to be two prevailing methods in literature for testing the performance of VRFB cells; polarization curves and charge / discharge cycling [221]. Both methods provide useful data, but also face significant experimental challenges that must be considered.

8.1.1. Polarization Curve Measurements

The main performance indicator that can be extracted from polarization curve data is the overpotential to achieve a set current density, thus better performing cells will have lower overpotentials over a range of current densities. Additionally, the peak power density can be found, which occurs at a compromise between current density and cell potential.

8.1.2. Methods Used

Polarization curves are typically recorded by measuring the charging or discharging current at a range of current densities, with the potential for each current density taken from the average of a short test, typically 30 s. The SOC of the electrolyte used is typically 100% or 50% and can be maintained by either using a single pass of electrolyte [73]. Holding a constant SOC removes the influence of changes to the standard reduction potential from changes in the electrolyte concentration, following the relationship outlined by the Nernst equation:

$$E = E^0 - \frac{RT}{nF} ln\left(\frac{[R]}{[O]}\right) \tag{8.1}$$

Where E is the reduction potential of the redox couple in the half cell at a given point in time, E^0 is the standard reduction potential of the redox couple, R is the standard gas constant, T is the temperature of the cell, n is the number of moles of electrons transferred per mole of species, F is Farraday's constant, $[R]$ is the concentration of the reduced species in the bulk, $[O]$ is the concentration of the oxidised species in the bulk.

Maintaining a fixed state of charge also minimises the influence of changes to the mass transport limitations, as the concentrations of the reactants and products are fixed. The main limitation of polarization curve analysis is that the coulombic efficiency of the cell cannot be measured, therefore the contribution to the current from side reactions such as oxygen evolution (water splitting), carbon oxidation or hydrogen evolution is unknown. This limitation mainly applies at higher current densities and will depend on electrolyte concentration and flow rate.

8.1.3. Findings from literature

Chen *et al.* [222] measured a polarization curve for the discharging of a fully charged cell (SOC =100%) with fluorinated sulfonated poly(arylene ether) SFPAE membranes of three different thicknesses (28, 45 and 80 μm). The cell was fully charged using a 100 mL solution of 1.4 M $VOSO_4$ dissolved in 2 M H_2SO_4 as the positive electrolyte and 50 mL of the same solution as the negative electrolyte. The polarization curve for the cell was measured in 10 mA cm^{-2} current density increments, from 10 mA cm^{-2} through to 700 mA cm^{-2}, with the potential for each step reported as the average potential over 30 s. The peak power densities recorded for the cells with 28 μm, 45 μm and 80 μm membranes were 267 mW cm^{-2}, 311 mW cm^{-2} and 253 mW cm^{-2}, respectively. The 45 μm membrane therefore provides the best compromise between voltage efficiency and vanadium crossover of the three membranes tested.

Liu *et al.* [223] investigated the effect of electrode surface area on the polarization curve using different layers of 0.4 mm thick SGL 10AA carbon paper electrodes, with a geometric area of 5 cm^2. In this configuration, the optimal number of carbon paper layers was found to be three, recording a peak power density of 557 mW cm^{-2}.

The electrolyte flow rate has a significant influence on mass transport limitations, but experimental flow rates are not always stated. Aaron *et al.* [224] carried out polarization curve measurements at different electrolyte flow rates to estimate the mass transport limitation for the discharging step. At 0.5 mL min^{-1} this was found to be 40 mA cm^{-2}, increasing to 321 mA cm^{-2} at 25 mL min for a 1 M VO_2^+ in 5 M H_2SO_4 positive electrolyte and 1 M V^{2+} in 5 M H_2SO_4 negative electrolyte. The cell used a 0.2 mm thick Toray carbon paper electrode with a geometric area of 5 cm^2.

8.1.4. Charge / Discharge Cycling Measurements

Charge / discharge cycling is widely used and provides the definitive measure of cell performance, the round trip energy efficiency. Increased round trip energy efficiency for a given current density, indicates a higher performance cell. As discussed in Chapter 2, the energy efficiency is the product of the voltage efficiency and the coulombic efficiency.

8.1.5. Methods Used

Charge / discharge cycling is typically carried out by setting a fixed current for both charging and discharging, with fixed upper and lower potential limits at which the current is reversed. There are a number of factors that must be considered during charge / discharge cycling, as the duration of charge / discharge cycling measurements depends on the current, electrolyte volume and concentration. The current is fixed and is the product of the electrode surface area and the current density. The potential required to maintain the fixed current depends on the electrolyte concentration, electrolyte flowrate and the redox kinetics of the reaction at the electrode. Charge / discharge cycling measurements can take a long time to perform, particularly at low current densities. If there are a large number of different carbon felts or pre-treatments that require testing, this is a real challenge.

As previously mentioned, changes in SOC result in changes to the standard reduction potential as defined by the Nernst equation. Whilst it is expected that the changes in E^{std} during charging and discharging will cancel each other out, this will not occur if the concentration at the potential limits are different for the charging and discharging cycles. If the potential limit is set too high, the graphite electrode will be oxidised during charging and water splitting will occur. Both of these unwanted side reactions result in unreliable data, as oxidising the electrode is a form of surface modification that will influence the kinetics of the reaction at the surface, whilst water splitting will reduce the coulombic efficiency. If the water splitting current is high, gas bubbles will form and depending on the local flow conditions, these bubbles may remain trapped inside the felt. Trapped bubbles will reduce the surface area available for electrocatalytic reactions, increasing the overpotential and reducing the voltage efficiency.

During discharging it is assumed there are no side reactions, this is a reasonable assumption as during discharging the potential at the positive will be insufficient thermodynamically to split water. The applied potential at the negative electrode will be less than 0.26 V below the standard reduction potential for the hydrogen evolution reaction, an insignificant amount of hydrogen should be formed at the negative electrode during discharging.

Vanadium crossover through the ion exchange membrane during charge / discharge cycling can influence the coulombic and hence energy efficiency of the cell. V^{3+} ions have the highest transference number and hence are likely to have the highest rate of cross-over through the membrane, whilst VO_2^+ ions have the lowest [225]. When the vanadium ions cross over during the discharging step, the coulombic efficiency is reduced. This is because the applied potential at the positive electrode will oxidise the V^{2+} and V^{3+} ions that cross over from the negative electrolyte, whilst at the negative electrode the applied potential will reduce the VO_2^+ and VO^{2+} ions that cross over from the positive electrolyte. This reduces the coulombic efficiency, as during discharging the dominant reaction at the positive electrode is the reduction of VO_2^+ to VO^{2+} and at the negative electrode it is the oxidation of V^{2+} to V^{3+}.

Many studies have investigated the performance of VRFB cells using charge / discharge cycling, with varying experimental parameters and efficiency results, (Table 8.1).

Table 8.1: Non-exhaustive selection of full cell measurement conditions and efficiency results. Other important parameters not shown include operating temperature, whether the electrolyte is recirculated and the duration of the experiments.

Ref	Elect. Thick.	Electrode Treatment	Area	[V]/ $[H_2SO_4]$	S.O.C	Flow	Mem.	E_{lim}	i	VE	CE	EE
	mm		cm^2	M	%	mL min^{-1}		(V)	mA cm^{-2}	%	%	%
[226]	6	400°C Air 6 hrs	10	1/4	100/0	None	N117	0.8 - 1.7	40	87.1	-	-
[226]	6	None	10	1/4	100/0	None	N117	0.8 - 1.7	40	60.3	-	-
[227]	4.6	None	31	1.6/4	50/50	100	N117	0.7 - 1.8	90	72.4	96.1	69.5
[227]	4.6	None	31	1.6/4	50/50	100	N117	0.7 – 1.8	435	28.1	96.7	27.1
[221]	0.3	1300°C 4:1 N_2:CO_2 1 hr	12	1.5/3	100/0	20	N115	0.9 – 1.65	60	92.6	93	86
[221]	0.3	None	12	1.5/3	100/0	20	N115	0.9 – 1.65	140	69	95	66
[222]	6	400°C Air 6 hrs	10	1.4/2	100/0	100	SFPAE 28 um	0.7-1.7	20	96	94	90
[222]	6	400°C Air 6 hrs	10	1.4/2	100/0	100	SFPAE 28 um	0.7-1.7	80	83	97.9	81
[228]	6	400°C Air 6 hrs	10	1/ 2.5	100/0	100	AEM 56 um	0.7 - 1.7	20	91	100	91
[228]	6	400°C Air 6 hrs	10	1/ 2.5	100/0	100	N212 51 um	0.7 - 1.7	80	71	94	66.7

8.1.6. Half-Cell Measurements

Half-cell measurements enable the contribution to the overpotential from the positive and negative electrodes to be calculated independently of each other. This is important for identifying whether electrode modifications improve the kinetics for both redox couples. Half-cell measurements have been recorded using a number of different cell set-ups, Schweiss *et al.* used a double-half cell design, whereby the same electrolyte was used at 50% SOC for both the positive and negative electrode. For the V^{2+} / V^{3+} couple, this means V^{2+} is oxidised at the positive electrode and V^{3+} is oxidised at the negative electrode. By drawing the electrolytes from the same tank the SOC should be maintained at 50%, provided there is not a large imbalance in the charge transferred to side reactions between the negative and positive electrode [229]. Fetyan *et al.* used a full cell, but with reference electrodes in each half cell to measure the potential of each half-cell reaction [230].

If a half-cell is used for polarization measurements, the apparent rate constant can be calculated from the current density, overpotential and geometric surface area of the electrode by rearranging Eq. 2.9:

$$k^0 = \frac{i}{FA\left(C_{Red}e^{\frac{-\alpha nF(E-E_{rev})}{RT}} - C_{Ox}e^{\frac{(1-\alpha)nF(E-E_{rev})}{RT}}\right)} \tag{2.9}$$

Where i, is the current, A, is the surface area of the electrode, k^0, is the standard rate constant, C_{Red}, is the concentration of the reduced species at the surface of the electrode, C_{Ox}, is the concentration of the oxidised species at the surface of the electrode, R, is the universal gas constant, T, is the temperature of the system in K. This Equation is only valid if the concentration of the oxidised and reduced species at the surface do not change. This is conditional upon having sufficient electrolyte flow to limit concentration polarization at the electrode surface and therefore calculated apparent rate constant values should be considered estimates.

8.2. Experimental

In this work measurements for the positive electrolyte were carried out using a half-cell, where the working electrode felt samples (3.14 cm^2 cross-sectional area) were separated from a supporting electrolyte chamber by a Nafion N1110 membrane. The positive electrode potential was recorded relative to a saturated KCl Ag|AgCl reference electrode, with a large graphite plate used as the counter electrode, (Figure 8.1). Polarization curve and charge / discharge measurements were recorded for GFE, C100 and G100 untreated and thermally treated felts, to calculate the apparent rate constant and half-cell efficiency.

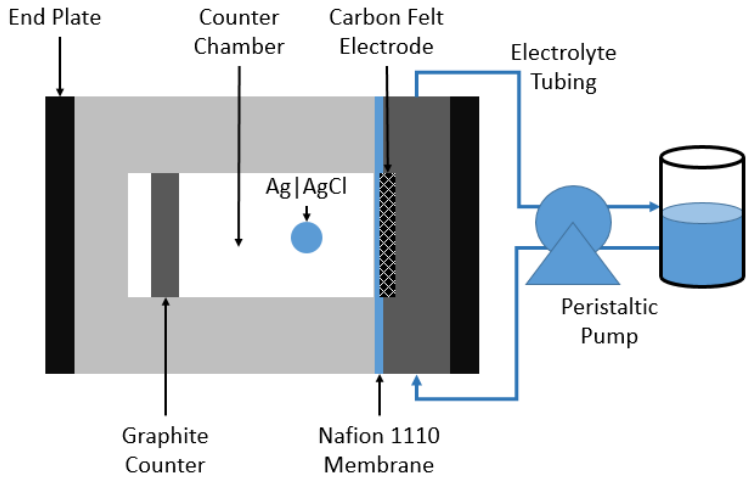

Figure 8.1: Custom half-cell design enabling analysis of single redox couples at 50% SOC.

Half-cell polarization measurements were used to identify the kinetic performance of different felts and isolate the onset of mass transport resistance. Using an electrolyte at 100% SOC would only allow for the measurement of the reduction reaction, thus not fully characterizing the system. Hence, polarization curve measurements were recorded at 50% SOC for the positive electrolyte. The electrolyte was prepared by dissolving 0.4 M $VOSO_4$ (Alfa Aesar) and 0.2 M V_2O_5 (Alfa Aesar) in 3 M H_2SO_4, to give a solution at 50% SOC with 0.4 M VO^{2+} and 0.4 M VO_2^+. The counter chamber contained the same solution as the working side to minimise cross-over of vanadium ions. Different current densities ranging from 5 to 500 mA cm^{-2} were applied using a Gamry 3000 potentiostat, with the average potential reported over last 25 s of each 30 s step. The first 5 s were ignored to limit the contribution of capacitance.

To maintain the SOC at 50% during the polarization curve measurements each charging current density measurement was followed by a discharging measurement at the same current density. Based on the planned current density, the total charge transferred for charging and discharging of each felt sample will be 279 coulombs. If the coulombic efficiency was 90%, the complete measurement for each cell set up would lead to an imbalance of 28 coulombs, equivalent to the conversion of 0.00029 moles of VO_2^+ to VO^{2+}. Given the electrolyte volume of 50 mL and the concentration of each vanadium ion is 0.4 M, each felt sample measurement will change the total concentration by less than 1.4%, thus the initial 0.4 M VO_2^+ concentration may become 0.494 M. This imbalance is mostly influenced by the higher current measurements, as at low current densities the total charge passed is smaller and the coulombic efficiency should be close to 100% due to the smaller overpotential during charging.

EIS measurements were recorded with a 5 mV rms AC perturbation, within a frequency range of 200 kHz to 100 Hz. The resistance value from the EIS recorded before the polarization measurements was used for IR correction, as the higher current measurements were carried out first and are the most sensitive to changes in resistance (which can occur due to ion cross-over or changes to the carbon felt over time).

Charge / discharge measurements were recorded using the same half-cell set up used for the polarization curve measurements. Charge / discharge curves were recorded at 100 mA cm^{-2}, with upper and lower voltage cut-off limits of 1.15 V and 0.55 V vs the Ag|AgCl reference electrode. The electrical resistance was corrected for post run using the resistance value recorded at 0 ^{o} phase angle, from EIS measurements made before each charging and discharging step.

8.3. Results and Discussion

The electrolyte flowrate is an important parameter for the cell efficiency and power output, as a higher flowrate reduces the mass transport overpotential. In this work the polarization curve was recorded at a range of flowrates with a GFE felt thermally treated at 300 ºC for one hour as the working electrode, (Figure 8.2).

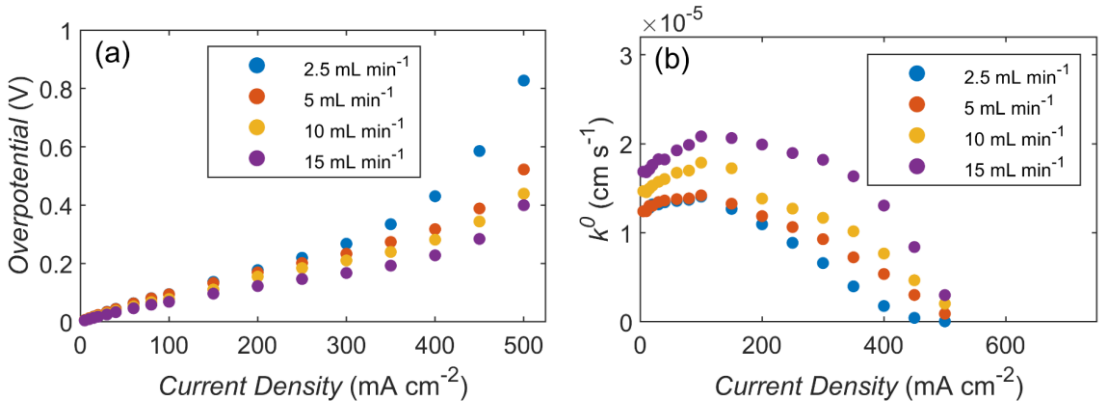

Figure 8.2: a) Polarization curve for different electrolyte flow rates through the felt. b) Apparent rate constant calculated form the electrode overpotential.

In Figure 8.2 a, the polarization curve data demonstrates that increasing the flowrate reduces the required overpotential for each current density. Additionally, the overpotential increases significantly after around 150 mA cm^{-2}, particularly at the lower flowrates and is likely the result of mass transfer resistance. The apparent rate constants calculated form the overpotentials are shown in Figure 8.2 b, as expected the calculated apparent rate constants decrease above 150 mA cm^{-2}. This is not because the rate constant has changed, but rather the concentration of the reactant at the surface begins to reduce, due to mass transport limitations.

Interestingly the calculated rate constant is larger at the higher flowrates, this could be the result of improved wetting of the felt by forcing the electrolyte through at a faster rate. Based on these results, 15 mL min^{-1} was selected as the most suitable flowrate for future measurements, to accurately identify differences in kinetics at different felts.

Polarization curve measurements were recorded at 15 mL min^{-1} for untreated and thermally treated GFE, G100 and C100 felts, (Figure 8.3).

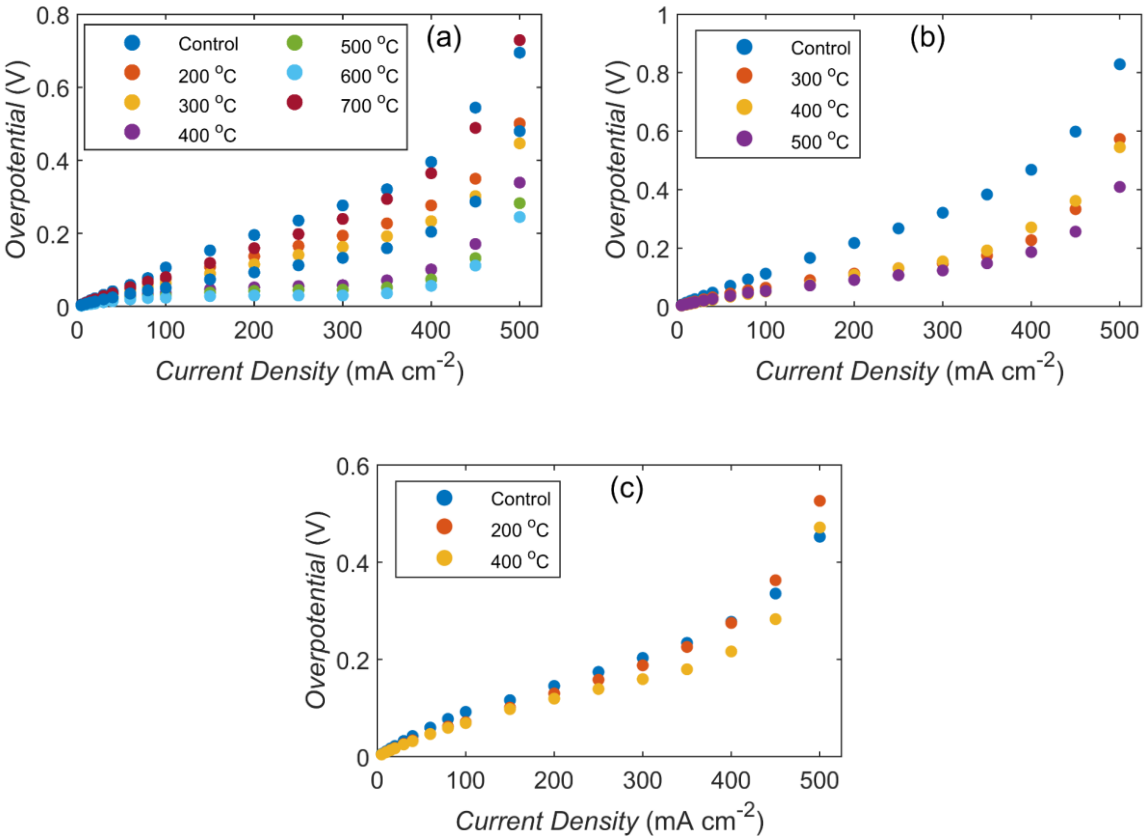

Figure 8.3: Polarization curves for each felt and thermal treatment, recorded in 0.4 M V^{4+} and 0.4 M V^{5+} dissolved in 3 M H_2SO_4. a) GFE felt samples, b) G100 felt samples and c) C100 felt samples.

As expected the thermally treated GFE and G100 felts showed a clear reduction in overpotential, consistent with the trend in rate constants calculated in Chapter 7. Little change was observed for the thermally treated C100 felts, further supporting the accuracy of the apparent rate constants calculated from cyclic voltammetry in Chapter 7.

The apparent rate constant for each felt is reported as the average of the apparent rate constants calculated from the current densities of 100 mA cm^{-2} or less, (Figure 8.4). This current density range was chosen to reduce the influence of mass transport limitations, which occur at the higher current densities.

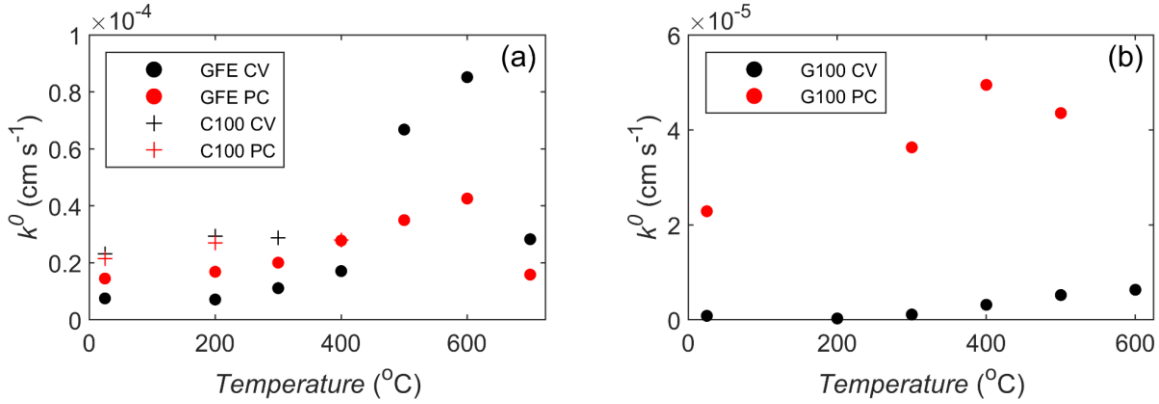

Figure 8.4: Apparent rate constant comparison between values calculated from cyclic voltammetry and polarization curves. a) GFE and C100 felt samples, b) G100 felt samples. Apparent rate constants calculated using Equation 2.

The rate constants calculated from polarization curve data for the GFE and C100 felts, thermally treated and untreated are in excellent agreement with the previously reported values calculated from cyclic voltammetry reported in Chapter 7. This confirms that the analysis of the cyclic voltammetry data using the assumed void distribution modelling was accurate. However, there was a noticeable increase in the calculated rate constant for G100 from polarization curve measurements relative to those from cyclic voltammetry. G100 clearly had much larger peak separation during cyclic voltammetry than the GFE and C100, therefore the difference in measurement methods is likely responsible for the different in the recorded apparent rate constant. The higher rate constants recorded during polarization curve measurements in the half-cell can be explained by improved wetting, which may due to use of the peristaltic pump.

8.3.1. Charge / Discharge Measurements

Charge / discharge measurements were carried out determine if the rate constants calculated from cyclic voltammetry and polarization curves accurately reflect the performance of the carbon felt when used in a working cell. As previously mentioned the voltage drop from electrical resistance was corrected for post run. In a full-cell, the electrical resistance is not typically corrected for, as the change in resistance can be due to the conductivity of the felt. However, in this half-cell set up changes in resistance are more likely due to changes in solution resistance from the distance of the reference electrode to the working electrode. The voltage efficiency (VE), coulombic efficiency (CE) and energy efficiency (EE) were calculated using Eqs. 2.5-2.7 and are presented, (Table 8.2).

Table 8.2: Performance characteristics for selected carbon felt samples.

Felt	**VE**	**CE**	**EE**	$\mathbf{k^0_{app}}$
	(%)	(%)	(%)	(cm s^{-1})
GFE	81.9	93.8	76.8	1.4×10^{-5}
G100	82.8	97.9	81.1	2.3×10^{-5}
C100	87.1	98.2	85.5	2.2×10^{-5}
GFE Thermal	89.1	98.5	87.7	4.3×10^{-5}

As expected based on the rate constant calculated from polarization curve measurements, the GFE Control felt sample had the lowest efficiency of the three felts (GFE, C100, G100). Whilst the GFE felt sample thermally treated at 600 ^{o}C showed a noticeable improvement in performance over the untreated felt, increasing energy efficiency from 76.8% to 87.7%.

Based on the apparent rate constants the G100 felt should have a slightly higher efficiency than the C100 felt. However, the apparent rate constants were calculated from the geometric surface area of the different felts, based on the sample weight and average fiber diameter. C100 was found to have 25% more area than the G100 felt sample, hence the C100 felt showed higher efficiency.

The calculated efficiency values in this work should not be used to identify full-cell performance, as the negative cell is often cited as having slower kinetics and being more prone to unwanted side reactions, specifically the hydrogen evolution reaction. Additionally, the vanadium electrolyte concentration in this work was 0.8 M, which is half of what would be used in an operational battery. Therefore, the overpotentials measured here will be higher than in a commercial battery for the positive redox couple.

The results however do confirm that polarization curve measurements are an accurate way to calculate the kinetic performance of different felts. Polarization curve measurements can significantly reduce the time needed to analyse the performance of different electrode treatments, which will be helpful in future experimentation. Another advantage of polarization curve measurements is that they provide a good understanding of when mass transport losses become significant during cell operation. Ultimately, polarization curve measurements should also be carried out using the negative electrolyte, with comparison to the efficiency of a full-cell from charge / discharge measurements, to gain a fuller understanding of the VRFB cell operation.

8.4. Conclusions

Polarization curve and charge / discharge cycling measurements for a range of untreated and thermally treated felts were recorded in a half-cell set up. It was found that at low current densities, the apparent rate constant for felt samples could be accurately recorded. The apparent rate constants calculated from polarization curve measurements were in close agreement to those calculated previously from cyclic voltammetry for GFE and C100 felts. The apparent rate constants calculated for G100 felt samples from polarization curve measurements were significantly higher than what was calculated from cyclic voltammetry. This discrepancy is likely due to improved wetting in the half-cell. Charge / discharge cycling measurements were carried out to calculate the voltage, coulombic and energy efficiency for the positive VRFB reaction. The resulting energy efficiency values were consistent with the apparent rate constant values calculated from polarization curve measurements. With the GFE felt thermally treated at 600 ^{o}C having the highest rate constant of $k_{app}^{0} = 4.3 \times 10^{-5}$ cm s^{-1} and an energy efficiency of 87.7% for charge / discharge curve measurements recorded at 100 mA cm^{-2}.

9. Conclusions and Recommendations

Vanadium redox flow batteries are a viable form of long duration energy storage. However, the high capital cost reduces the economic incentive to install large quantities of vanadium redox flow batteries. Cost reductions could come from improving the kinetic performance of the carbon felt electrodes, typically used in vanadium redox flow battery cell stacks. Unfortunately, the quantification of electron transfer kinetics at carbon felt electrodes is difficult due to the complex mass transport behaviour within the randomly ordered felt electrodes.

9.1. Experimental conclusions

In this work we have used cylindrical single carbon fibre electrodes to simplify the geometry, enabling accurate calculation of electrode kinetics, by modelling the response of the electrodes to cyclic voltammetry and electrochemical impedance spectroscopy. Analysis of the kinetics for the $Fe(CN)_6^{3-}$ / $Fe(CN)_6^{4-}$ redox couple at single carbon fibre electrodes showed that there was a distribution of rate constants within the felt. However, the carbon felt electrodes are a randomly ordered array of individual carbon fibers, thus in order to model the behaviour at a felt electrode the void size distribution of the felt is required. In this work the felt void size distribution was characterised by analysing micro-CT images of the felt. When the void size distribution and the rate constant distribution were considered together, it was shown that accurate simulation of cyclic voltammetry at the carbon felt electrode was possible over a wide range of sweep rates.

Thermal treatment of four different carbon fibers was carried out to further understand the kinetics of $Fe(CN)_6^{3-} / Fe(CN)_6^{4-}$ at the carbon fiber surface. The apparent rate constant was calculated for thermally treated and untreated carbon fiber samples, using the previously validated methods for the simulation of cyclic voltammetry and electrochemical impedance spectroscopy. The capacitance of the carbon fibers was calculated from cyclic voltammetry and can be considered a proxy for the electrochemically active surface area. The apparent rate constant was found to increase more significantly than the capacitance at three of the four fibers tested, whilst the final fiber had only a modest increase in the apparent rate constant. This result strongly suggests that the kinetics for the reaction depend on different functional groups at the surface, as well as the electrochemically active surface area.

Whilst thermal treatment improved the apparent rate constant for the $Fe(CN)_6^{3-} / Fe(CN)_6^{4-}$ redox couple, the redox couples of most interest form a commercial perspective are the V^{2+} / V^{3+} and VO^{2+} / VO_2^{+}. Cyclic voltammetry of the vanadium redox couples at single fiber electrodes is difficult, as the water splitting and hydrogen evolution side reactions will complicate the measurement of the voltammograms. However, due to the small voids within carbon felt electrodes, the positive redox couple can be analysed through cyclic voltammetry, as the reactant concentration in the small voids within the felt depletes quickly, reducing the peak potential separation relative to single fiber electrodes. Using the previously calculated void size distribution, an apparent rate constant was calculated for felt samples of three different carbon felts, thermally treated for 1 hour at 100 °C increments from 200 °C to 700 °C. Thermal treatment primarily improved the apparent rate constant at the different carbon felts.

As with the $Fe(CN)_6^{3-}$ / $Fe(CN)_6^{4-}$ redox couple, the increase in kinetics was not directly related to increased capacitance. The change in physical area of the felts at a selected treatment temperature was also recorded with BET measurements. It was found that the increase in capacitance was broadly related to the increased physical area of the electrodes, however there was also a change in the specific capacitance. The specific capacitance for carbon surfaces is known to be related to the ratio of basal to edge plane sites. In this work the recorded specific capacitances of the different thermally treated felts were within the expected range for carbon materials. Raman spectroscopy analysis supported the changes in specific capacitance, with the least ordered felt showing the highest change in capacitance, as would be expected.

Half-cell measurements of the VO^{2+} / VO_2^+ redox couple were recorded using polarization curve and charge / discharge curve analysis. The apparent rate constants calculated from the overpotential during polarization curve measurements were in close agreement with those calculated from the simulation of cyclic voltammetry. This supports the accuracy of using cyclic voltammetry to identify the kinetic performance of carbon felts, provided the void distribution is accounted for. Charge / discharge measurements confirmed that felts with higher apparent rate constants had higher performance, with improved energy efficiency.

9.2. Recommendations for Future Work

The electrochemical performance of single carbon fiber electrodes and carbon felts has been accurately analysed using electrochemical impedance spectroscopy, cyclic voltammetry and polarization curve measurements for the $Fe(CN)_6^{3-}$ / $Fe(CN)_6^{4-}$ and VO^{2+} / VO_2^{+} redox couples. However, this primarily serves as a proof of concept, as the V^{2+} / V^{3+} redox reaction is considered to be the performance limiting reaction for the vanadium redox flow battery. In this work we selected the VO^{2+} / VO_2^{+} redox couple to avoid large current contributions from side reactions during electrochemical measurements, simplifying the analysis. Future work should be focused on applying the analytical methods developed in this work to the V^{2+} / V^{3+} redox reaction, with attention given to improving the kinetics of the vanadium reaction, whilst inhibiting the hydrogen evolution reaction to improve coulombic efficiency. Once this is understood, full cell measurements should be recorded using the same procedures as in literature, to enable direct comparison of the performance.

In current literature the importance of different functional groups is often discussed, however the identification of the most effective functional groups has likely been held back by the difficulties involved in calculating the inherent rate constant. Using the improved understanding of the inherent kinetics developed in this work, it should be possible to identify with greater confidence the contribution to battery performance from electrode wettability, surface roughness, inherent kinetics and conductivity. If this is achieved, more targeted electrode modifications can be designed, with the aim of improving the energy efficiency of the cell when operated at industrially relevant current densities.

10. References

1. International Energy Agency, *Renewables 2018*. 2018. p. 3-4.
2. Helm, C. and M. Mier, *On the efficient market diffusion of intermittent renewable energies.* Energy Economics, 2019. **80**: p. 812-830.
3. Committee for The National Academies Summit on America's Energy, F., *The National Academies summit on America's energy future: summary of a meeting*. 2008, Washington, D.C: National Academies Press.
4. Price, A., *Electrical energy storage-a review of technology options.* Proceedings of the Institution of Civil Engineers: Civil Engineering, 2005. **158**(6): p. 52-58.
5. Deane, J.P., B.P. Ó Gallachóir, and E.J. McKeogh, *Techno-economic review of existing and new pumped hydro energy storage plant.* Renewable and Sustainable Energy Reviews, 2010. **14**(4): p. 1293-1302.
6. Transpower. *Hydro Risk Curves*. 2017 [cited 2017 28/9]; Available from: https://www.transpower.co.nz/system-operator/security-supply/hydro-risk-curves.
7. Ministry of Business and Innovation, *Data tables for electricity*. 2020.
8. International Energy Agency. *Hydropower*. 2017 [cited 2017 28/9]; Available from: https://www.iea.org/topics/renewables/hydropower/.
9. Budt, M., et al., *A review on compressed air energy storage: Basic principles, past milestones and recent developments.* Applied Energy, 2016. **170**: p. 250.
10. Pollet, B.G., I. Staffell, and J.L. Shang, *Current status of hybrid, battery and fuel cell electric vehicles: From electrochemistry to market prospects.* Electrochimica Acta, 2012. **84**: p. 235-249.
11. Colthorpe, A. *Lithium-ion predicted to dominate even in 'longer duration' global market*. 2017 [cited 2017 28/9]; Available from: https://www.energy-storage.news/news/lithium-ion-to-dominate-even-in-longer-duration-global-market-says-i.h.s-ma.
12. Ulaganathan, M., et al., *Recent Advancements in All-Vanadium Redox Flow Batteries.* Advanced Materials Interfaces, 2016. **3**(1): p. 1500309-n/a.

13. Chu, S., Y. Cui, and N. Liu, *The path towards sustainable energy.* Nature materials, 2017. **16**(1): p. 16-22.
14. Amrouche, S.O., et al., *Overview of energy storage in renewable energy systems.* International Journal of Hydrogen Energy, 2016. **41**(45): p. 20914-20927.
15. Arbabzadeh, M., et al., *Vanadium redox flow batteries to reach greenhouse gas emissions targets in an off-grid configuration.* Applied Energy, 2015. **146**: p. 397-408.
16. Kim, K.J., et al., *Superior Electrocatalytic Activity of a Robust Carbon-Felt Electrode with Oxygen-Rich Phosphate Groups for All-Vanadium Redox Flow Batteries.* ChemSusChem, 2016. **9**(11): p. 1329-1338.
17. Alotto, P., M. Guarnieri, and F. Moro, *Redox flow batteries for the storage of renewable energy: A review.* Renewable and Sustainable Energy Reviews, 2014. **29**: p. 325-335.
18. International Electrotechnical Commission, *Electrical Energy Storage*. 2012. p. 31.
19. Yang, B., et al., *High-Performance Aqueous Organic Flow Battery with Quinone-Based Redox Couples at Both Electrodes.* Journal of the Electrochemical Society, 2016. **163**(7): p. A1442-A1449.
20. Minke, C. and T. Turek, *Economics of vanadium redox flow battery membranes.* Journal of Power Sources, 2015. **286**: p. 247-257.
21. Aaron, D., et al., *Kinetic enhancement via passive deposition of carbon-based nanomaterials in vanadium redox flow batteries.* Journal of Power Sources, 2017. **366**: p. 241-248.
22. Page, S. and S. Krumdieck, *System-level energy efficiency is the greatest barrier to development of the hydrogen economy.* Energy Policy, 2009. **37**(9): p. 3325-3335.
23. Pilatowsky, I., et al., *Cogeneration Fuel Cell - Sorption Air Conditioning Systems*. Vol. 12. 2011. Chapter 2.
24. Luo, X., et al., *Overview of current development in electrical energy storage technologies and the application potential in power system operation.* Applied Energy, 2015. **137**: p. 511-536.
25. Julch, V., *Comparison of electricity storage options using levelized cost of storage (LCOS) method.* Applied Energy, 2016. **183**: p. 1594-1606.

26. Lazard. *Lazard's Levelized Cost of Storage*. 2017 [cited 2017 21/9]; Available from: https://www.lazard.com/media/450338/lazard-levelized-cost-of-storage-version-30.pdf.
27. International Energy Agency. *Tracking Progress: Energy storage*. 2017 [cited 2017 29/9]; Available from: https://www.iea.org/etp/tracking2017/energystorage/.
28. Transpower, *Battery Storage in New Zealand*. 2017.
29. Cunha, Á., et al., *Vanadium redox flow batteries: a technology review.* International Journal of Energy Research, 2015. **39**(7): p. 889-918.
30. Skyllas-Kazacos, M., et al., *Progress in Flow Battery Research and Development.* Journal of the Electrochemical Society, 2011. **158**(8): p. R55-R79.
31. Tomazic, G. and M. Skyllas-Kazacos, *Chapter 17 - Redox Flow Batteries*, in *Electrochemical Energy Storage for Renewable Sources and Grid Balancing*, P.T. Moseley and J. Garche, Editors. 2015, Elsevier: Amsterdam. p. 309-336.
32. Kear, G., A.A. Shah, and F.C. Walsh, *Development of the all-vanadium redox flow battery for energy storage: a review of technological, financial and policy aspects.* International Journal of Energy Research, 2012. **36**(11): p. 1105-1120.
33. Guarnieri, M., et al., *Vanadium Redox Flow Batteries: Potentials and Challenges of an Emerging Storage Technology*. IEEE Industrial Electronics Magazine, 2016. **10**(4): p. 20-31.
34. Ravikumar, M., et al., *The renaissance in redox flow batteries.* Journal of Solid State Electrochemistry, 2017. **21**(9): p. 2467-2488.
35. Weber, A.Z., et al., *Redox flow batteries: a review.* Journal of Applied Electrochemistry, 2011. **41**(10): p. 1137-1164.
36. Shigematsu, T., *Redox flow battery for energy storage.* SEI technical review, 2011. **73**(7): p. 13.
37. Skyllas-Kazacos, M., et al., *Recent advances with UNSW vanadium-based redox flow batteries.* International Journal of Energy Research, 2010. **34**(2): p. 182-189.
38. Fabjan, C., et al., *The vanadium redox-battery: an efficient storage unit for photovoltaic systems.* Electrochimica Acta, 2001. **47**(5): p. 825-831.

39. Liu, J., et al., *Aqueous Rechargeable Batteries for Large-scale Energy Storage.* Israel Journal of Chemistry, 2015. **55**(5): p. 521-536.
40. Wu, X., et al., *Electrolytes for vanadium redox flow batteries.* Pure and Applied Chemistry, 2014. **86**(5): p. 661-669.
41. Soloveichik, G.L., *Flow Batteries: Current Status and Trends.* CHEMICAL REVIEWS, 2015. **115**(20): p. 11533-11558.
42. Leung, P., et al., *Progress in redox flow batteries, remaining challenges and their applications in energy storage.* Rsc Advances, 2012. **2**(27): p. 10125-10156.
43. Skyllas-Kazacos, M., et al., *Vanadium electrolyte studies for the vanadium redox battery—a review.* ChemSusChem, 2016. **9**(13): p. 1521-1543.
44. Ding, C., et al., *Vanadium flow battery for energy storage: prospects and challenges.* The journal of physical chemistry letters, 2013. **4**(8): p. 1281-1294.
45. Liu, J., et al., *Materials science and materials chemistry for large scale electrochemical energy storage: from transportation to electrical grid.* Advanced Functional Materials, 2013. **23**(8): p. 929-946.
46. Parasuraman, A., et al., *Review of material research and development for vanadium redox flow battery applications.* Electrochimica Acta, 2013. **101**: p. 27-40.
47. Chakrabarti, M.H., et al., *Redox flow battery for energy storage.* Arabian Journal for Science and Engineering, 2013. **38**(4): p. 723-739.
48. Kim, K.J., et al., *A technology review of electrodes and reaction mechanisms in vanadium redox flow batteries.* Journal of Materials Chemistry, 2015. **3**(33): p. 16913-16933.
49. Wei, G.-j., et al., *A review of the electrochemical activity of carbon materials in vanadium redox flow batteries.* Carbon, 2015. **81**: p. 850.
50. Minke, C. and T. Turek, *Materials, system designs and modelling approaches in techno-economic assessment of all-vanadium redox flow batteries – A review.* Journal of power sources, 2018. **376**: p. 66-81.
51. Yuan, X.Z., et al., *A review of all-vanadium redox flow battery durability: Degradation mechanisms and mitigation strategies.* International journal of energy research, 2019. **43**(13): p. 6599-6638.

52. Shi, Y., et al., *Recent development of membrane for vanadium redox flow battery applications: A review.* Applied energy, 2019. **238**: p. 202-224.
53. Lourenssen, K., et al., *Vanadium redox flow batteries: A comprehensive review.* Journal of energy storage, 2019. **25**: p. 100844.
54. Perry, M.L., R.M. Darling, and R. Zaffou. *High power density redox flow battery cells*. 2013.
55. Daintith, J., *Oxford Dictionary of Chemistry*. 6th ed. 2008.
56. Knehr, K.W. and E.C. Kumbur, *Open circuit voltage of vanadium redox flow batteries: Discrepancy between models and experiments.* Electrochemistry Communications, 2011. **13**(4): p. 342-345.
57. Shah, A.A., et al., *A dynamic unit cell model for the all-vanadium flow battery.* Journal of the Electrochemical Society, 2011. **158**(6): p. A671-A677.
58. Zoski, C.G., *Handbook of electrochemistry*. 1st ed. 2007, Amsterdam;Boston;: Elsevier.
59. Sutherland, W., *LXXV. A dynamical theory of diffusion for non-electrolytes and the molecular mass of albumin.* The London, Edinburgh, and Dublin Philosophical Magazine and Journal of Science, 1905. **9**(54): p. 781-785.
60. University of Cambridge Department of Chemical Engineering and Biotechnology. *Mass Transport*. 2020 [cited 2017 17/07/20120]; Available from: https://www.ceb.cam.ac.uk/research/groups/rg-eme/Edu/mass-transport.
61. Tang, A., J. Bao, and M. Skyllas-Kazacos, *Studies on pressure losses and flow rate optimization in vanadium redox flow battery.* Journal of power sources, 2014. **248**: p. 154-162.
62. Holland-Cunz, M.V., J. Friedl, and U. Stimming, *Anion effects on the redox kinetics of positive electrolyte of the all-vanadium redox flow battery.* Journal of Electroanalytical Chemistry, 2018. **819**: p. 306-311.
63. Chin-Lung, H., et al., *Effect of Compression Ratio of Graphite Felts on the Performance of an All-Vanadium Redox Flow Battery.* Energies, 2019. **12**(2).

64. Brown, L.D., et al., *The effect of felt compression on the performance and pressure drop of all-vanadium redox flow batteries.* Journal of Energy Storage, 2016. **8**: p. 91-98.
65. Hsieh, S.-S., H.-C. Wu, and B.-S. Her, *A novel design for a flow field configuration, of a direct methanol fuel cell.* Journal of Power Sources, 2010. **195**(10): p. 3224-3230.
66. Arvay, A., et al., *Nature inspired flow field designs for proton exchange membrane fuel cell.* International Journal of Hydrogen Energy, 2013. **38**(9): p. 3717-3726.
67. Li, X. and I. Sabir, *Review of bipolar plates in PEM fuel cells: Flow-field designs.* International Journal of Hydrogen Energy, 2005. **30**(4): p. 359-371.
68. Srouji, A.K., et al., *Ultra-high current density water management in polymer electrolyte fuel cell with porous metallic flow field.* Journal of Power Sources, 2013. **239**: p. 433-442.
69. Cho, K.T. and M.M. Mench, *Coupled effects of flow field geometry and diffusion media material structure on evaporative water removal from polymer electrolyte fuel cells.* International Journal of Hydrogen Energy, 2010. **35**(22): p. 12329-12340.
70. Kumbur, E.C., K.V. Sharp, and M.M. Mench, *Liquid droplet behavior and instability in a polymer electrolyte fuel cell flow channel.* Journal of Power Sources, 2006. **161**(1): p. 333-345.
71. Yoon, S.Y., et al., *Gas-phase particle image velocimetry (PIV) for application to the design of fuel cell reactant flow channels.* Journal of Power Sources, 2006. **160**(2): p. 1017-1025.
72. Turhan, A., et al., *Passive control of liquid water storage and distribution in a PEFC through flow-field design.* Journal of Power Sources, 2008. **180**(2): p. 773-783.
73. Sun, C.-N., et al., *Probing electrode losses in all-vanadium redox flow batteries with impedance spectroscopy.* ECS Electrochemistry Letters, 2013. **2**(5): p. A43-A45.
74. Liu, Q., et al., *In situ potential distribution measurement in an all-vanadium flow battery.* Chemical Communications, 2013. **49**(56): p. 6292-6294.
75. Houser, J., et al., *Influence of architecture and material properties on vanadium redox flow battery performance.* Journal of Power Sources, 2016. **302**: p. 369-377.

76. Xu, Q., T.S. Zhao, and C. Zhang, *Performance of a vanadium redox flow battery with and without flow fields.* Electrochimica Acta, 2014. **142**: p. 61-67.
77. Darling, R.M. and M.L. Perry, *The Influence of Electrode and Channel Configurations on Flow Battery Performance.* Journal of the Electrochemical Society, 2014. **161**(9): p. A1381-A1387.
78. Gundlapalli, R. and S. Jayanti, *Performance characteristics of several variants of interdigitated flow fields for flow battery applications.* Journal of Power Sources, 2020. **467**: p. 228225.
79. Gurieff, N., et al., *Mass Transport Optimization for Redox Flow Battery Design.* Applied Sciences, 2020. **10**(8): p. 2801.
80. Viswanathan, V., et al., *Cost and performance model for redox flow batteries.* Journal of Power Sources, 2014. **247**: p. 1040-1051.
81. Mohamed, M.R., S.M. Sharkh, and F.C. Walsh. *Redox flow batteries for hybrid electric vehicles: Progress and challenges*. 2009.
82. Dennison, C.R., et al., *Enhancing Mass Transport in Redox Flow Batteries by Tailoring Flow Field and Electrode Design.* Journal of the Electrochemical Society, 2016. **163**(1): p. A5163-A5169.
83. Ke, X., et al., *Rechargeable redox flow batteries: Maximum current density with electrolyte flow reactant penetration in a serpentine flow structure.* 2017.
84. Xu, Q. and T.S. Zhao, *Determination of the mass-transport properties of vanadium ions through the porous electrodes of vanadium redox flow batteries.* Physical Chemistry Chemical Physics, 2013. **15**(26): p. 1841-1848.
85. Pezeshki, A.M., et al., *High performance electrodes in vanadium redox flow batteries through oxygen-enriched thermal activation.* Journal of Power Sources, 2015. **294**: p. 333-338.
86. Prifti, H., et al., *Membranes for Redox Flow Battery Applications.* Membranes, 2012. **2**(2): p. 275.
87. Zhou, X.L., et al., *Performance of a vanadium redox flow battery with a VANADion membrane.* APPLIED ENERGY, 2016. **180**: p. 353-359.

88. Stimming, U., J. Wang, and A. Bund, *The Vanadium Redox Reactions – Electrocatalysis versus Non-Electrocatalysis.* Chemphyschem, 2019. **20**(22): p. 3004-3009.

89. Chen, P., M.A. Fryling, and R.L. McCreery, *Electron Transfer Kinetics at Modified Carbon Electrode Surfaces: The Role of Specific Surface Sites.* Analytical Chemistry, 1995. **67**(18): p. 3115-3122.

90. Goulet, M.-A., M. Skyllas-Kazacos, and E. Kjeang, *The importance of wetting in carbon paper electrodes for vanadium redox reactions.* Carbon, 2016. **101**: p. 390-398.

91. Zhang, W., et al., *Electrochemical activation of graphite felt electrode for VO^{2+}/VO_2^{+} redox couple application.* Electrochimica Acta, 2013. **89**: p. 429-435.

92. Schweiss, R., A. Pritzl, and C. Meiser, *Parasitic hydrogen evolution at different carbon fiber electrodes in vanadium redox flow batteries.* Journal of the Electrochemical Society, 2016. **163**(9): p. A2089.

93. Sun, C.-N., et al., *Hydrogen evolution at the negative electrode of the all-vanadium redox flow batteries.* Journal of Power Sources, 2014. **248**: p. 560-564.

94. Kokkinidis, G., *Underpotential deposition and electrocatalysis.* Journal of Electroanalytical Chemistry and Interfacial Electrochemistry, 1986. **201**(2): p. 217-236.

95. Trasatti, S., *Electrocatalysis of hydrogen evolution: progress in cathode activation.* Advances in electrochemical science and engineering, 1992. **2**: p. 1-85.

96. Ross Jr, P.N., *The science of electrocatalysis on bimetallic surfaces*. 1998: Wiley-VCH: New York.

97. Holze, R., *Underpotential deposit electrocatalysis of fast redox reactions for electrochemical energy storage systems.* Journal of Solid State Electrochemistry, 1998. **2**(2): p. 73-77.

98. Mehboob, S., et al., *Excellent electrocatalytic effects of tin through in situ electrodeposition on the performance of all-vanadium redox flow batteries.* Journal of Materials Chemistry A, 2017. **5**(33): p. 17388-17400.

99. Sun, B. and M. Skyllas-Kazakos, *Chemical modification and electrochemical behaviour of graphite fibre in acidic vanadium solution.* Electrochimica Acta, 1991. **36**(3): p. 513-517.

100. Xiang, Y. and W.A. Daoud, *Electrochemical enhancement of carbon paper by indium modification for the positive side of vanadium redox flow battery*. Journal of The Electrochemical Society, 2017. **164**(9): p. A2256.

101. Suárez, D.J., et al., *Graphite felt modified with bismuth nanoparticles as negative electrode in a vanadium redox flow battery.* ChemSusChem, 2014. **7**(3): p. 914-918.

102. Liu, T., et al., *Investigation on the effect of catalyst on the electrochemical performance of carbon felt and graphite felt for vanadium flow batteries.* Journal of Power Sources, 2015. **286**: p. 73-81.

103. González, Z., et al., *Enhanced performance of a Bi-modified graphite felt as the positive electrode of a vanadium redox flow battery.* Electrochemistry Communications, 2011. **13**(12): p. 1379-1382.

104. Li, B., et al., *Bismuth nanoparticle decorating graphite felt as a high-performance electrode for an all-vanadium redox flow battery.* Nano letters, 2013. **13**(3): p. 1330-1335.

105. Yang, X., et al., *The catalytic effect of bismuth for VO_2^+/VO^{2+} and V^{3+}/V^{2+} redox couples in vanadium flow batteries.* Journal of Energy Chemistry, 2017. **26**(1): p. 1-7.

106. Lv, Y., et al., *Enhanced electrochemical activity of carbon felt for V^{2+}/V^{3+} redox reaction via combining KOH-etched pretreatment with uniform deposition of Bi nanoparticles.* Electrochimica Acta, 2017. **253**: p. 78-84.

107. Shen, J., et al., *Influence of antimony ions in negative electrolyte on the electrochemical performance of vanadium redox flow batteries.* Electrochimica Acta, 2015. **151**: p. 297-305.

108. Flox, C., et al., *Active nano-CuPt3 electrocatalyst supported on graphene for enhancing reactions at the cathode in all-vanadium redox flow batteries.* Carbon, 2012. **50**(6): p. 2372-2374.

109. Flox, C., et al., *Strategies for enhancing electrochemical activity of carbon-based electrodes for all-vanadium redox flow batteries.* Applied energy, 2013. **109**: p. 344-351.

110. Wei, L., et al., *Copper nanoparticle-deposited graphite felt electrodes for all vanadium redox flow batteries.* Applied Energy, 2016. **180**: p. 386-391.

111. Han, P., et al., *RuSe/reduced graphene oxide: an efficient electrocatalyst for VO^{2+}/VO_2^{+} redox couples in vanadium redox flow batteries.* RSC advances, 2014. **4**(39): p. 20379-20381.

112. Al-Ahmed, A., *Electrode Modification for Better Kinetics in all Vanadium Redox Flow Battery (AVRFB): A Short Review.* Advanced Materials Research, 2015. **1116**: p. 229-235.

113. Khan, M.A., et al., *Recent Progresses in Electrocatalysts for Water Electrolysis.* Electrochemical Energy Reviews, 2018. **1**(4): p. 483-530.

114. Wang, W. and X. Wang, *Investigation of Ir-modified carbon felt as the positive electrode of an all-vanadium redox flow battery.* Electrochimica Acta, 2007. **52**(24): p. 6755-6762.

115. Wu, X., et al., *PbO2-modified graphite felt as the positive electrode for an all-vanadium redox flow battery.* Journal of Power Sources, 2014. **250**: p. 274-278.

116. Faraji, M., A. Hassanzadeh, and M. Mohseni, *Interlaced WO3-carbon nanotube nanocomposite electrodeposited on graphite as a positive electrode in vanadium redox flow battery.* Thin Solid Films, 2017. **642**: p. 188-194.

117. Ma, Q., et al., *High electro-catalytic graphite felt/MnO_2 composite electrodes for vanadium redox flow batteries.* Science China Chemistry, 2018. **61**(6): p. 732-738.

118. He, Z., et al., *Mn_3O_4 anchored on carbon nanotubes as an electrode reaction catalyst of V(IV)/V(V) couple for vanadium redox flow batteries.* Electrochimica Acta, 2015. **176**: p. 1434-1440.

119. Ejigu, A., M. Edwards, and D.A. Walsh, *Synergistic Catalyst–Support Interactions in a Graphene–Mn_3O_4 Electrocatalyst for Vanadium Redox Flow Batteries.* ACS Catalysis, 2015. **5**(12): p. 7122-7130.

120. Zeng, L., T. Zhao, and L. Wei, *Revealing the performance enhancement of oxygenated carbonaceous materials for vanadium redox flow batteries: functional groups or specific surface area?* Advanced sustainable systems, 2018. **2**(2): p. 1700148.
121. Sun, B. and M. Skyllas-Kazacos, *Chemical modification of graphite electrode materials for vanadium redox flow battery application—part II. Acid treatments.* Electrochimica Acta, 1992. **37**(13): p. 2459-2465.
122. Ju, H.X., et al., *The electrochemical behavior of methylene blue at a microcylinder carbon fiber electrode.* Electroanalysis, 1995. **7**(12): p. 1165-1170.
123. Yi, Y., et al., *Electrochemical corrosion of a glassy carbon electrode.* Catalysis Today, 2017. **295**: p. 32-40.
124. Bourke, A., et al., *Effect of Cathodic and Anodic Treatments of Carbon on the Electrode Kinetics of VIV/VVOxidation-Reduction.* Journal of The Electrochemical Society, 2015. **162**(8): p. A1547-A1555.
125. Bourke, A., et al., *Electrode Kinetics of Vanadium Flow Batteries: Contrasting Responses of VII-VIIIand VIV-VVto Electrochemical Pretreatment of Carbon.* Journal of The Electrochemical Society, 2015. **163**(1): p. A5097-A5105.
126. Li, X.-g., et al., *Electrochemical behavior of diverse vanadium ions at modified graphite felt electrode in sulphuric solution.* Journal of Central South University of Technology, 2007. **14**(1): p. 51-56.
127. Kil, D., et al., *Synthesis of activated graphite felts using short-term ozone/heat treatment for vanadium redox flow batteries.* Journal of The Electrochemical Society, 2017. **164**(13): p. A3011.
128. Wang, W., et al., *Kinetic investigation of vanadium (V)/(IV) redox couple on electrochemically oxidized graphite electrodes.* Electrochimica Acta, 2016. **205**: p. 102-112.
129. He, Z., et al., *Carbon layer-exfoliated, wettability-enhanced, SO3H-functionalized carbon paper: A superior positive electrode for vanadium redox flow battery.* Carbon, 2018. **127**: p. 297-304.
130. Di Blasi, A., et al., *Investigation of several graphite-based electrodes for vanadium redox flow cell.* Journal of Power Sources, 2013. **227**: p. 15-23.

131. González, Z., et al., *Thermally reduced graphite and graphene oxides in VRFBs.* Nano Energy, 2013. **2**(6): p. 1322-1328.
132. Schmidt, C.N. and G. Cao, *Properties of mesoporous carbon modified carbon felt for anode of all-vanadium redox flow battery.* Science China Materials, 2016. **59**(12): p. 1037-1050.
133. Yang, H., C. Fan, and Q. Zhu, *Activated charcoal modified graphite felts using for positive electrodes of vanadium redox flow battery.* Journal of Electrochemical Energy Conversion and Storage, 2017. **14**(4).
134. Lee, M.E., et al., *Standalone macroporous graphitic nanowebs for vanadium redox flow batteries.* Journal of industrial and engineering chemistry, 2018. **60**: p. 85-90.
135. Peng, L., et al., *Holey 2D nanomaterials for electrochemical energy storage.* Advanced Energy Materials, 2018. **8**(9): p. 1702179.
136. Liu, Y., et al., *Holey-engineered electrodes for advanced vanadium flow batteries.* Nano Energy, 2018. **43**: p. 55-62.
137. Zhou, Y., et al., *Carbon dots promoted vanadium flow batteries for all-climate energy storage.* Chemical Communications, 2017. **53**(54): p. 7565-7568.
138. Han, P., et al., *Graphene oxide nanoplatelets as excellent electrochemical active materials for VO^{2+}/VO_2^+ and V^{2+}/V^{3+} redox couples for a vanadium redox flow battery.* Carbon, 2011. **49**(2): p. 693-700.
139. Schuette, S.A. and R.L. McCreery, *Efficient Hydrodynamic Modulation Voltammetry with a Microcylinder Electrode.* Analytical Chemistry, 1986. **58**(8): p. 1778-1782.
140. Kovach, P.M., M.R. Deakin, and R.M. Wightman, *Electrochemistry at partially blocked carbon-fiber microcylinder electrodes.* Journal of Physical Chemistry, 1986. **90**(19): p. 4612-4617.
141. Wang, J., P. Tuzhi, and V. Villa, *Activation of carbon fiber microelectrodes by alternating current electrochemical treatment.* Journal of Electroanalytical Chemistry, 1987. **234**(1-2): p. 119-131.
142. Aoki, K. and H. Kaneko, *Theory of irreversible cyclic voltammograms at microcylinder electrodes.* Journal of Electroanalytical Chemistry, 1988. **247**(1-2): p. 17-27.

143. Oldham, K.B., *Steady-state microelectrode voltammetry as a route to homogeneous kinetics.* Journal of Electroanalytical Chemistry, 1991. **313**(1-2): p. 3-16.
144. Neudeck, A. and J. Dittrich, *The determination of diffusion coefficients and rate constants from the dependence of the peak separation and peak current on the scan rate of cyclic voltammograms at micro-cylindrical electrodes.* Journal of Electroanalytical Chemistry, 1991. **313**(1-2): p. 37-59.
145. Wu, H.P. and R.L. McCreery, *Observation of Concentration Profiles at Cylindrical Microelectrodes by a Combination of Spatially Resolved Absorption Spectroscopy and the Abel Inversion.* Analytical Chemistry, 1989. **61**(21): p. 2347-2352.
146. Fleischmann, M., S. Pons, and J. Daschbach, *The ac impedance of spherical, cylindrical, disk, and ring microelectrodes.* Journal of Electroanalytical Chemistry, 1991. **317**(1-2): p. 1-26.
147. Kasper, C., *The Theory of the Potential and the Technical Practice of Electrodeposition.* Transactions of The Electrochemical Society, 1940. **77**(1).
148. Jacobsen, T. and K. West, *Diffusion impedance in planar, cylindrical and spherical symmetry.* Electrochimica Acta, 1995. **40**(2): p. 255-262.
149. Barral, G., J.P. Diard, and C. Montella, *Etude d'un modele de reaction electrochimique d'insertion-I. Resolution pour une commande dynamique a petit signal.* Electrochimica Acta, 1984. **29**(2): p. 239-246.
150. Lasia, A., *Electrochemical impedance spectroscopy and its applications*. Electrochemical Impedance Spectroscopy and its Applications. Vol. 9781461489337. 2014. 1-367.
151. de Levie, R. and L. Pospíšil, *On the coupling of interfacial and diffusional impedances, and on the equivalent circuit of an electrochemical cell.* Journal of Electroanalytical Chemistry, 1969. **22**(3): p. 277-290.
152. Angell, D.H. and T. Dickinson, *The kinetics of the ferrous/ferric and ferro/ferricyanide reactions at platinum and gold electrodes. Part I. Kinetics at bare-metal surfaces.* Journal of Electroanalytical Chemistry, 1972. **35**(1): p. 55-72.
153. Bates, D.M. and D.G. Watts, *Nonlinear Regression Analysis and Its Applications*. 1988.

154. McCreery, R.L., *Advanced Carbon Electrode Materials for Molecular Electrochemistry.* Chemical Reviews, 2008. **108**(7): p. 2646-2687.
155. Chen, P. and R.L. McCreery, *Control of Electron Transfer Kinetics at Glassy Carbon Electrodes by Specific Surface Modification.* Analytical Chemistry, 1996. **68**(22): p. 3958-3965.
156. Blaedel, W.J. and R.C. Engstrom, *Investigations of the Ferricyanide-Ferrocyanide System by Pulsed Rotation Voltammetry.* Analytical Chemistry, 1978. **50**(3): p. 476-479.
157. Galus, Z. and R.N. Adams, *The investigation of the kinetics of moderately rapid electrode reactions using rotating disk electrodes.* Journal of Physical Chemistry, 1963. **67**(4): p. 866-871.
158. Miller, M.A., et al., *Kinetic study of electrochemical treatment of carbon fiber microelectrodes leading to in situ enhancement of vanadium flow battery efficiency.* Journal of the Electrochemical Society, 2016. **163**(9): p. A2095-A2102.
159. Rabbow, T.J., et al., *Variability within a single type of polyacrylonitrile-based graphite felt after thermal treatment. Part II: chemical properties.* Electrochimica Acta, 2015. **173**: p. 24-30.
160. Perry, M.L. and A.Z. Weber, *Advanced Redox-Flow Batteries: A Perspective.* Journal of The Electrochemical Society, 2016. **163**(1): p. A5064-A5067.
161. Tichter, T., et al., *Theory of cyclic voltammetry in random arrays of cylindrical microelectrodes applied to carbon felt electrodes for vanadium redox flow batteries.* Physical chemistry chemical physics : PCCP, 2019. **21**(18): p. 961-968.
162. Sohr, R., L. Müller, and R. Landsberg, *Elektrochemische Untersuchungen am Redoxsystem Hexacyanoferrat(II)/Hexacyanoferrat(III)an Graphitelektroden.* Journal of Electroanalytical Chemistry, 1974. **50**(1): p. 55-63.
163. Fletcher, S. and T.S. Varley, *Beyond the Butler-Volmer equation. Curved Tafel slopes from steady-state current-voltage curves.* Physical Chemistry Chemical Physics, 2011. **13**(12): p. 5359-5364.

164. Kim, K.J., et al., *A new strategy for integrating abundant oxygen functional groups into carbon felt electrode for vanadium redox flow batteries.* Scientific Reports, 2014. **4**(1): p. 6906.

165. Mehboob, S., et al., *Enhancing the performance of all-vanadium redox flow batteries by decorating carbon felt electrodes with SnO_2 nanoparticles.* Applied Energy, 2018. **229**: p. 910-921.

166. Davies, T. and J. Tummino, *High-Performance Vanadium Redox Flow Batteries with Graphite Felt Electrodes.* C - Journal of Carbon Research, 2018. **4**(1): p. 8.

167. Li, Y., et al., *Impact of Surface Carbonyl- and Hydroxyl-Group Concentrations on Electrode Kinetics in an All-Vanadium Redox Flow Battery.* The Journal of Physical Chemistry C, 2019. **123**(11): p. 6370-6378.

168. Nicholson, R.S., *Theory and Application of Cyclic Voltammetry for Measurement of Electrode Reaction Kinetics.* Analytical Chemistry, 1965. **37**(11): p. 1351-1355.

169. Yue, L., et al., *Highly hydroxylated carbon fibres as electrode materials of all-vanadium redox flow battery.* Carbon, 2010. **48**(11): p. 3079-3090.

170. González, Z., et al., *Thermally reduced graphite oxide as positive electrode in Vanadium Redox Flow Batteries.* Carbon, 2012. **50**(3): p. 828-834.

171. Li, W., J. Liu, and C. Yan, *Reduced graphene oxide with tunable C/O ratio and its activity towards vanadium redox pairs for an all vanadium redox flow battery.* Carbon, 2013. **55**: p. 313-320.

172. Menshykau, D. and R.G. Compton, *The influence of electrode porosity on diffusional cyclic voltammetry.* Electroanalysis, 2008. **20**(22): p. 2387-2394.

173. Menshykau, D., I. Streeter, and R.G. Compton, *Influence of Electrode Roughness on Cyclic Voltammetry.* The Journal of Physical Chemistry C, 2008. **112**(37): p. 14428-14438.

174. Streeter, I., et al., *Cyclic voltammetry on electrode surfaces covered with porous layers: An analysis of electron transfer kinetics at single-walled carbon nanotube modified electrodes.* Sensors and Actuators B: Chemical, 2008. **133**(2): p. 462-466.

175. Barnes, E.O., et al., *Voltammetry at porous electrodes: A theoretical study.* Journal of Electroanalytical Chemistry, 2014. **720-721**: p. 92-100.

176. Ward, K.R., et al., *Nanoparticle modified electrodes can show an apparent increase in electrode kinetics due solely to altered surface geometry: The effective electrochemical rate constant for non-flat and non-uniform electrode surfaces.* Journal of Electroanalytical Chemistry, 2013. **695**: p. 1-9.

177. Friedl, J. and U. Stimming, *Determining Electron Transfer Kinetics at Porous Electrodes.* Electrochimica Acta, 2017. **227**: p. 235-245.

178. Tichter, T., et al., *Theory of cyclic voltammetry in random arrays of cylindrical microelectrodes applied to carbon felt electrodes for vanadium redox flow batteries.* Physical Chemistry Chemical Physics, 2019. **21**(18): p. 9061-9068.

179. Miller, M.A., et al., *Kinetic Study of Electrochemical Treatment of Carbon Fiber Microelectrodes Leading to In Situ Enhancement of Vanadium Flow Battery Efficiency.* Journal of The Electrochemical Society, 2016. **163**(9): p. A2095-A2102.

180. Narita, A., et al., *Characterization of Carbon Fiber Electrode for Vanadium-Based Redox Flow Batteries.* ECS Transactions, 2015. **68**(3): p. 89-95.

181. Neudeck, A. and J. Dittrich, *The determination of diffusion coefficients and rate constants from the dependence of the peak separation and peak current on the scan rate of cyclic voltammograms at micro-cylindrical electrodes.* Journal of Electroanalytical Chemistry, 1991. **313**(1): p. 37-59.

182. Batchelor-McAuley, C., et al., *Recent Advances in Voltammetry.* ChemistryOpen, 2015. **4**(3): p. 224-260.

183. Golub, D. and Y. Oren, *Graphite felt as an electrode for thin-layer electrochemistry.* Journal of Applied Electrochemistry, 1990. **20**(5): p. 877-879.

184. Kato, K., K. Kano, and T. Ikeda, *Electrochemical Characterization of Carbon Felt Electrodes for Bulk Electrolysis and for Biocatalyst-Assisted Electrolysis.* Journal of The Electrochemical Society, 2000. **147**(4): p. 1449-1453.

185. Aoki, K., H. Kaneko, and K. Nozaki, *Estimation of charge transfer kinetic parameters from irreversible cyclic voltammograms at carbon fiber electrodes.* Journal of Electroanalytical Chemistry, 1988. **247**(1-2): p. 29-36.

186. Amatore, C.A., M.R. Deakin, and M. Wightman, *Electrochemical kinetics at microelectrodes Part 1. Quasi-reversible electron transfer at cylinders.* Journal of Electroanalytical Chemistry, 1986. **206**(1-2): p. 23-36.

187. Bieniasz, L.K., *Automatic simulation of electrochemical transients at cylindrical wire electrodes, by the adaptive Huber method for Volterra integral equations.* Journal of Electroanalytical Chemistry, 2011. **662**(2): p. 371-378.

188. Landon-Lane, L., A.T. Marshall, and D.A. Harrington, *EIS at carbon fiber cylindrical microelectrodes.* Electrochemistry Communications, 2019. **109**: p. 106566.

189. Banerjee, R., et al., *Characterization of carbon felt electrodes for vanadium redox flow batteries – A pore network modeling approach.* Journal of Energy Storage, 2019. **21**: p. 163-171.

190. Montella, C., *LSV/CV modelling of electrochemical reactions with interfacial CPE behaviour, using the generalised Mittag–Leffler function.* Journal of Electroanalytical Chemistry, 2012. **667**: p. 38-47.

191. Yang, Z., et al., *Electrochemical Energy Storage for Green Grid.* Chemical Reviews, 2011. **111**(5): p. 3577-3613.

192. Chakrabarti, M.H., et al., *Application of carbon materials in redox flow batteries.* Journal of Power Sources, 2014. **253**: p. 150-166.

193. Park, M., J. Ryu, and J. Cho, *Nanostructured Electrocatalysts for All-Vanadium Redox Flow Batteries.* Chemistry – An Asian Journal, 2015. **10**(10): p. 2096-2110.

194. Xi, J., et al., *Effect of electro-oxidation current density on performance of graphite felt electrode for vanadium redox flow battery.* International Journal of Electrochemical Science, 2013. **8**(4): p. 4700-4711.

195. Bismarck, A., M.E. Kumru, and J. Springer, *Influence of Oxygen Plasma Treatment of PAN-Based Carbon Fibers on Their Electrokinetic and Wetting Properties.* Journal of Colloid And Interface Science, 1999. **210**(1): p. 60-72.

196. Estevez, L., et al., *Tunable Oxygen Functional Groups as Electrocatalysts on Graphite Felt Surfaces for All-Vanadium Flow Batteries.* ChemSusChem, 2016. **9**(12): p. 1455-1461.

197. Sun, B. and M. Skyllas-Kazacos, *Modification of graphite electrode materials for vanadium redox flow battery application-I. Thermal treatment.* Electrochimica Acta, 1992. **37**(7): p. 1253-1260.

198. Pupkevich, V., V. Glibin, and D. Karamanev, *The effect of activation on the electrochemical behaviour of graphite felt towards the Fe3+/Fe2+ redox electrode reaction.* Electrochemistry Communications, 2007. **9**(8): p. 1924-1930.

199. Frysz, C.A. and D.D.L. Chung, *Improving the electrochemical behavior of carbon black and carbon filaments by oxidation.* Carbon, 1997. **35**(8): p. 1111-1127.

200. 李晓刚 黄可龙 刘素琴 谭宁, 陈., *Characteristics of graphite felt electrode electrochemically oxidized for vanadium redox battery application.* 中国有色金属学会会刊：英文版, 2007. **17**(1): p. 195-199.

201. Sun, B. and M. Skyllas-Kazacos, *Chemical modification of graphite electrode materials for vanadium redox flow battery application-part II. Acid treatments.* Electrochimica Acta, 1992. **37**(13): p. 2459-2465.

202. Wu, T., et al., *Hydrothermal ammoniated treatment of PAN-graphite felt for vanadium redox flow battery.* Journal of Solid State Electrochemistry, 2012. **16**(2): p. 579-585.

203. Flox, C., et al., *Thermo–chemical treatments based on NH3/O2 for improved graphite-based fiber electrodes in vanadium redox flow batteries.* Carbon, 2013. **60**: p. 280-288.

204. Rice, R.J. and R.L. McCreery, *Quantitative relationship between electron transfer rate and surface microstructure of laser-modified graphite electrodes.* Analytical Chemistry, 1989. **61**(15): p. 1637-1641.

205. Rice, R.J., N.M. Pontikos, and R.L. McCreery, *Quantitative correlations of heterogeneous electron-transfer kinetics with surface properties of glassy carbon electrodes.* Journal of the American Chemical Society, 1990. **112**(12): p. 4617-4622.

206. Rabbow, T.J., et al., *Variability within a single type of polyacrylonitrile-based graphite felt after thermal treatment. Part I: physical properties.* Electrochimica Acta, 2015. **173**: p. 17-23.

207. Rabbow, T.J. and A.H. Whitehead, *Deconvolution of electrochemical double layer capacitance between fractions of active and total surface area of graphite felts.* Carbon, 2017. **111**: p. 782-788.
208. Pezeshki, A.M., et al., *High performance electrodes in vanadium redox flow batteries through oxygen-enriched thermal activation.* Journal of Power Sources, 2015. **294**(C): p. 333-338.
209. Friedl, J., et al., *Electron transfer kinetics of the VO2+/VO2+ – Reaction on multi-walled carbon nanotubes.* Carbon, 2013. **63**: p. 228-239.
210. Lee, Y.-H., K.-H. Chang, and C.-C. Hu, *Differentiate the pseudocapacitance and double-layer capacitance contributions for nitrogen-doped reduced graphene oxide in acidic and alkaline electrolytes.* Journal of Power Sources, 2013. **227**: p. 300-308.
211. Bevilacqua, N., et al., *Visualization of electrolyte flow in vanadium redox flow batteries using synchrotron X-ray radiography and tomography – Impact of electrolyte species and electrode compression.* Journal of Power Sources, 2019. **439**: p. 227071.
212. Schuepfer, D.B., et al., *Assessing the structural properties of graphitic and non-graphitic carbons by Raman spectroscopy.* Carbon, 2020. **161**: p. 359-372.
213. Pimenta, M.A., et al., *Studying disorder in graphite-based systems by Raman spectroscopy.* Physical Chemistry Chemical Physics, 2007. **9**(11): p. 1276-1290.
214. Malard, L.M., et al., *Raman spectroscopy in graphene.* Physics Reports, 2009. **473**(5): p. 51-87.
215. Dresselhaus, M.S., A. Jorio, and R.Saito, *Characterizing Graphene, Graphite, and Carbon Nanotubes by Raman Spectroscopy.* Annual Review of Condensed Matter Physics, 2010. **1**(1): p. 89-108.
216. Meunier, V., et al., *Physical properties of low-dimensional ${sp}^{2}$-based carbon nanostructures.* Reviews of Modern Physics, 2016. **88**(2): p. 025005.
217. Mochalin, V., S. Osswald, and Y. Gogotsi, *Contribution of Functional Groups to the Raman Spectrum of Nanodiamond Powders.* Chemistry of Materials, 2009. **21**(2): p. 273-279.

218. Wang, Y.-H., I.M. Hung, and C.-Y. Wu, *The characteristics and electrochemical performance of graphite felts with thermal and fenton's reagent treatment for vanadium redox flow battery.* Ceramics International, 2018. **44**: p. S30-S33.

219. Ding, H.B., et al., *Investigations on the Thermal and Acid Treatment of Graphite Felt for Vanadium Redox Flow Battery Application.* Advanced Materials Research, 2014. **953-954**: p. 1157-1162.

220. Ghimire, P.C., et al., *Optimization of thermal oxidation of electrodes for the performance enhancement in all-vanadium redox flow betteries.* Carbon, 2019. **155**: p. 176-185.

221. Liu, T., et al., *Activated Carbon Fiber Paper Based Electrodes with High Electrocatalytic Activity for Vanadium Flow Batteries with Improved Power Density.* ACS Applied Materials & Interfaces, 2017. **9**(5): p. 4626-4633.

222. Chen, D., et al., *Optimizing membrane thickness for vanadium redox flow batteries.* Journal of Membrane Science, 2013. **437**: p. 108-113.

223. Liu, Q.H., et al., *High Performance Vanadium Redox Flow Batteries with Optimized Electrode Configuration and Membrane Selection.* Journal of The Electrochemical Society, 2012. **159**(8): p. A1246-A1252.

224. Aaron, D., et al., *Polarization curve analysis of all-vanadium redox flow batteries.* Journal of Applied Electrochemistry, 2011. **41**(10): p. 1175-1182.

225. Vardner, J.T., et al., *Current-Driven Vanadium Crossover as a Function of SOC and SOD in the Vanadium Redox Flow Battery.* Journal of The Electrochemical Society, 2020. **167**(8): p. 080512.

226. Agar, E., et al., *Identification of performance limiting electrode using asymmetric cell configuration in vanadium redox flow batteries.* Journal of Power Sources, 2013. **225**: p. 89-94.

227. Davies, T. and J. Tummino, *High-Performance Vanadium Redox Flow Batteries with Graphite Felt Electrodes.* C, 2018. **4**(1): p. 8.

228. Chen, D., et al., *Selective anion exchange membranes for high coulombic efficiency vanadium redox flow batteries.* Electrochemistry Communications, 2013. **26**: p. 37-40.

229. Schweiss, R., C. Meiser, and D. Dan, *Effect of Operating Temperature on Individual Half-Cell Reactions in All-Vanadium Redox Flow Batteries.* Batteries, 2018. **4**(4): p. 55.

230. Fetyan, A., et al., *Detrimental role of hydrogen evolution and its temperature-dependent impact on the performance of vanadium redox flow batteries.* Journal of Energy Chemistry, 2019. **32**: p. 57-62.